Estimation of slack tide using GPS measurements on a buoy

A case study on buoy 18 in the Schelde Estuary

M. Valk BSc.

14 March 2012

TUDelft

Estimation of slack tide using GPS measurements on a buoy
A case study on buoy 18 in the Schelde Estuary

MASTER OF SCIENCE THESIS

For obtaining the degree of Master of Science in Geomatics Engineering at Delft University of Technology

M. Valk BSc.

14 March 2012

Faculty of Civil Engineering and Geosciences · Delft University of Technology

Delft University of Technology

The undersigned hereby certify that they have read and recommend to the Faculty of Civil Engineering and Geosciences for acceptance a thesis entitled **"Estimation of slack tide using GPS measurements on a buoy"** by **M. Valk BSc.** in partial fulfillment of the requirements for the degree of **Master of Science**.

Dated: <u>14 March 2012</u>

Graduation professor:

_____

prof.dr.ir. R.F. Hanssen

Supervisor:

_____

dr.ir. C.C.J.M. Tiberius

Reader:

_____

Ir. W.M.J. Luxemburg

Summary

In this thesis a method is developed to estimate the moment of slack tide based on GPS measurements on a buoy. The moment of slack tide is the very moment the tidal current changes direction. The method is applied in the Schelde Estuary in the Netherlands.

An estuary is the transition between two distinct water bodies: a river and a sea. Estuaries are very important as a transport link and a source of food. Interventions in the estuary bathymetry, like dredging, can have severe impact on the hydraulic behavior of the estuary. Knowledge of the physical phenomena that determine the tidal flow is important as they influence the environment of an estuary in many ways. One of the key parameters in tidal propagation is the phase lag, which is the difference in time between high or low water and the subsequent moment of slack.

The main objective of this thesis is to estimate the moment of slack tide based on GPS measurements on a buoy ultimately with an accuracy in the order of 5-10 minutes. The buoy, which is used as an aid to navigation, is floating on the water and tied to the sea floor by a heavy anchor chain. In order to achieve this goal it is necessary to: investigate the performance of different GPS receivers in combination with different antennas and operating modes; analyze the motion of the buoy during several tidal cycles; develop a method to estimate the moment of slack tide based on GPS measurements on a buoy; and, investigate whether the results could be further improved by employing a Kalman filter that combines knowledge about the dynamics of the buoy and series of measurements over time as opposed to a single epoch slack tide estimation.

A static measurement campaign is performed to analyze the performance of low-end to mid-range GPS receivers using different antennas and different operating modes. The receivers are shown to perform according to manufacturer specifications. Furthermore, the difference in precision of the position estimators due to use of a better survey antenna as opposed to a simple patch antenna is shown.

During the dynamic measurement campaign in the Schelde Estuary the motion of the buoy is captured using a dual-frequency geodetic receiver in a relative positioning mode, resulting in centimeter accuracy. The acquired dataset consisted of three-dimensional position estimates of the buoy for a period of five days at a one second interval. Based

on this dataset the conclusion is made that the dynamics of the buoy, caused by the tidal current, can be captured almost entirely by one component (direction).

The axis of this component is aligned with the main current direction. The direction of this component is determined with principal component analysis (PCA). Furthermore a formula is developed that defines the centre point, right above the anchor point, which is the point of zero extension of the anchor chain.

The dynamics of the buoy can be approximated by a mathematical model. The chosen model is a mass-spring-damper system and it is calibrated using the observed motion of the buoy. This model is rewritten in a state-space format and implemented in a Kalman filter algorithm. To show the improvement due to Kalman filtering, the observed extension is intentionally degraded with Gaussian noise to represent the situation of a low-end GPS receiver. The filtered extensions estimates show in terms of precision a significant improvement of almost 60-70 %.

The position of the buoy related to moment of slack tide can be described by a simple formula which depends on: the length of the anchor chain, the charted water depth and water elevation which are related to the same datum, and the draft of the buoy. The estimation of slack tide is based on hypothesis testing. The test is designed to determine whether the extension of the buoy is either larger or smaller than the extension related to the moment of slack tide. Later on, the estimated moments of slack tide are related to high and low water to determine the phase lag.

The results are validated against one-dimensional tidal propagation models and nearby current observations. However, the estimated phase lags are not in agreement with the tidal propagation models. The main reason for this disagreement is that the one-dimensional tidal propagation models compute an estuary cross-sectional average phase lag. However, the observed phase lags only hold for the location of the buoy. Besides, the results are in good agreement with nearby current measurements.

The main conclusion is that the estimation of slack tide based on GPS measurements on a buoy can be accomplished with an accuracy better than 10 minutes. This could be further improved by application of the designed Kalman filter. In the recommendations the design of an operational system is given.

Acknowledgements

First of all, I would like to express my special thanks to my supervisor Dr. Ir. C.C.J.M. Tiberius. Christiaan his eye for detail, his integrity and his enthusiasm inspired me during this research. I greatly appreciate your time devoted to help me this research.

I would like to express my gratitude to the committee members, Prof. Dr. Ir. R.F. Hanssen, Prof. Dr. Ir. H.H.G. Savenije and Ir. W.M.J. Luxemburg for agreeing to be in the committee, the progress meetings, for reading the draft thesis and giving their constructive comments. I should acknowledge Dr. Ir. H. van der Marel and Ir. P.J. Buist for their support during this research.

My thanks go to Multraship, and in particular Jan-Willem Regt for the tendering to the buoy, the possibility to install our base station at the roof of the Multraship office and the commitment of this company to this research. The support of the Department of Waterways and Public Works, in particular Ing. L. Dekker, J. van Espen and Ing. I. Schep, is much appreciated.

I would like to thank my student colleagues Wouter Berghuijs and Bart van Osnabrugge for the pleasant cooperation and their support during the measurement campaign in Schelde Estuary.

Tom and Mark, we started our master study at TU Delft in 2009. My time here in Delft would not have been so much fun without you. My roommate Tim, special thanks for reading the draft versions, providing constructive corrections and for the pleasant time at our apartment. Niek, your help on state equations and the nice coffee breaks we shared is well appreciated.

Finally, I am absolutely indebted to my parents and sister for their love, encouragement and their patience during my study period in Terschelling and Delft.

Delft, The Netherlands   M. Valk BSc.
14 March 2012

Contents

List of Figures

List of Tables

Nomenclature

Latin Symbols

A	Effective surface	$[m^2]$
A	Model Matrix	[-]
a	Calibration constant spring force model	[-]
B_L	Bandwidth of the code tracking loop	[Hz]
B	Stream width of the estuary	[m]
b	Convergence length of the stream width	[m]
b	Receiver clock drift	$[s^{-1}]$
C	Centre point of the buoy's extension	[m]
c	Damping coefficient of the mass spring system	[N s/m]
c	Speed of light in GPS observation equation	[m/s]
c	Wave celerity in the phase lag equation	[m/s]
c_d	Drag coefficient	[-]
d	Early to late correlator spacing, normalized with respect to one chip	[-]
Dr	Draft	[m]
e	User-to-satellite line of sight vector	[m]
E	Extension of the buoy	[m]
E	Local east component	[m]
F	Force	[N]
F	State matrix	[-]
G	Geometry matrix satellite-user	[-]
G	Gain of the GPS-antenna	[dBic]

G	Input matrix	[-]
g	Local gravity acceleration	$[m/s^2]$
H	Hypothesis	[-]
h	Height with regard to the ellipsoid	[m]
h_w	Wave height	[m]
I	Ionospheric delay	[m]
K	Critical Region	[-]
k	Critical value	[-]
k	Spring constant in the mass spring system	[N/m]
L	Length	[m]
M	Moment (time tag)	[hh:mm:ss]
m	Mass	[kg]
m	Number of estimates	[-]
N	Local north component	[m]
N	Number of measurements for the determination of the empirical standard deviation	[-]
n	Number of bins	[-]
n	Number of unknowns	[-]
p	Order of the spring constant	[-]
p	Pseudo-code range	[m]
Q	Error covariance matrix	[-]
r	Topocentric distance	[m]
T	Matrix of eigenvectors of the mass spring system	[-]
T	Tidal amplitude	[m]
T	Tropospheric delay	[m]
t	Time	[s]
U	Local up component	[m]
v	Velocity vector based on Doppler observations	$[m/s^2]$
v	Flow velocity	[m/s]
w	Bin size	[m]
x	Position vector	[m]
X	Matrix consisting of the local east E and north N vector	[m]
x	Extension in the mathematical model and Kalman filter	[m]
x	Inward distance in the estuary with regard to a predefined point	[m]
Z	Orthometric depth with respect to NAP	[m]
z	Specific force / Acceleration	$[m/s^2]$

Greek Symbols

α	Significance level	[-]
γ	Damping frequency	[s^{-1}]
γ	Detection power	[-]
Δ	Difference operator	[-]
δ	Damping rate in the phase lag equation	[m^{-1}]
δ	Error	[s]
ϵ	Phase lag	[mm:ss]
ϵ	Receiver noise, multipath and other errors	[m]
λ	Eigenvalues of the mass-spring system	[m]
λ	Length of the tidal wave	[m]
λ	Longitude	[°]
μ	Bias	[m]
ρ	Mass density of the fluid	[kg/m^3]
σ	Standard deviation about the (empirical) mean	[-]
τ	Interval	[s]
τ	Travel time	[s]
Φ	Transition Matrix	[-]
ϕ	Latitude	[°]
ω	Angular velocity	[s^{-1}]
ω	Undamped angular frequency of the mass spring system	[s^{-1}]

Subscripts

$_0$	Null	
$_a$	Alternative	
$_{bd}$	Buoy Dynamics	
$_{bs}$	Base Station	
$_{buoy}$	Buoy	
$_{chain}$	Chain	
$_{CS}$	Satellite clock and ephemeris parameters	
$_{Flow}$	Tidal current	
$_{gps}$	Global Positioning System	
$_{hws}$	High Water Slack	
$_{hw}$	High Water	
$_k$	Epoch	
$_{lws}$	Low Water Slack	

lw	Low Water
P	Atmospheric propagation modeling
RNM	Receiver Noise and Multipath
rr	Rover Receiver
r	Receiver
st	Slack Tide
URE	User Range Error

Superscripts

^{hw}	High Water
^{lw}	Low Water
^{s}	Satellite

Abbreviations

ADCP	Acoustic Doppler Current Profiler
APPS	Automatic Precise Point Positioning Service
ATON	Aid to Navigation
DGPS	Differential Global Positioning System
DOP	Dilution Of Precision
DPGA	Dutch Permanent GNSS Array
EGNOS	European Geostationary Navigation Overlay System
FFT	Fast Fourier Transform
GIVD	Grid Ionosphere Vertical Delay
GLONASS	GLObal'naya NAvigatsionnaya Sputnikovaya Sistema
GPS	Global positioning system
HL	Low Water
HWS	High Water Slack
HW	High Water
ITRF	International Terrestrial Reference Frame
JPL	Jet Propulsion Laboratory
LWS	Low Water Slack
MOPS	Minimum Operational Performance Standard
NAP	Amsterdam Ordnance Datum
NMEA	National Marine Electronics Association
PCA	Principle Component Analysis

PPP	Precise Point Positioning
RINEX	Receiver Independent Exchange Format
RWS	Ministry of Transport, Public Works and Water Management
SA	Selective Availability
SBAS	Satellite-Based Augmentation System
SIS URE	Signal in Space User Range Error
SOBEK	SOBEK is not an abbreviation, but is the name of a powerful 1D tidal propagation software package
SPS	Standard Positioning Service
TGO	Trimble Geomatics Office
URE	User Range Error
WGS84	World Geodetic System 1984
WLSE	Weighted Least Squares Estimation

Chapter 1

Introduction

In this thesis a method is developed for the estimation of the moment of slack tide in estuaries based on GPS measurements on a buoy. Slack tide is the very moment the water current changes its direction during a tidal cycle. The method is applied in the Schelde Estuary, near the city of Terneuzen, in The Netherlands.

An estuary is the transition between two distinct water bodies: a river and a sea. Estuaries have always been important to mankind, both as a transport link between the river and the sea, and as a source of food. Interventions in the estuary topography, like dredging, can have severe impacts on the hydraulic behavior of an estuary, disturbing the delicate equilibrium, which may cause dramatic and often irreversible changes. Knowledge of the physical phenomena that determine the tidal flow is important as it influences the environment of an estuary in many ways. The following case study illustrates the previous statements.

In the late 1950's, dredging activities greatly altered the physical processes in the Eems Estuary. Deepening and streamlining the shipping channels resulted in an increased tidal range in the river by as much as 1.5m. Also the turbidity maximum between are currently 1-2 order of magnitude larger than in the 1950's [Talke & Swart, 2006].

Savenije (2005) derived multiple analytical equations that describe the tidal behavior in estuaries. In these equations the phase lag between high water and high water slack plays a crucial role. The phase lag is therefore a key parameter in hydraulic studies. The phase lag is the timespan between the moment of high or low water and the subsequent moment of slack, when the current changes direction.

On the other hand, recent developments in the Physical Oceanographic Real-time System Project (PORTS)[1] show the benefits of real time current observations in harbors. Real

---

[1] *PORTS is a decision support tool that improves the safety and efficiency of maritime commerce and coastal resource management through the integration of real-time environmental observations, forecasts and other geospatial information. PORTS measures and disseminates observations and predictions of water levels, currents, salinity, and meteorological parameters (e.g., winds, atmospheric pressure, air and water temperatures) that mariners need to navigate safely [NOAA, 2011].*

time water current data improves navigation safety, spur the economy and benefit the environment [Hamilton & Wright, 2009].

Unfortunately, the measurement of water currents, and therefore the measurement of the phase lag, is four till ten times more expensive to do as the measurement of water levels. This has important implications on the quality and number of current observations [NOAA, 2011]. Furthermore, water currents, in opposite to water levels, are highly spatially variable. Lievens (2010) proposed a simple and cheap method to estimate the moment in time of slack tide based on GPS measurements on ATON (Aids To Navigation) buoys. However, this concept is still in an early phase.

This research continues with this concept, although it is focused on the development of a method for the estimation of slack tide based on GPS measurements on buoys and the choice of an appropriate GPS measurement set-up. The combination of GPS and the measurement of tidal behavior is the field of marine geodesy, a multidisciplinary field.

1.1   Research goal

The aim of this MSc-graduation research is to detect and estimate the moment of slack tide with GPS measurements on an ATON buoy, and do this as accurately as possible, preferably with an accuracy of better than 10 minutes, in real time and with modest means.

Therefore, the goal of this master thesis is:

The estimation of slack tide using GPS measurements on a buoy.

This main goal is subdivided in several subquestion/subgoals:

Which GPS receiver, antenna and operating method is most suited for this specific goal?

There is a wide variety of GPS measurement methods varying from low to high accuracy: standalone, augmented, differential GPS (DGPS) to carrier phase real time kinematic. Part of this research is a substantial and systematic measurement campaign to conclude which GPS measurement method is most suited in a performance - cost trade off.

What is the actual motion of the buoy during a tidal cycle?

To separate GPS measurement noise from 'noise' in the dynamics of the buoy, it is useful to observe the actual motion with a high performance GPS measurement set-up. This serves as a calibration, and helps to investigate the true dynamics of the buoy. This is also useful for the requirements definition of the measurement technique. I.e. what is the necessary precision and accuracy?

What is the most suitable navigation data from the GPS measurements?

A GPS receiver can produce a wide variety of data: absolute or relative position in 2D or 3D, displacement and velocity based on Doppler observations. I.e. what kind of navigation data provides the most accurate information about the moment of slack tide

through the motion of the buoy. This part is also closely linked to the method that is used for the estimation of slack tide.

What is a suitable method to estimate the moment of slack tide based on GPS measurement on the buoy?

Likely there are various possibilities to estimate the time of slack. The solution may lie in statistical significance testing on the position of the buoy. Therefore a relation between the position of the buoy and moment of slack needs to be established. Besides this functional description also the stochastic properties of the buoy's motion and the definition of the moment of slack tide are analyzed.

How do the results compare against nearby measurements of the water current and estuary tidal propagation models?

Although, current measurements are spare in the Schelde Estuary, the results are compared with nearby current magnitude and direction measurements. In this way, it is possible to validate the results. Furthermore, the results are compared against one dimensional approximations of the tidal dynamics in convergent estuaries.

Can the method be further improved by including the knowledge about the dynamics of the buoys and series of measurement as opposed to a single epoch slack tide estimation?

In a Kalman Filter, the dynamics of the buoy could be included. In this way the buoy is treated as a dynamic system, which enables Kalman filtering of the position estimates. Therefore a mathematical representation of the buoys dynamics needs to be found. This model can be rewritten in a state-space format and implemented in a Kalman filter algorithm. The Kalman filter exploits series of measurement, which are linked through a dynamic model. This subgoal shows the performance improvement by the Kalman filter.

1.2 Research area

An interesting introduction on the Schelde Estuary is described by [Eck, 1999]. Some relevant facts are presented here. The Zeeschelde and the Westerschelde together form the Schelde estuary. The Schelde Estuary is the area between Breskens / Vlissingen and Gent. The estuary is 50 meters wide near Gent and this increases to 5 kilometers at Vlissingen (see figure 1.1).

The Schelde Estuary is the only connection between the ports of Terneuzen, Gent and Antwerp and the North Sea. The port of Antwerp the is second largest port of Europe, ranked by the total freight shipping. The shipping lanes of the estuary are permanently dredged and monitored to ensure a safe entrance for vessels with a draft[2].

About 2,2 billion m^3 of water flows in and out of the estuary during a tidal period. The river discharges about 5.5 milion m^3 per tidal cycle, which is small compared to the tidal volume. This implies that the Schelde Estuary is tide dominated.

---

[2]*Draft refers to the distance between the vessel's waterline and the lowest point of the vessel, usually the keel.*

Figure 1.1: Overview of the Westerschelde Estuary, the small map in the left corner indicates the location of Westerschelde Estuary in West-Europe with a red rectangle. The complexity of this alluvial estuary is shown with this aerial photograph. The area shown measures 60 by 40 km. Image is taken from Google Maps.

1.3   Report outline

In chapter 2 the results of the literature study are described. The following subjects are addressed: Global Positioning System (GPS) measurement systems and methods, the phase lag in alluvial estuaries and the concept of GPS-buoys.

Chapter 3 describes the methodology behind this research. That is, the estimation of the moment of slack tide based on GPS measurements on a buoy.

Chapter 4 shows the results this research, that are the estimated phase lags in the Schelde Estuary. Furthermore, a Kalman filter algorithm is developed to filter the observed extensions of the buoy. Also the influence of the accuracy of the GPS-receiver on the detection delay is shown.

Finally, chapter 5 formulates the conclusions and gives recommendations with regard to the implementation an operational system.

Chapter 2

Background

Due to this multidisciplinary nature of this research, the literature study is divided in three subjects. The first section discusses the related literature about the concept of GPS-buoys. The next section deals with the application of this concept to the measurement of the moment of slack tide. Section 2.3 introduces the phase lag, which is the difference in time between high water level and the subsequent high water slack. Section 2.4 continues with fundamental theory about the GPS system, antenna and receiver design and operating modes.

2.1 The concept of GPS-buoys

The concept of deriving information from GPS observations on anchored or drifting buoys is developed in the last two decades. It is applied to the measurement of the vertical tide, tsunami detection, the measurement of the incident angle of tidal waves and observing the near-shore current.

The observation of the vertical tide with GPS-buoys is described by [Nagai et al., 2004] and [DeLoach, 1995]. These methods involve the design of a specially designed measurement buoy and an accurate GPS position solution, derived via post-processing or RTK. Furthermore, the observed height of the buoy is then (frequency) filtered and related to the relevant datum. This results in an observed tidal elevation in a difficult accessible environment.

Another application is the detection of approaching tsunamis. The method of an experimental system is presented by [Kato et al., 2001] which relies on one measurement buoy. An alternative implementation is presented by [Kato et al., 2000] which makes use of two buoys: a support and a sensor buoy. The latter is insensitive for wind-waves. A complete implementation is described by [Nagai et al., 2006], the system consists of a GPS-buoy, fixed GPS base station and a tsunami detection algorithm.

The measurement of the wave direction of a gravity wave with GPS-buoys is described by [Yoo et al., 2004]. The wave direction is measured with an arrayed GPS-buoy config-

uration. The principle relies on the measured phase difference of the tidal wave between the different GPS-buoys.

The near-shore current is measured with a drifting GPS-buoy by [Schmidt et al., 2003], assuming that the velocity and direction of the drifting buoy is equal to that of the water mass. The information is then applied in an analysis of sediment transport and distribution of pollutants.

Summarizing, the concept of a GPS-buoys is applied in different studies. The next section continues with the application of GPS-buoys on the measurement of the phase lag in estuaries.

2.2 Application of a GPS-buoy to observe the moment of slack tide

In the master thesis 'Phase Lags in Alluvial Estuaries' by [Haas, 2007] a new method to determine the phase lag is proposed, which is based on the observation of the position of an ATON buoy with a theodolite. The results are in comparison with a nearby tidal station very accurate. However, this conclusion is based on one determined phase lag.

The master thesis 'Observing tidal slack in the Schelde Estuary' by [Lievens, 2010] continues with the concept described by [Haas, 2007] and introduces the use of GPS to position the ATON buoy instead of a theodolite. Hereby, the potential of a GPS-buoy to observe the moment of slack tide in estuaries is shown. Since this research is closely related, the next three paragraphs discuss the measurement campaign, the methodology and the main conclusions in short notice.

During three measurement campaigns the measurement methodology is improved. On the first campaign a sensor buoy was attached to an ATON buoy. However it was shown, that the position tracks of the sensor buoy and the ATON buoy are similar, making the sensor buoy redundant. During the second campaign five buoys across the Schelde Estuary were tracked with a hand-held GPS, in an attempt to observe the phase lag across the estuary. The third measurement campaign was similar with the addition of a salinity measurement device on the ATON buoy for the validation of the phase lag.

The methods to detect the moment of slack tide are straightforward. Three methods are proposed. These methods are designed to detect the moment that the buoy is changing side with regard to centre position and do not incorporate any stochastic properties. In addition a rough implementation is done to determine the moment of slack tide based on the elasticity properties of the anchor chain, the 'elasticity method'. The results of the multiple methods show a relative large bias and spread in the determined phase lag.

It is concluded that the use of GPS-buoys for the determination of the moment of slack tide is a functional and affordable method. Further work is suggested on: the improvement of the measurement setup with regard to battery life time and measurement precision, development of a remotely operated system, and the improvement of the 'elasticity method'.

The work done by [Berghuijs & Osnabrugge, 2011] focuses on the shortcomings observed and described by [Lievens, 2010], emphasizing on the development of an autonomous

GPS system to monitor the tidal slack in estuaries. The proposed hardware architecture consisted of a Meshlium Router, which receives the data from the Waspmotes that are placed on the buoys across the estuary. The Waspmotes are specially designed sensor boards with GPS receivers. Furthermore, the Waspmotes are solar powered and use the 2.4 GHz band for the wireless communication with Meshlium Router. This system solves the technical problems described by [Lievens, 2010]. However, the system is currently not operational yet due to technical difficulties.

2.3 The phase lag

The phase lag is a key parameter in almost all analytical equations that describe the tidal movement in estuaries such as the Schelde Estuary [Savenije, 2001]. First some basic definitions are exemplified. Secondly the concept of tidal propagation in coastal water is described. Thirdly the phase lag is introduced and discussed for different types of tidal waves.

2.3.1 Tidal definitions

The vertical rise and fall of the water level is defined as the vertical tide, or simply tide. High water means high water levels, whereas low water mean low water levels. The rising period is defined as the period between low and high water, the falling period is the period between high and low water. The associated horizontal movement is referred to as the horizontal tide or tidal current. Flood currents have velocities in the direction of the tidal propagation (see subsection: 2.3.2), whereas ebb currents are opposite this direction [Stive & Bosboom, 2011].

The moment that the velocity is equal to zero is called slack. The moment of slack is related to the tidal elevation. The moment of slack water after high water is referred to as high water slack (HWS), whereas the moment of slack after low water is low water slack (LWS).

The phase difference between HW and HWS or between LW and LWS is called the phase lag ϵ. The phase lag can also be expressed in terms of minutes.

2.3.2 Tidal propagation along the shore

The tidal wave propagates (tidal propagation) in northward direction along the Dutch coast. This is in accordance with the direction of the rotary wave in ocean basins and seas in the Northern Hemisphere. Rotary waves are tidal waves influenced by the existence of a closed boundary (coastline) and the Coriolis force. For a detailed description of tidal generation and propagation the reader is referred to [Stive & Bosboom, 2011].

When the flood and ebb current are maximum around high and low water; the tidal wave has a progressive character [Stive & Bosboom, 2011]. This is characteristic of the propagation of the tide in relative deep water, where bed friction has relatively little effect on the propagation.

In the case of relative shallow water, such as an estuary, bottom friction cannot be neglected. As a result, the velocity peaks before the tidal elevation. The phase relationship between vertical and horizontal tide is very complex. Not only bottom friction, but (partial) reflections of the tidal wave introduce phase differences between velocity and elevation. Generally, the phase lag in coastal waters and basins vary between zero and $\pi/2$ [Stive & Bosboom, 2011].

2.3.3 The phase lag and tidal waves

The phase lag is discussed for the three types of tidal waves: a standing wave, a progressive wave, and a wave of mixed type.

A purely standing wave requires a semi-enclosed body, for example a harbor or a bay, where the tidal wave is fully rejected [Savenije, 2005]. The emerging wave is the sum of an incoming and reflecting wave. Figure 2.1 indicates that the high water coincides with high water slack whereas low water coincides with low water slack. In other words, the phase lag is equal to zero.
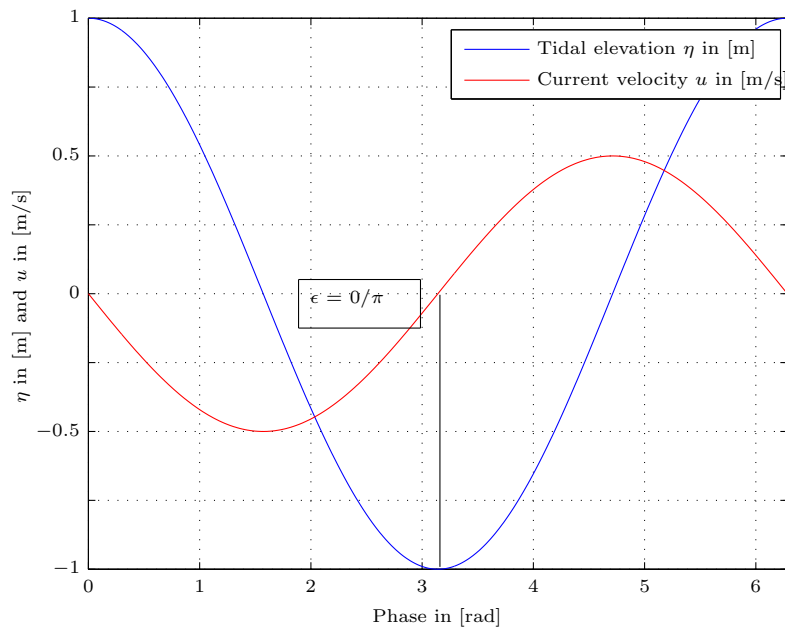
Figure 2.1: A standing wave is the sum of an incoming and reflecting wave. A purely standing wave requires a semi-enclosed body. The phase lag for a standing wave is equal to zero. This means that HW and HWS slack coincides, the same relation yields for LW and LWS.

Generally, a progressive wave occurs in a frictionless channel of infinite length and with a constant cross section. It is not necessary that the flow is completely frictionless, however the channel should have a constant cross section and be very long [Savenije, 2005]. In figure 2.2 a typical progressive wave is shown. The horizontal and vertical tide are in phase. This means that the phase lag is maximal and equal to $\pi/2$. In other words, high water and high water slack differ a period of $\pi/2$.
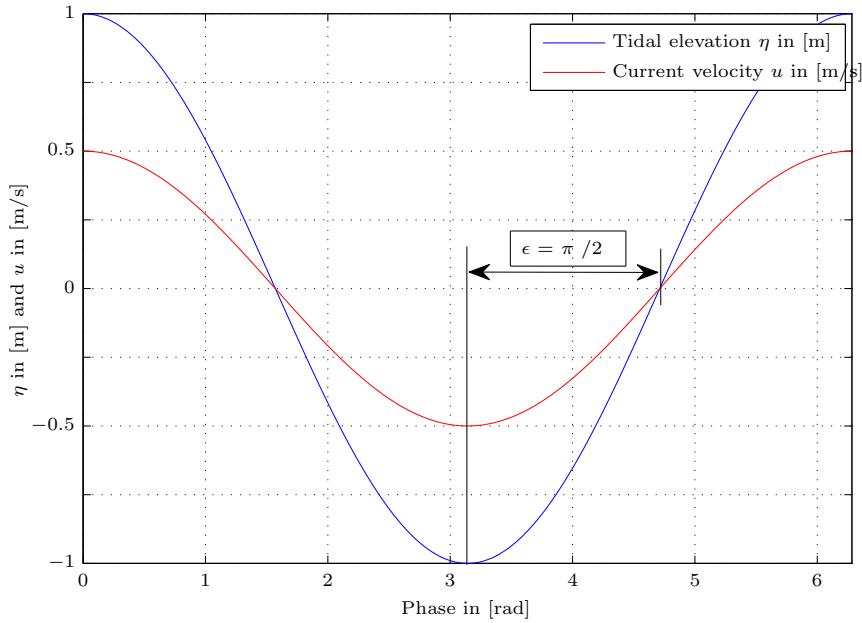
Figure 2.2: A progressive wave occurs in a frictionless channel of infinite length and with a constant cross section. The phase lag is maximal and equal to $\pi/2$.

None of these extreme situations occur in alluvial estuaries, such as the Schelde Estuary. Friction can not be neglected and the tidal waves are partly reflected instead of a complete reflection. This results in a mixed wave type. An example of a mixed wave type is presented in figure 2.3. The phase lag ϵ in alluvial estuaries lies between 0 and $\pi/2$. The moment of LWS occurs after the moment of LW but before the mean tidal level. The similar relation yields for HWS and HW. In estuaries with a semi-diurnal tide, such as the Schelde Estuary, the flow velocity slacks approximately one hour after high or low water [Savenije, 2005].

2.3.4   The phase lag equation

The most important cause for phase lag is the shape of the estuary, which is partly described by the convergence of the banks. The bank convergence causes the tidal wave to gain energy per unit width as it travels upstream. Savenije (2005) derived an equation that relates the bank convergence and the wave celerity to the phase lag. The wave celerity is the distance traveled by a crest per time unit. In this subsection the equation and the parameters that are linked to the this equation are explained. A detailed derivation is given by [Savenije, 2005].

The phase lag equation is given by:

$$\tan \epsilon = \frac{\omega b}{c(1 - \delta b)} = \frac{b}{\lambda}\frac{2\pi}{(1 - \delta b)} \tag{2.1}$$

Where ϵ is the phase lag [-]; ω is the angular velocity of the moon around the earth which
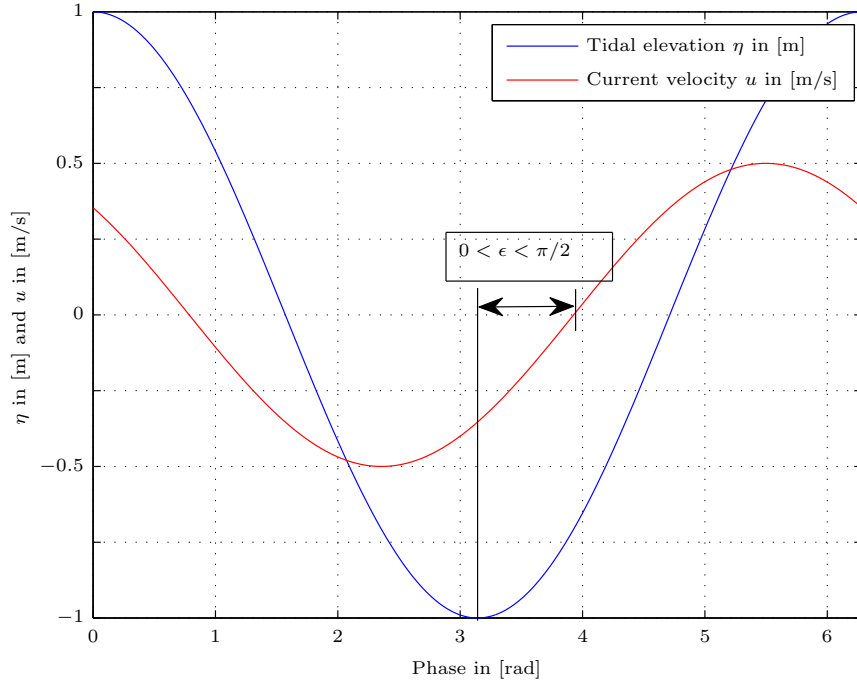
Figure 2.3: A wave of the mixed type showing the phase lag between low water and low
water slack.

causes the main harmonic component of the tide in $[rad\ s^{-1}]$; b is the convergence length
of the stream width in [m]; c is the wave celerity in [m/s]; δ is the damping rate $[m^{-1}]$,
and; λ is the length of the tidal wave [m]. This function is evaluated for the Schelde
Estuary in figure 4.26. The parameters will be discussed in the following paragraphs.

Convergence length. The Schelde Estuary is, like most estuaries, not a prismatic
channel[1]. Savenije (1992) made the assumption that the development of the width and
cross-section of alluvial estuaries can be described by means of an exponential func-
tion. This is validated for the Schelde Estuary by [Savenije, 2005]. Figure 2.4 presents a
schematic overview of an estuary with an exponentially varying width. The equation for
width convergence reads:

$$B = B_0 \exp^{-x/b} \tag{2.2}$$

Where B is the stream width in [m]; B_0 is the stream width at the estuary mouth $[m]$;
x is the land inward distance with regard to a predefined zero point in [m] and b is the
convergence length of the stream width [m].

---

[1]*Prismatic channel is a type of channel which has the same cross-section throughout the length of
channel.*
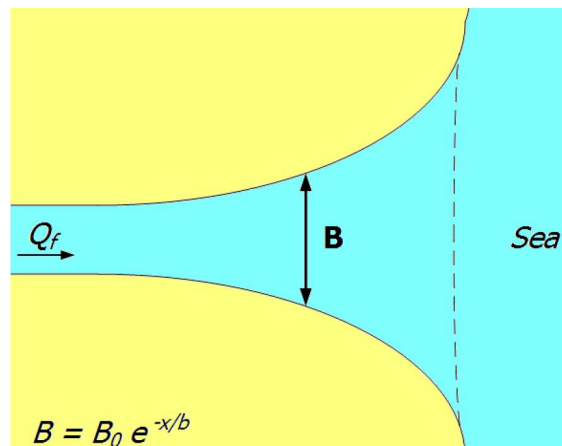
Figure 2.4: Schematic representation of an estuary with an exponential varying cross-section. Where B_0 stands for the stream with at the estuary mouth in [m]; B is the stream width in [m]; x is the land inward distance with regard to a predefined zero point in [m] and b is the convergence length of the stream width in [m]. Image taken from [Haas, 2007].

Wave celerity. The wave celerity is the distance traveled by a crest per unit time. For a standing wave, the extreme water levels are reached simultaneously along the estuary. This implies that the wave celerity equals infinity. For a progressive wave, the wave celerity is equal to the classic wave celerity, defined by $c_0 = \sqrt{gh_w}$. Where g denotes the acceleration due to the gravity in $[m/s^2]$ and h_w the wave height in [m] [Savenije, 2005].

The phase lag equation (2.1) holds for the one-dimensional exponential modelled estuary, and provides a theoretical insight. However the calculated phase lag is an average over the cross-section. Moreover the equation suggests that the phase lag is only varying along the axis of the estuary.

In reality the phase lag is highly variable in the time and space domain. The phase lag is related to the water level and water current. Unlike the water level, the water current is a highly variable in the space and time domain. Figure 2.5 illustrates the spatial variability throughout the cross-section.

The phase lag depends on many other parameters, the most important being: water depth, bottom friction, bottom slope, gradient and Coriolis forces, the river flow rate and the tidal wave characteristics. However this complex relation is extremely difficult to model. Therefore, field observations remains to be of great use.

Summarizing, this section introduced the concept and consequences (standing wave, mixed wave or progressive wave) of the phase lag. Furthermore, the relations between the phase lag, the convergence length, and the wave celerity is shown with the phase lag equation. Also, the complexity of the water current in the estuary is shown. The next section continues with GPS measurement systems and observations.
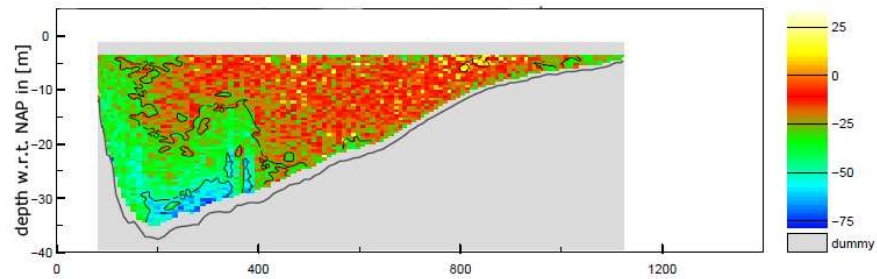
Figure 2.5: Observed current velocity in cm/s in a cross-section of 'De pas van Terneuzen' near buoy 18 on 6th July 2011 at 16:04 local time. Positive velocity values indicate an ebb current, and negative values indicate a flood current. At the bottom the flow is recently reversed, while on the surface the tide is still slacking. This illustrates the variability of the water current within a cross-section of the estuary (courtesy of RWS).

2.4   GPS measurement systems and observations

This section deals with GPS measurement systems and observations. First the operational status of the GPS system is discussed. Then in subsection 2.4.2 the relevant positioning methods and their error budgets are described. The last part continues with receiver and antenna design parameters and their influence on the pseudo-range precision.

2.4.1   Operational status of the GPS system

In this subsection a short overview of the history of the GPS system is given. But more importantly, the system performance of the modern day GPS system is discussed in detail.

Since the launch of the first GPS satellite in 1978, the GPS system has constantly been changing. In 1995 the system was declared operational. At that moment, the precision for the Standard Positioning Service (SPS) was around 100m [Misra & Enge, 2006], due to intentionally degrading of the signal called Selective Availability (SA). This was turned off in May 2000, resulting in an enormous improvement in precision [Misra & Enge, 2006]. In the upcoming paragraphs the modern day performance is discussed.

At the moment of this writing, 30 satellites are operational. All these satellites are of the Block-II(A/R/R-M/F) type, and are launched from 1990 until 2011.

The Standard Positioning Service (SPS) levels, which indicate the nominal performance of the GPS system, are determined by [Anonymous, 2008]. These performance levels are described in terms of Signal in Space User Range Error (SIS URE), also denoted as σ_{CS}. The stated nominal accuracy for the SIS URE is 3.9 meter (σ). However in reality, the GPS-system appears to perform much better than the SPS levels [Hughes, 2001].

The total error budget is called the User Range Error (URE) and is defined by [Misra & Enge, 2006] as follows:

$$\sigma_{URE} = \sqrt{\sigma_{CS}^2 + \sigma_P^2 + \sigma_{RNM}^2} \qquad (2.3)$$

Where: σ_{CS} is the standard deviation of the satellite clock and ephemeris parameters; σ_P is the standard deviation of the atmospheric propagation modeling, and; σ_{RNM} is the standard deviation of is the receiver noise and multipath.

This research focuses on determining the accuracy and precision of the position and velocity estimates, for different receivers and positioning modes. The precision of the position estimate is a function of the user range error σ_{URE} and the user-satellite geometry, which is partly represented by the Dilution Of Precision (DOP).

The DOP value depends on the user location, the number of satellites and the satellite constellation at the moment of observation. A low DOP value indicates a good geometry, while a large value indicates a poor geometry.

The influence of σ_{CS} and σ_P on the position estimate depends on the operating mode and receiver type. This is explained in more detail in section 2.4.2. Furthermore σ_{RNM} is a function of the GPS receiver and antenna design which is discussed in section 2.4.3.

2.4.2 GPS positioning modes

This section describes the different positioning modes. The first subsection deals with the observation equation, this is fundamental theory necessary for the explanation of the different positioning modes. Then in the subsections that follow, the principles and error budgets of standalone, DGPS, relative positioning and SBAS are described. The last subsection is devoted to Doppler observations.

Observation equation

To explain the different GPS positioning techniques, and their error budget in the pseudoranges, use is made of the observation equation described by [Misra & Enge, 2006]. In this equation the pseudorange is a function of the true range, (this is the separation vector between the satellite position $\mathbf{x^s}$ and the receiver position $\mathbf{x_r}$) the satellite clock error δt^s, the receiver clock error δt_r, tropospheric delay T_r^s, ionospheric delay I_r^s and receiver noise, multipath and other errors ϵ_r^s:

$$p_r^s(t) = \|\mathbf{x^s}(t - \tau_r^s(t)) - \mathbf{x_r}(t)\| + c\delta t_r - c\delta t^s(t - \tau_r^s(t)) + I_r^s(t) + T_r^s(t) + \epsilon_p^s(t) \qquad (2.4)$$

with:

$r_r^s = \|\mathbf{x^s}(t - \tau_r^s(t)) - \mathbf{x_r}(t)\|$	is the topocentric distance between the receiver and the satellite;
$\tau_r^s(t)$	is the travel time from satellite to receiver;
$\delta t_r(t)$	is the receiver clock error at time of reception;
$\delta t^s(t - \tau_r^s(t))$	is the satellite clock error at time of transmission;
$\epsilon_p^s(t)$	is the measurement error and multipath;
$T_r^s(t)$	is the tropospheric delay in meters, and;
$I_r^s(t)$	is the ionospheric delay on L1 (code) in meters.

Standalone GPS

Standalone GPS relies only on the GPS system and makes no use of other information. The data that is transmitted by the satellite is called the navigation data. This is a binary code message consisting of data on the clock bias parameters, satellite health status, ionosphere model parameters (Klobuchar Model) and ephemeris. These models contain some errors, and influence the pseudorange measurements. The following errors are present in the measured pseudorange (for a single frequency receiver):

- errors in modeling the satellite clock δt^s;

- errors in the estimated satellite ephemeris $\mathbf{x^s}$;

- errors in modeling the ionospheric delay $I_r^s(t)$, The Klobuchar Model is estimated to reduce the ionospheric effect by only 50 % [Misra & Enge, 2006];

- errors in modeling the tropospheric delay $T_r^s(t)$, and;

- errors in measuring the code pseudorange due to multipath and receiver noise $\epsilon_p^s(t)$.

To emphasize, none of these errors are mitigated and effect directly the position solution, resulting in a relative noisy and biased position. In order to obtain higher accuracies than provided by the standalone solution, the measurement errors have to be reduced. This requires a change in the mode of GPS usage from standalone to Differential GPS (DGPS).

Differential GPS

DGPS relies on the principle that errors associated with a satellite clock, satellite ephemeris and atmospheric propagation are similar for users separated by tens of kilometres, and vary slowly with time. The errors exhibit spatial and temporal correlations. However the errors tend to get decorrelated with an increasing distance between the users and an increasing time difference between their measurement epochs.

If the receiver is set-up at a known position, this receiver functions as the base station, and allows the determination of the combined error for each satellite. The second receiver, is free to roam around, in an area nearby the base station. This receiver is called the rover. The error estimates are then applied to the measurements of the rover receiver in order to mitigate the errors and improve the quality of the position estimates. This can be done nearly real time with a radio link, or in a post processing scheme.

The size of most common errors are now a directly related to the baseline length. This results in the following error budget (for a single frequency receiver):

- errors in modeling the satellite clock δt^s, are almost completely mitigated;

- errors in estimated satellite ephemeris $\mathbf{x^s}$, are almost completely mitigated;

- errors in modeling the ionospheric delay $I_r^s(t)$, are almost completely mitigated with a short baseline;

- errors in modeling the tropospheric delay $T_r^s(t)$, are almost completely mitigated, in case of a short baseline, otherwise this is a function of baseline length and altitude difference;

- errors in measuring the pseudorange code due to multipath and receiver noise $\epsilon_p^s(t)$, this is uncorrelated between the two receivers and therefore *not* mitigated.

Relative Positioning

Relative positioning is an alternate implementation of DGPS, here we will discuss the between receiver, single-difference pseudorange code measurements. This is simply called single-differences and is defined as follows:

$$\Delta p_{bs-rr}^s = p_{bs}^s(t) - p_{rr}^s(t) \qquad (2.5)$$

Where the subscript bs denotes the base station, and rr denotes the rover receiver. Substituting in the observation equation for code measurements and assuming a short distance between the base and rover station the following holds:

$$\Delta p_{bs-rr}^s = r_{bs-rr} + c \cdot \delta t_{bs-rr} + \epsilon_{bs-rr} \tag{2.6}$$

With this relative positioning approach, all common-mode errors between measurements at the two receivers are eliminated. The satellite clock error term δt^s is common and therefore cancels out. The residual errors of satellite ephemeris, ionospheric and tropospheric terms are now a function of the baseline length, and are in this case neglected, since a very short baseline is considered. The remaining terms are the separation vector between the base station and the rover receiver r_{bs-rr}, the between receiver clock error δt_{bs-rr} and the receivers noise ϵ_{bs-rr}.

SBAS GPS

The basic principle of DGPS is explained in the previous section, wide-area DGPS differs slightly from this concept. SBAS DGPS is a wide-area GPS system, moreover the corrections are transmitted from a geostationary satellite and are continentally applicable.

In the area of interest, which is often an entire continent, a network of reference stations is deployed. Measurements of each epoch are processed centrally to decompose the errors into their constituents: ephemeris, satellite clock and ionosphere. These corrections are then broadcast for each error separately, which enables the user to apply the corrections correctly depending on its location. This results in the following error budget (for a single frequency receiver):

- errors in modeling the satellite clock δt^s, are mitigated by the provided clock correction;

- errors in estimated satellite ephemeris $\mathbf{x^s}$, are mitigated by the precise estimated satellite ephemeris;

- errors in modeling the ionospheric delay $I_r^s(t)$, are mitigated significantly through a provided Grid Ionosphere Vertical Delay (GIVD) [Gauthier et al., 2001];

- errors due to the tropospheric delays $T_r^s(t)$, are mitigated significantly through the use of a-priori Minimum Operational Performance Standard troposphere model (MOPS) [Leeuwen et al., 2004];

- errors in measuring the code due to multipath and receiver noise $\epsilon_p^s(t)$ are *not* mitigated, and are still a function of the receiver design.

To conclude, SBAS offers great flexibility with a continental coverage and transmits the correction directly to a SBAS compatible GPS receiver using the same L1 radio frequency. Resulting in a significant improvement in accuracy and precision. For Europe, the European Geostationary Navigation Overlay System (EGNOS) is operational, this system is used during this measurement campaign.
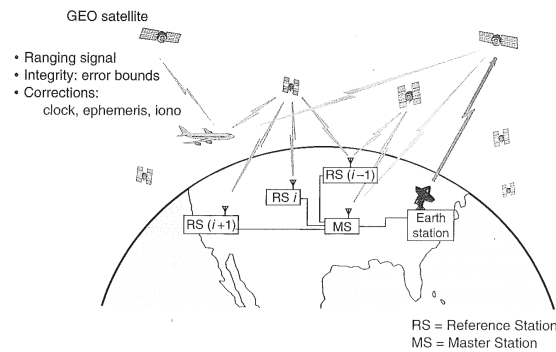
Figure 2.6: Schematic overview of a Satellite Based Augmentation System (SBAS) [Misra & Enge, 2006]

Velocity estimation using Doppler measurements

Previous studies have shown that it is possible to obtain velocity estimates with a few millimeters accuracy per second depending on the receiver quality, static or kinematic mode and the particular dynamics situation [Serrano et al., 2004]. These results are obtained using Doppler measurements.

The relative motion between the user and the satellite results in changes in the observed frequency of the satellite signal, which is caused by the Doppler effect. With a given satellite velocity, the Doppler shift can be used to estimate the user velocity.

This could also be explained from a physical point of view: there is the frequency of the carrier and the phase. The frequency is the time derivative of the phase. Or conversely, the carrier phase measurement is the integrated Doppler.

The Doppler shift is measured directly in the carrier tracking loop of a receiver or can be obtained by differentiating the carrier phase observations in the time domain (carrier-phase-derived Doppler). The receiver generated Doppler is a direct measurement of velocity, while the carrier-phase derived Doppler is a measure of the mean velocity between two epochs. This influences the characteristics of the two measurements. The receiver generated Doppler measurement is noisier than the carrier-phase Doppler, since it only measures over a very small time interval. Moreover, the carrier-phase Doppler is measured over a longer time span, averaging the random noise. This results in very smooth velocity estimate, if there is no undetected cycle slip [Serrano et al., 2004].

The Doppler shift or the observed range rate, can be written as a projection of the relative receiver velocity on the receiver-satellite line-of-sight vector. However, this measurement is biased by the receiver clock bias rate. This principle is explained with the observation equation as given in formula (2.4). More specific: the part that describes the true topocentric distance between the satellite and receiver:

$$r_r^s = \|\mathbf{x^s}(t - \tau_r^s(t)) - \mathbf{x_r}(t)\| \tag{2.7}$$

Taking the derivative with regard to the time, leaving out the time notation, denoting the derivate of the position vector $\dot{\mathbf{x}}$ as $\mathbf{v}$ (velocity) and introducing the user-to-satellite

line-of-sight vector $\mathbf{e}$ the following holds:

$$\dot{r}_r^s = (\mathbf{v^s} - \mathbf{v_r}) \cdot \mathbf{e} \tag{2.8}$$

In this equation represents $\cdot$ the inner dot product. Taking the derivative of the remaining terms of the observation equation: Tropospheric delay is a slowly varying phenomena, therefore the time derivative of T_r^s is almost zero and cancels out. The same yields for the ionospheric delay I_r^s. The satellite clock drift $\dot{\delta}(t^s)$ is minimal, and can be neglected. The time derivative of the receiver clock error $\dot{\delta}(t_r)$ can not be neglected and is denoted by b.

The pseudorange rate is now a function of the line-of-sight vector $\mathbf{e}$, the satellite velocity $\mathbf{v^s}$, the unknown receiver velocity $\mathbf{v_r}$ and the receiver clock drift b. When rewriting the formula and adding the other derivatives back into the equation the following holds:

$$\dot{p}_r^s = (\mathbf{v^s} - \mathbf{v_r}) \cdot \mathbf{e} + b + \epsilon \tag{2.9}$$

Now the method of velocity estimation described by [Misra & Enge, 2006] is followed. Equation (2.9) can be rewritten as:

$$(\dot{p}_r^s - \mathbf{v^s} \cdot \mathbf{e}) = -\mathbf{e} \cdot \mathbf{v_r} + b + \epsilon \tag{2.10}$$

Denoting $(\dot{p}_r^s - \mathbf{v^s} \cdot \mathbf{e})$ as $\dot{\tilde{p}}_r^s$, the set of measurements to K satellites can be written compactly in matrix notation as:

$$\dot{\tilde{\mathbf{p}}} = \mathbf{G} \begin{bmatrix} \mathbf{v_r} \\ \mathbf{b} \end{bmatrix} + \epsilon \tag{2.11}$$

Where, $\mathbf{G}$ indicates the matrix describing the user satellite geometry and ϵ is now a vector consisting of unmodelled errors. The velocity of the receiver can now be determined in a least squares manner from the observed Doppler based range rate measurements.

2.4.3   GPS receiver and antenna design parameters

This subsection describes the antenna and receiver design parameters. Moreover the influence of these parameters is linked to the accuracy of the pseudo-range measurement. The first paragraph deals with the design parameters for the antenna, the next paragraph continues with receiver.

Antenna design

The received power density of the GPS L1 signal is extremely small, and for a satellite with an elevation of $90°$ this is $-133.1 dBW/m^2$ [Misra & Enge, 2006]. The power in this incident signal field is captured by the receiver's antenna. Moreover, the received power is equal to the power density of the incident field multiplied by the effective area of the

antenna. The gain G_r of an antenna describes its ability to focus transmitted power in a certain direction and is expressed in decibels relative to an isotropic antenna (dBic). Isotropic antennas have a gain of 1, i.e. such antennas are equally sensitive to signals coming from any direction. This is not desirable for GPS antennas, because they only need to receive signals from above the horizon. Signals from satellites from all directions need to be received for a good performance (geometry). Therefore, the gain of a GPS antenna does not vary with the azimuth. However, the gain does vary with the elevation angle, in an attempt to strengthen the signals from satellites above the horizon as much as possible, while blocking out multipath signals. This variation is described by the elevation pattern. The next paragraphs continues respectively with patch and survey antennas.

Patch antennas. A typical patch antenna pattern is taken from [Misra & Enge, 2006] and is used to show the key design parameters. The gain is approximately +4 dBic for an elevation of 20° and above, strengthening the signal from overhead satellites. However, the gain does not decrease rapidly for elevations below the horizon. In this way multipath signals can find their way into the receiver. In other words there is no or little multipath mitigation in the antenna design.
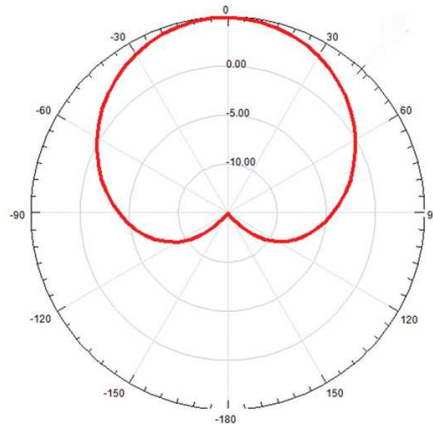
Figure 2.7: Commercial L1 antenna gain pattern for a standard patch antenna [Image taken from www.gpsworld.com].

Survey antennas. Survey antennas are designed for optimal reception of the GPS signal. The design is therefore not influenced by other design parameters such as costs, aerodynamics (automotive and aviation applications) or size. The bottom plate is made of a strong reflective material which limits the reception of multipath signals.

Also the antenna gain pattern is more sophisticated. For example the used the Septentrio PolaNt AT575-275SW survey antenna, has a 7.5 dBic gain for an elevation of 90° and decreases slowly till an elevation of 10°. From there it decreases rapidly to -7.5 dBic for an elevation of 0° [Septentrio, 2011].

Receiver design

This section is used to provide the reader with a small insight in the receiver design, that ultimately influences the ranging precision of the code pseudoranges and is based on [Braasch & Dierendonck van, 1999] and [Misra & Enge, 2006].

Receiver noise is uncorrelated between spatially separated receivers, which makes it the dominant error in source in high precision DGPS. In addition, sensitivity to thermal noise multipath and interference are highly dependent upon the receiver design. Without going into too much detail, a formula is presented relating four receiver key design parameters: the code tracking loop bandwidth, the signal to noise ratio, the pre-detection integration interval, and the correlator spacing.

The Carrier-to-Noise density ratio (C/N_0), is the ratio of the signal, to the power spectral density of the competing noise. This competing noise consists of natural thermal noise from sources outside the receiver, reflected signals, man made signals and signals from other satellites and thermal noise generated in the receiver. Natural thermal noise from sources outside the receiver are for example the sun and ground radiation. The influence of the noise from reflected and man-made signals, is heavily depended on the antenna design. The thermal noise of the antenna, pre-amplifier and the front end of the receiver set the noise figure for the entire receiver system. Components further up in the processing chain appear to have less influence [Misra & Enge, 2006]. High-end receivers are characterized by low thermal noise figures [Braasch & Dierendonck van, 1999].

The selection of the code tracking loop bandwidth B_L is a compromise between a wide bandwidth, which allows the tracking of the code during high receiver dynamics, and a narrow bandwidth which minimizes the tracking jitter due to interference.

The correlator spacing described by d is normalized with respect to one chip, therefore d is dimensionless. A smaller correlator spacing improves the tracking performance, but to a certain limit. Values of d below 0.1 do not offer any additional benefit due to filter algorithms that round the correlation peak [Braasch & Dierendonck van, 1999].

Formula 2.12 is described by [Braasch & Dierendonck van, 1999] and relates the four key design parameters to a tracking error variance in units of PRN chips squared σ_τ^2:

$$\sigma_\tau^2 \approx \frac{B_L d}{2C/N_0} \tag{2.12}$$

With:

- B_L is the code tracking loop bandwidth in Hz;

- d is the early to late correlator spacing normalized with respect to one chip, and;

- C/N_0 is the carrier to noise value in units of dB.

To summarize, the following relation can be defined: A higher C/N_0 results in a better range precision and also a lower B_L and d influence the precision in a positive way.

Another important design parameter is the signal bandwidth, which in the previous formula is assumed to be infinite. However spread spectrum signaling provides a processing gain proportional to the signal bandwidth. This results in steeper slope of the correlation function which improves the ranging precision [Misra & Enge, 2006]. High-end receivers use the radio signal with a bandwidth varying between 2-20 MHz while low-end receivers are often limited to the minimum of 2 MHz [Braasch & Dierendonck van, 1999].

Chapter 3

Materials and methods

3.1 Introduction

This chapter describes the methodology behind this research. That is, the estimation of the moment of slack tide based on GPS measurements on a buoy. All processes and intermediate results are represented schematically in a work flow diagram (see figure 3.1).

The first part of this research is a static measurement campaign. This is a performance analysis of different GPS receivers in combination with different antennas and operating modes. The results are used in a later stadium to choose an appropriate GPS receiver, antenna and operating mode for the operational system. The tested GPS receivers, antennas, location and methodology are described in section 3.2.

The second part is a dynamic measurement campaign, which is designed to measure the buoy's dynamics as accurately as possible. The measurement set-up, location and processing techniques are discussed in section 3.3. The acquired dataset is used for the: calibration of the mathematical model; the stochastic description of the buoy's dynamics, and; the development and application of a methodology to estimate the moment of slack tide.

The third part is a simplification of the buoy's motion, as is measured during the dynamic measurement campaign, from three to one-dimensional. The methodology and the assumptions are discussed in section 3.4. The results are then used in the next part.

The fourth part is the development of the mathematical model of the buoy's dynamics due to tidal current. This is described in detail in section 3.5. The model is then calibrated against the one-dimensional observed motion. In this section also the reasoning behind the definition of the moment of slack tide is described.

In the fifth part all intermediate results are combined. The estimation of the moment of slack tide is based on hypothesis testing. It requires the stochastic model of the buoy's motion, the stochastic description of the GPS receiver's position estimates and the relation between the buoy's extension and the moment of slack tide.

The determination of the phase lag is described in short notice in subsection 3.7. This is actually no more than determining the time difference between maximal/minimal tidal elevation and the moment of slack tide. This is necessary for the last phase where the results are validated and compared.

The last phase describes a comparison of the determined phase lag against the observed phase lag with ADCP measurement of RWS and a one dimensional modelled approximation of the phase lag throughout the estuary.
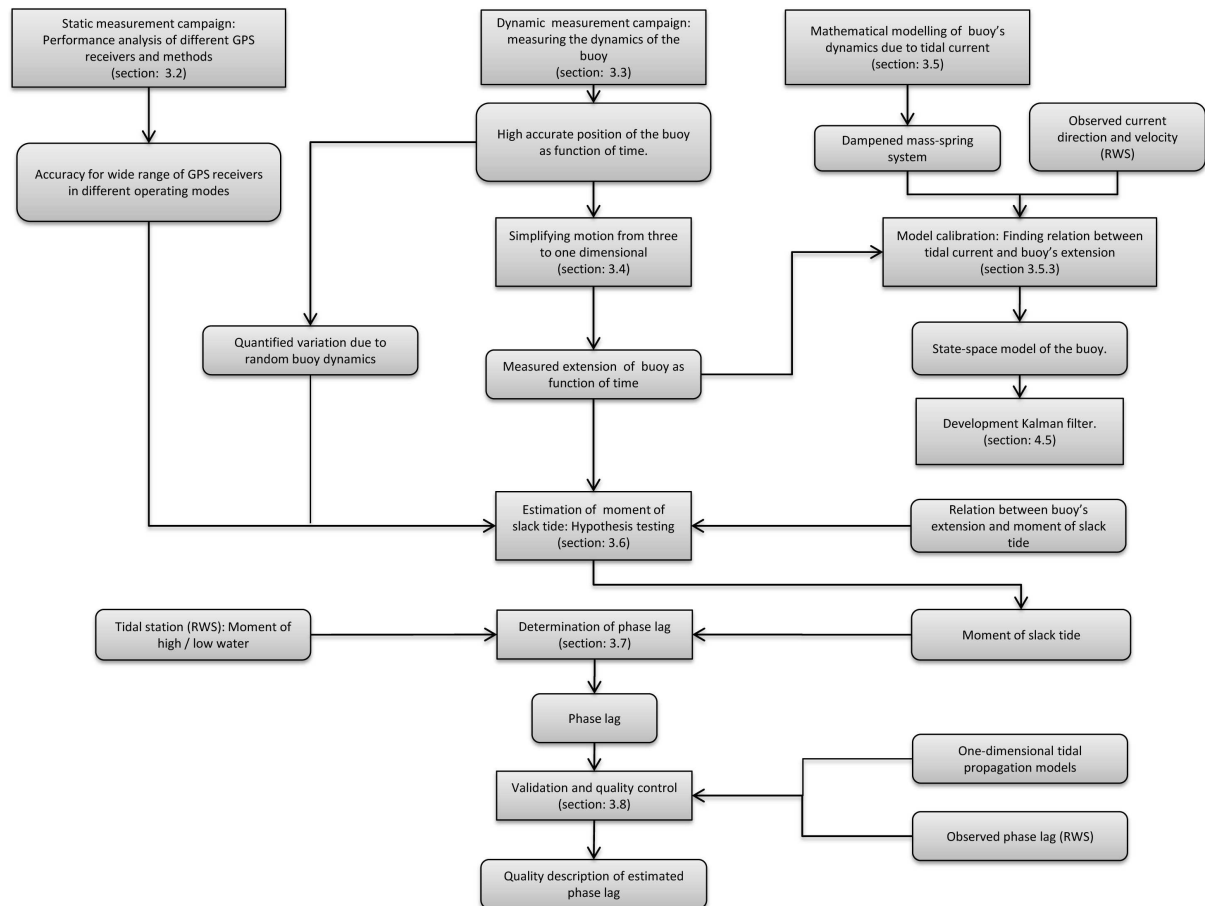
Figure 3.1: Work flow diagram, square shapes indicate a process, while round shapes indicate an (intermediate) result. The research starts with three independent parts, represented by the three main columns. In the last part, all intermediate results are used for the estimation of slack tide. The end result is the estimated phase lag with an associated quality description.

3.2 Static measurement campaign: Performance of different GPS measurement systems and methods

This section describes the methodology of the static measurement campaign. Based on this measurement campaign the performance of different GPS measurement systems and

methods is determined. The section is divided in four subsections, the first subsection
describes the tested GPS receivers and provides an introduction of their expected perfor-
mance. The second subsection provides the reader with an overview of the test location.
Then in subsection 3.2.4 the methodology behind the performance analysis of the posi-
tion estimates is given. The same is done in subsection 3.2.5 for the velocity estimates.
The last part is only applicable for the Septentrio AsteRx1 receiver and describes the
methodology to determine the performance of Doppler measurements and displacements.

3.2.1   The analyzed GPS receivers

Two GPS receivers are made available by the section Mathematical Geodesy and Posi-
tioning from the Faculty of Aerospace Engineering, Delft University of Technology. The
Garmin GPS 76 C(S)x (SiRFstarIII chipset) with the Garmin GA27C external antenna
and the Septentrio AsteRx1 1.4.0. The section Watermanagement from the faculty of
Civil Engineering provided the Vincotech A1084. In table 3.1 an overview is given of
the GPS receivers and their operating modes. Important properties of these systems
are discussed in the next paragraphs. For a complete overview of all the GPS systems
specifications see the appendix A.1.

GPS Receiver	Standalone	SBAS	dGPS	Doppler Observation
Vincotech A1084	n/a	yes	n/a	n/a
Garmin GPS 76 C(S)x	yes	yes	not used	n/a[1]
Septentrio AsteRx1 1.4.0	yes	yes	yes	yes

Table 3.1: Static measurement campaign: GPS measurement systems and methods.

Vincotech A1084

The Vincotech A1084 is a compact, low power consumption GPS engine board, based on
the SiRFstarIII chipset (see figure 3.2). The receiver is developed for automotive, marine
and personal navigation. It tracks up to 20 GPS satellites on the L1 frequency (1575.42
MHz). Furthermore it's SBAS enabled, for Europe this is the EGNOS system, which is
operational since 2009. The stated precision of the two-dimensional position estimates by
the manufacturer is 3.5m σ (SBAS disabled) and 1.75 m σ (SBAS enabled) [Vincotech,
2011]. The output format is, as expected for a low end GPS receiver, only NMEA.

Garmin GPS 76 C(S)x

The Garmin GPS 76 C(S)x is a complete GPS system, with a power supply, screen and
interface designed as a total outdoor navigation solution. This system is based on the
SiRFstarIII chipset. This means, that it is a L1 single frequency receiver, which can
track up to 12 satellites at a time. For this research, the main difference with regard to
the Vincotech A1084, is the external antenna; the Garmin GA27C. An external antenna

---

[1]However, the velocity estimate are supposedly based on Doppler observation (this could not be verified
by Garmin), the resolution of the NMEA string is insufficient for this research.
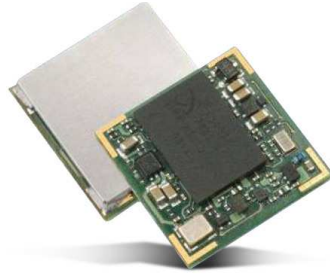
Figure 3.2: Vincotech A1084 GPS receiver with a built-in passive patch antenna element, note that the dimension is only 15 by 15 mm [Source: Vincotech].

results in a better sky view and likely less multipath. Also for this system, the output format is only NMEA [Garmin, 2011].

Figure 3.3: Garmin GPS 76 C(S)x with the Garmin GA27C antenna. Designed as a total outdoor navigation device [Image source: Garmin]

Septentrio AsteRx1 1.4.0

The Septentrio AsteRx1 is a high-end geodetic receiver (see figure 3.4), designed for high-performance single frequency applications. It features 24 single frequency channels for all-in-view GPS, Galileo and SBAS tracking. Furthermore the AsteRx1 incorporates a high update rate, low latency and a low power consumption. Another advantage is the output of the raw measurements, which can be used in a post processing algorithm. Also, it offers the possibility to set the receiver up in a differential mode. The specified position accuracies depend upon the positioning mode. These are in horizontal and vertical position accuracies (σ): 1.7 m and 3 m for standalone, 0.7 m and 1.2 m in SBAS mode and 0.35 m and 0.65 m in DGPS configuration. Besides, it is capable of producing Doppler observations, that is an extremely accurate measurement for velocity, in the order of mm per second [Septentrio, 2006].

Two antennas are available, an high performance survey antenna, this is the Septentrio PolaNt also known as the AT575-275SW, and a patch antenna (AT575-70W). The PolaNt is a lightweight high precision survey antenna for survey applications. This high-gain

antenna is designed to reduce noise and multipath. Furthermore it is capable of receiving the GPS and GLONASS signal. The patch antenna on the other hand is not suitable for survey applications, and is more vulnerable for multipath signals, but is significantly cheaper. How this influences the position estimates is part of this research.

Figure 3.4: Middle: Septentrio AsteRx1 1.4.0, professional L1 GPS receiver. Left: compatible patch antenna with a diameter of 38 mm. Right: the high precision survey antenna with a diameter of 178 mm. [Image source: Septentrio]

3.2.2 Location of the static measurement campaign: NMi

In Delft, the Netherlands, the NMi (Netherlands Metrology institute) offered the possibility to make use of their observation platform. A perfect location with a clear sky view and geodetic markers, for which the coordinates of the markers are accurately determined. Three systems are evaluated simultaneously on different observation points as figure 3.5 indicates.
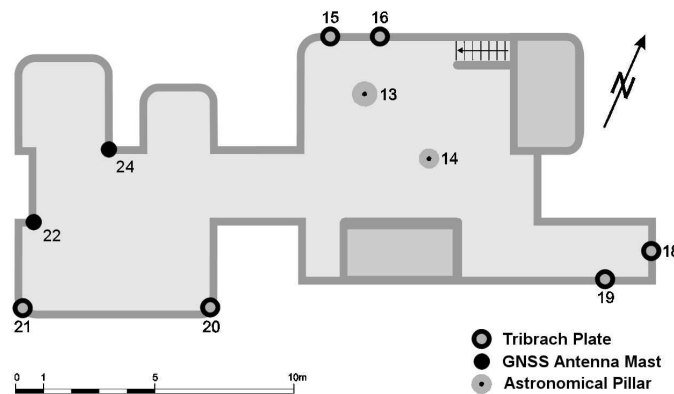
Figure 3.5: Location of the static measurements, this platform is located on the roof of the NMi building, Delft, The Netherlands. The Vincotech A1084 is installed on marker 14, the Garmin GPS 76 C(S)x on marker 13 and the Septentrio AsteRx1 1.4.0 on marker 15. On marker 22, the Septentrio PolaRx2 is installed, within the DPGA network also known as DLF5, and is used as a base station for the DGPS set-up.

3.2.3   Definition of accuracy and precision

In section 4.1 the accuracy and precision of the receiver's position estimates are discussed. The precision of the GPS receiver coordinate estimates is quantified by a standard deviation σ. The empirical standard deviation is defined as follows:

$$\sigma = \sqrt{\frac{1}{n-1} \sum_{i=1}^{n} (x_i - \overline{x})^2} \tag{3.1}$$

Where n represent the number of measurements, x_i can be an estimate of the local north, east or upward component and $\overline{x}$ is the empirical mean of these estimates. The empirical mean $\overline{x}$ is defined as follows:

$$\overline{x} = \frac{1}{n} \sum_{i=1}^{n} x_i \tag{3.2}$$

The bias μ is defined as the difference between the empirical mean of the measurements and the ground truth. The 95% intervals indicate the value below which, 95% of the absolute difference values between the position estimates and the groundtruth can be found. The reference value for this figure is the ground truth (marker coordinates), and hence the difference between the estimate and groundtruth is is a measure of accuracy.

3.2.4   Determination of the accuracy and precision from the receiver's position estimates

This subsection is divided in two paragraphs, the first paragraph describes the measurement set-up and measurement analysis for the position estimates obtained with a GPS-receiver in a standalone or SBAS mode. The second paragraph continues with the measurement set-up and analysis of a DGPS configuration.

Standalone and SBAS

The three receivers are installed on three geodetic markers (see figure 3.6). The coordinates of the markers are precisely known in ITRF2005 at the times of the experiments, which in millimeter accuracy. I.e. the precision of the reference coordinates are several orders of magnitude better than the position estimates of the receivers. Furthermore, the antenna height and phase reference point of the antenna are taken into consideration with millimeter accuracy.

The three receivers are logging simultaneously for a period of 24 hours at a rate of 1 Hz, starting at 00:00:00 UTC. The position is logged in geodetic coordinates i.e. latitude (ϕ), longitude (λ) and height (h) using the WGS84 ellipsoid.

As indicated above, the reference coordinates are Cartesian using ITRF2005 and the receiver position estimates are in geodetic coordinates using WGS84. The geodetic coordinates are transformed into the same Cartesian system as the reference coordinates.

Figure 3.6: Measurement set-up on the NMi roof, the Septentrio AsteRx1, the Vincotech 1084A and the Garmin are set-up at different marker locations.

Now it is possible to determine the differences between the given reference coordinates and the obtained position estimates. These differences are then transformed in a local North (N), East (E) and Up (U) system. The bias, standard deviation and 95% interval for the north, east and up component are calculated. Furthermore a three-dimensional 95% interval is determined to provide a practical all-in value.

This methodology is applied for the standalone and SBAS solution of the AsteRx1, the Garmin GPS 76 GS(X) and the Vincotech A1084. The methodology for the DGPS solution differs slightly and is discussed in the next paragraph.

DGPS - Relative Positioning

In this case, the AsteRx1 is configured as a kinematic rover. For the base station the Dutch Permanent GNSS Array (DPGA) station DLF5 is used, which is a permanently installed Septentrio PolaRx2 receiver with a Leica AR25 antenna. For the processing, again a period of 24 hours is taken with a measurement rate of 1 Hz.

The processing is done in Trimble Geomatics Office [Trimble, 2001], a commercial package used for surveying. The coordinates of the PolaRx2 are accurately known, since the antenna is installed on marker 22 (see figure 3.5). The (RINEX) files of the AsteRx1 are marked as kinematic. In this way, the same situation as on the buoy is simulated, otherwise the processing software makes use of the redundant measurements resulting in a better position estimate. Now every measurement epoch is considered separately resulting in a kinematic position solution. In section 2.4.2 the theory behind the single differences pseudorange code solution is discussed, this dataset is processed using the that concept.

For each epoch a new position solution is determined. The determination of the measurement statistics is done in the same manner as described in the previous paragraph.

3.2.5   Determination of the precision of the receiver's velocity estimates

The precision of a receivers velocity estimates is determined by assuming that the velocity of a static receiver equals zero, and that the outcome of this assessment is equal for a quietly fast moving receiver.

Again, it is necessary to make a distinction between the receivers. The velocity of the Garmin GPS 76 GS(X) and the Vincotech A1084 are determined by taking the first derivative of the position estimates numerically across adjacent epochs. This was necessary due to the limited precision of the NMEA velocity string. An example of the NMEA GPVTG string:

```
GPVTG,054.7,T,034.4,M,005.5,N,010.2,K*48
where:
        VTG              Track made good and ground speed
        054.7,T          True track made good (degrees)
        034.4,M          Magnetic track made good
        005.5,N          Ground speed, knots
        010.2,K          Ground speed, Kilometers per hour
        *48              Checksum
```

From the above it follows that the resolution of the NMEA output is 0.1 km/h, which is too coarse for this purpose.

The Septentrio AsteRx1, uses an internal algorithm to estimate the velocity directly based on receiver generated Doppler observations [Septentrio, 2006]. This principle is explained in section 2.4.2, also the differences between the receiver generated Doppler measurements and carrier-phase-derived Doppler are explained. The carrier-phase-derived Doppler algorithm is implemented in MATLAB using raw carrier phase observations in RINEX format.

3.3   Dynamic measurement campaign: capture the buoy's dynamics

This section describes the methodology of the dynamic measurement campaign as performed between 1 and 5 July 2011. The objective of this campaign is to measure the dynamics of an ATON buoy during several tidal cycles. With a GPS measurement set-up, for which the position measurement precision is so good, that compared with the buoy dynamics, it could be neglected. In that way, the results of this campaign can act as a ground truth motion of the buoy.

3.3.1   Motivation for buoy 18

The area of interest is predefined at the start of this research, this is the Schelde Estuary. The choice of the ATON buoy that is being investigated is based on practical and theoretical reasoning.

The location of the buoy within the estuary is important for the outcome of this research. As explained earlier, the main objective of this research is to measure the moment of slack tide. With the proposed methodology this is only possible if the buoy is subject to one dominant current direction. In other words, the buoy must be located in a main flood or ebb channel and separated from a short-circuit channel which connects the ebb and flood channel and other disturbing factors. The channel located in front of Terneuzen is an ebb channel [Van Veen, 1950].

On the practical side, other aspects influence the choice of the buoy. At the moment, several designs of ATON buoys are in use. Only the larger steel buoys can safely accommodate this measurement system. Furthermore, this research is dependent on the willingness of Multraship, to tender the research crew to the buoy. The office and location of the tender boat is the city of Terneuzen, therefore the use of a buoy within the vicinity of Terneuzen is advantageous. Besides, the accuracy of a kinematic baseline solution is highly correlated with the baseline length. The combinations of these two reasons favor buoys in the direct vicinity of Terneuzen.

Based on the reasoning described above, the most suitable buoy for this dynamic measurement campaign is number 18. This buoy is located in the ebb channel near Terneuzen (and the base station) and is well separated from the short-circuit channel. Moreover, due to the steel structure it can accommodate the measurement system. This was not the case for buoy 16, 20 and 28. The buoys ZE-6, ZE-5, WPT-2 and PT-4 are located in or near a short-circuit channel, and are therefore not suitable.

3.3.2   Motivation for the equipment

The choice of the right equipment for this campaign is critical. The equipment needs to be reliable in the harsh environment of the Schelde Estuary. Besides the reliability, the GPS receivers' observations need to be precise and accurate. Furthermore, the power consumption should be minimal, since the receiver on the buoy is powered by a battery.

Therefore, after taking many GPS systems into consideration during the static measurement campaign, the safe choice is made to perform this dynamic measurement campaign with Trimble R7 receivers. This receiver is not evaluated during the static measurement campaign, since it is per definition too expensive for the implementation of this system in the future. However, it does provide a reliable and high accurate dataset during the research phase. The Trimble R7 receiver is water and dust proof according to the IP67 standard. Moreover, the power consumption is only 2.5W and the precision of the position estimates can reach the order of millimetres for a kinematic baseline solution. The full specifications of the Trimble R7 receiver can be found in the appendix A.1.

3.3.3   Measurement set-up: short kinematic baseline

The two Trimble R7 receivers are set-up in a kinematic baseline. The base station is installed at the roof of the office of Multraship in Terneuzen. Providing a clear sky view for the antenna, while the receiver is installed safely inside the office.

The rover receiver is mounted on the buoy. To protect the receiver against the harsh environment it is placed in a specially designed measurement box. For the power supply
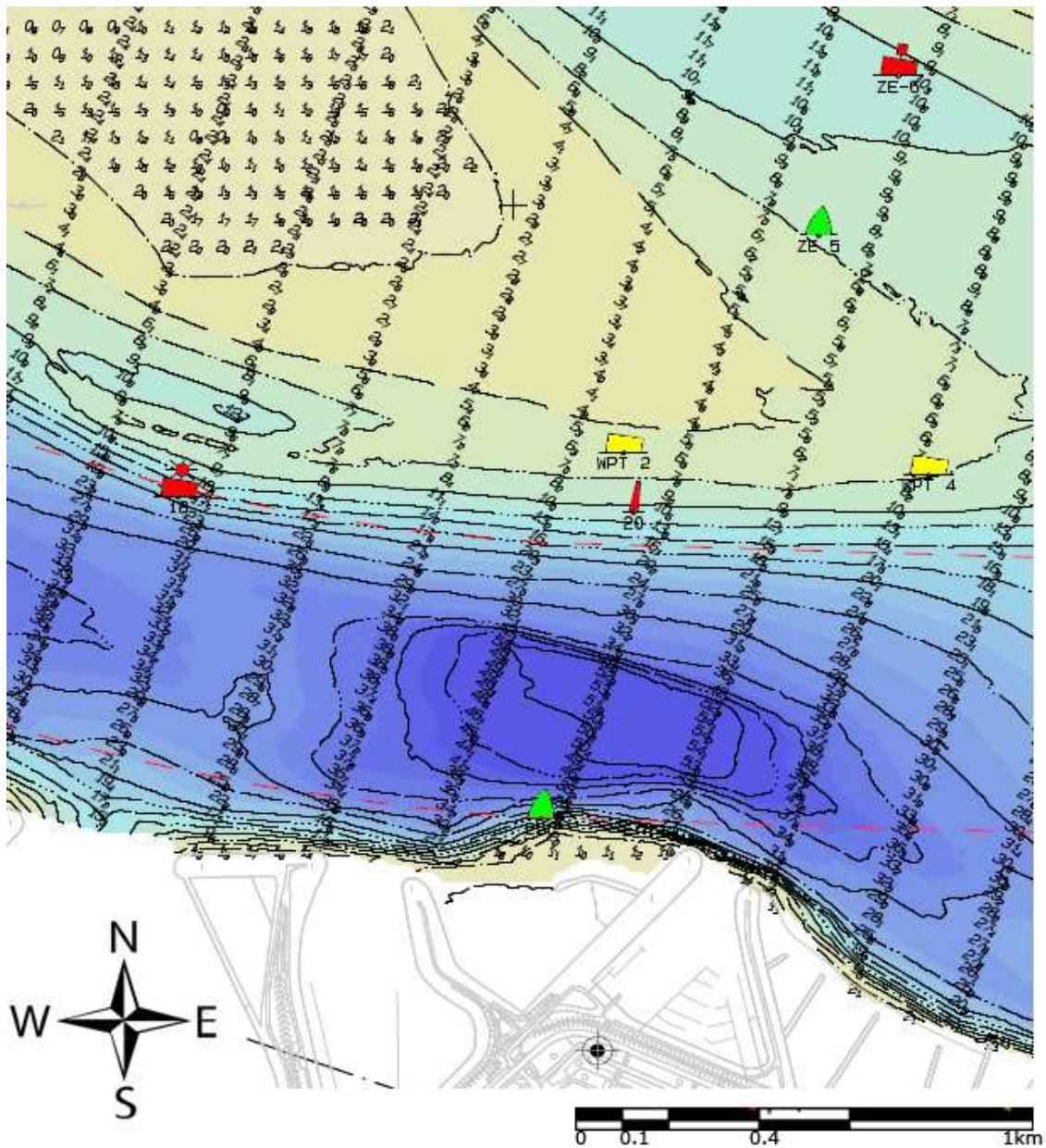
Figure 3.7: This map is a selection from the internal hydrographic chart of RWS. This hydrographic map shows the depth with contour lines, colours and sounding numbers. Furthermore , it shows the position of the ATON buoys and the outline of Terneuzen. The green, red and yellow symbols indicate the location of different types of ATON buoys. With the cross hair the location of GPS base station is marked [Image source: Rijkswaterstaat].

a large external battery with a capacity of 28Ah is connected to the receiver. This provides the GPS receiver with enough power for nearly 5 days. The antenna is mounted with a range pole to the buoy, such that the antenna has a clear sky view. The measurement box is firmly mounted inside the cage of the ATON buoy. The complete installation can be seen in figure 3.8.

3.3.4 Processing strategy

An accurate estimate of the position of the base station needs to be established. Next, the highly precise position estimates of buoy 18 are obtained via processing of the short kinematic baseline.

The coordinates of the base station are obtained by submitting the RINEX files to the Automatic Precise Point Positioning Service (APPS) of the Jet Propulsion Laboratory (JPL); this post processing method uses precise clock and orbit data. The results are precisely estimated coordinates of the point, with a detailed accuracy description of the of coordinates.

Once the coordinates of the base station are known, the kinematic baseline is processed on a epoch by epoch basis with software made available within the section of Mathematical Geodesy and Positioning, which is based on the LAMBDA-method. For validation purposes the dataset is also processed with a commercial software package: Trimble Geomatics Office.

The LAMBDA-method is considered to be the best method available for integer carrier phase ambiguity resolution. However, starting from noisy measurements, even the best method can not guarantee a 100% succes rate [Joosten & Tiberius, 2002]. The success rate of ambiguity resolution with dual-frequency data on a short baseline generally exceeds a level of 99.9% [Joosten & Tiberius, 2002]. This implies that 1 in a 1000 times ambiguity resolution fails, resulting in a wrong integer ambiguity resolution, which in turn results in a biased position estimate.

These biased position estimates need to be removed, since they can influence the subsequent analysis in a negative manner. First a smoothed position track is created with a moving average filter and subtracted from the raw position track, removing the trend. Second, each position estimate is tested against a threshold driven by a significance level. If the position estimate is significantly larger, it is considered to be a biased position estimate and removed from the position track. During this process no more than 0.01% of the position estimates will be removed.

Figure 3.8: Buoy 18 is located near Terneuzen. For this buoy the Trimble R7 GPS receiver is mounted inside the cage. The Trimble Zephyr antenna is installed on a range pole on top of the buoy. Note the eddies induced by the tidal current around the buoy.

3.4 Simplifying the buoy's motion: from a three-dimensional position to a one-dimensional extension

This section describes the reasoning and methodology behind the simplification of the complex three-dimensional movement of a buoy to one-dimension. Without neglecting significant 'information' with regard to the tidal current and moment of slack tide.

The first subsection describes the necessary assumptions. Principle component analysis is applied in subsection 3.4.2 to simplify the buoy's dynamics from a two-dimensional position to a one-dimensional extension in the dominant current direction. The last section describes a method to determine the centre position, i.e. the point of zero extension.

3.4.1 Assumptions with regard to the simplification

The buoy is subject to different forces. Not only to the tidal current, in which the interest lays, is responsible for the dynamics of the buoy. But also to the forces that are delivered by the wind induced waves, creating a high frequency oscillating movement in all three directions. The influence of the wind on the path of the buoy can be neglected according to [Lievens, 2010]. A low frequency oscillating motion in the upward direction is created by the tidal elevation. Finally, the chain produces a counter force to keep the buoy in its position. The track of the buoy as a result of these forces is indicated in figure 3.9.

Firstly the motion in the local upward direction is neglected. Although it contains information about the tidal elevation and the (significant) wave height, it is not of interest for the tidal current. Besides, due to small amplitude ($\pm 2m$) it cannot be measured with sufficient accuracy using a low budget GPS receiver.

However, the tidal elevation does influence the maximum extension in the local horizontal direction. Figure 3.10 shows a schematic representation of this situation. With the application of Pythagoras' theorem the maximum amount of extension for high and low water can be calculated. The following dimensions of buoy 18 are used: the length of the chain L_{chain} is 40 m [Rijkswaterstaat, 2011a]; the draft of the buoy equals approximately 2 m; the water depth with respect to NAP Z equals 15 m [Boon, 2011], and; a tidal amplitude T equals approximately 2 m [Rijkswaterstaat, 2011b]. This results in a maximum extension for high water E_{HW} of 38.5 m and for low water E_{LW} 37,0 m. The difference in maximum extension, due to the difference in tidal elevation equals 1,5 m.

Since it is not possible to measure the tidal elevation with a low cost GPS receiver and for the case of simplicity the height component of the buoy's motion is neglected. However, the influence of the tidal elevation on the extension of the buoy during the moment of slack tide is much larger (two times the tidal amplitude) and is incorporated in the definition, this is described in section 4.6.2.

Secondly, the assumption is made that the direction of the (tidal) current is constant during ebb and flood. Moreover, these currents are assumed to be opposite. This may however be not the case, due to an opposite Coriolis force on the ebb and flood current, morphological interaction, inertial and gradient effects [Stive & Bosboom, 2011].

However, the results of a 12 hour measurement campaign of RWS on the current in 'de Pas van Terneuzen' indicates the following: the direction of ebb stream varies only with a
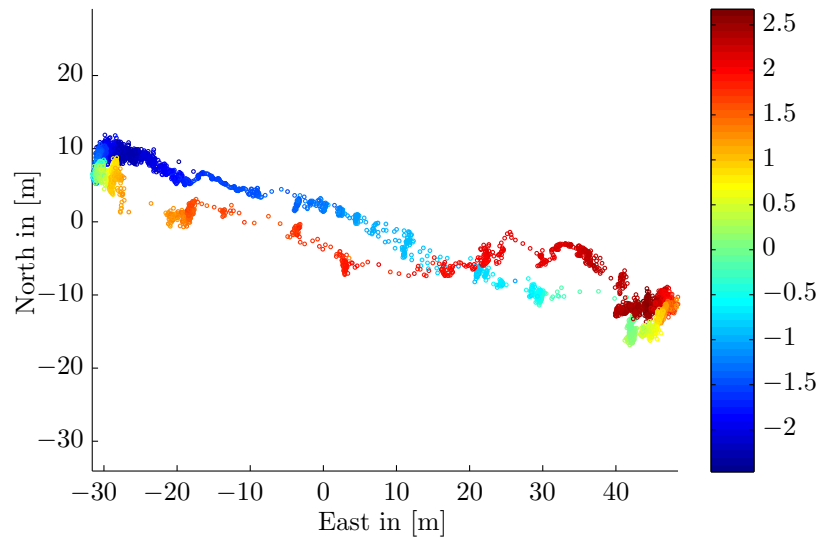
Figure 3.9: Movement of buoy 18, during one complete tidal cycle from high water to high water on 2nd July 2011, plotted at a 60 second interval. The marker indicates the elevation of the buoy in meters. Note that the buoy only moves significantly in one direction. This is the dominant current direction, perpendicular to that only a small scale movement is observed. The origin represents the empirical mean of the position.
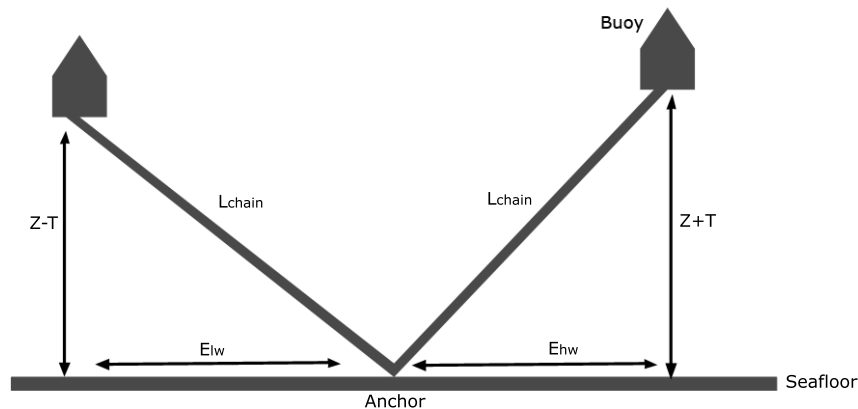
Figure 3.10: Schematic representation of the maximum extension E during high water hw and low water lw. Where L_{chain} indicates the length of the anchor chain, Z denotes the depth with regard to the chart datum and T denotes the tidal elevation related to to the chart datum.

maximum of 5° and the same yields for flood stream. Moreover, the ebb and flood stream are opposite [Rijkswaterstaat, 2011b].

Similar results are observed in the dynamic measurement campaign on buoy 18 (see figure 3.9). It is important to note that the largest motion ($\pm$ 80 m) is observed in one direction.

This is the dominant current direction. On the perpendicular direction only a small scale movement is observed. This movement is caused by a complex system of forces and is not of interest for the tidal current. Therefore, it is possible to simplify the buoy motion from two to one dimension without loosing 'information' with regard to the tidal current. The methodology is described in the next subsections.

3.4.2   Principle component analysis: estimation of the dominant current direction

The central idea of principal component analysis (PCA) is to reduce the dimensionality of a data set of interrelated variables, while retaining as much as possible of the variation present in the data set. The dataset is transformed in a new set of variables, the principle components. The principle components are uncorrelated and ordered so that the first few retain most of the variation present in all of the original variables [Jolliffe, 2002].

This principle is used to transform a two-dimensional horizontal position of the buoy to a one-dimensional extension. It is assumed that the first principle component describes the extension of the buoy due to the dominant current direction. Given a set of points in Euclidean space, the first principal component corresponds to a line that passes through the multidimensional mean and minimizes the sum of squares of the distances of the points from the line [Pearson, 1901].

The matrix X is a n x p matrix of n centralized observations of p attributes [Teunissen et al., 2005]. In this particular case there are two attributes: the north and east coordinates of the buoy which are observed during the dynamic measurement campaign. The matrix X consists out of vector of east coordinates E and a vector of north coordinates N, which are both centralized:

$$X = \left[\begin{array}{cc} E & N \end{array} \right] \tag{3.3}$$

Now we determine the eigenvalue decomposition of the variance-covariance matrix, $Q_{xx} = U\Lambda U^T$. Where Λ is the diagonal eigenvalue matrix (with eigenvalues $\Lambda_1, ..., \Lambda_n$ along the diagonal) and U the matrix of unit eigenvectors [Teunissen et al., 2005].

The eigenvectors point in the principal axes directions of the Q_{xx} ellipse and the eigenvalues give the lengths of the principal axes [Teunissen et al., 2005]. The principal components Y of X are now defined as:

$$Y = X \cdot U \tag{3.4}$$

The first column of Y consists of the variation in the direction of the first principle component, that is the extension with regard to the empirical mean in the dominant current direction. The second column can be seen as the residuals after the transformation.

3.4.3   Determination of the centre point

The anchor position of the buoy is an important parameter for the estimation of the moment of slack tide. It defines the centre point, i.e. the point of zero extension. RWS

stores the anchor positions in a database. Unfortunately, the accuracy is often insufficient [Lievens, 2010]. Also in this case it appears that the anchor position is biased. Therefore, an alternative for the estimation of the centre point is proposed.

The previous section results in an extension of the buoy with regard to the estimated dominant current direction. However, as indicated, this extension is related to the empirical mean. This empirical mean represents however not the point of zero extension. Due to the asymmetry of the tidal current the buoy remains longer in the extension related to the ebb stream than the flood stream (see figure 3.11). Therefore the ordinary time average (emperical mean) of the extensions results in a centre position that is shifted in the direction of this ebb stream. This problem is also described by [Lievens, 2010].

The following method holds under the assumption that the data is pre-analyzed and the outliers are removed from the dataset (see subsection: 3.3.4). The extension during a number of tidal cycles n is observed. For each complete tidal cycle, denoted by the subscript i, from high water slack till low water slack the the maximum extension E_i^{max} and the minimum extension E_i^{min} are determined. Since multiple tidal cycles are observed, creating redundancy, the average of the centre point $\bar{c}$ is described by:

$$\bar{c} = \frac{1}{n} \sum_{i=1}^{n} \frac{E_i^{min} + E_i^{max}}{2} \tag{3.5}$$

This method, considering the redundancy, enables quality control of the estimated centre point. The variation of the centre point is part of the results.
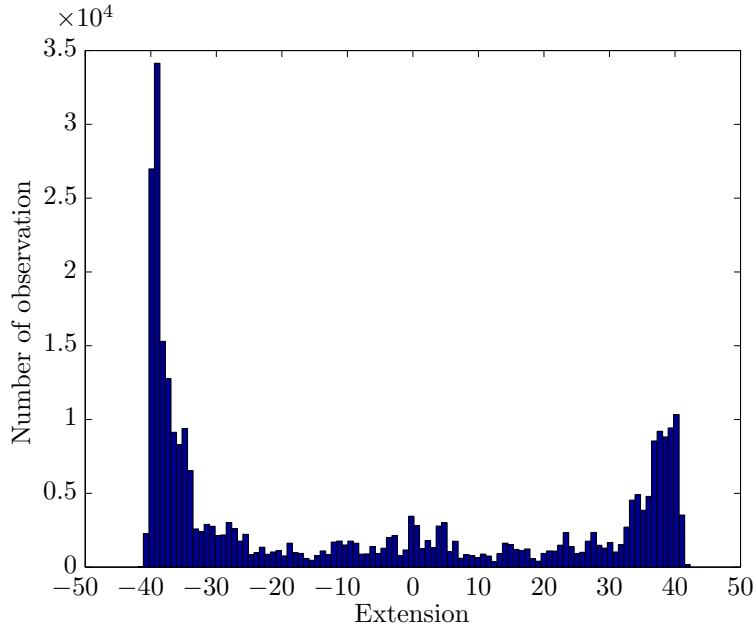

Figure 3.11: This histogram shows the extension of buoy 18 with regard to the centre point on 1-5 July. A negative extension indicates a position of the buoy related the ebb stream. The purpose of this graph is to note that the buoy remains longer in the position related to the ebb stream. This is due to inequality of the tidal current.

3.5   Mathematical description of the buoy's dynamics due to tidal current

In order to retrieve insight in the buoy's dynamics caused by the interaction between the buoy, the chain and the current, a mathematical model is created. Based on this model assumptions about the relation between the moment of slack tide and the buoy's extension are made. Furthermore it is used to assess appropriateness of a linear chain force model.

This section starts with a prediction of the buoy's motion as a function of time. Then in subsection 3.5.2 this is used for the development of the mathematical model. The basis of this model is a mass-spring system. Subsection 3.5.3 describes the calibration process of the mathematical model against the observed extension.

3.5.1   Model of motion

The forces that are acting on the buoy are related to the extension with regard to the centre position. Four critical points are discussed, those four points are indicated in figure 3.12. In the next paragraphs those points are discussed during a tidal period starting and ending just after the moment of slack tide.

Origin (1).   Imagine that the water flow recently reversed and the buoy's extension is equal to zero. For any change in extension caused by the flow force the chain acts as a friction force, limiting the acceleration of the buoy. This is an unstable situation; the buoy will move to position 2.

Chain becomes active (2).   At this point the force of the chain becomes an active force. The water flow velocity is still increasing.

Dynamic state of equilibrium (3).   The scenario between position 2 and 4 is a dynamic state of equilibrium. The chain is lifted off the seabed and acts as an active force (spring). If the extension increases the force of the spring increases as well. Therefore, the water flow force is counteracted by the chain force.

Maximum extension (4).   At this moment the force of the chain can go in theory to infinity, it is impossible for the buoy in the water current to extend any further than this position. It is uncertain if this maximum extension really occurs.

Dynamic state of equilibrium (3).   The buoy is again in a dynamic state of equilibrium. At this moment the water flow force is decreasing, as result the buoy is pulled back to position 2 by the active chain force.
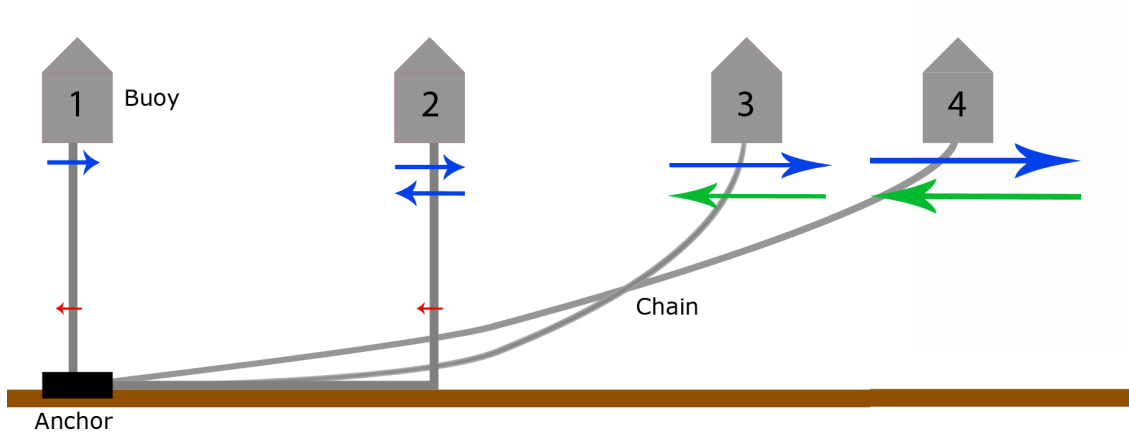
Figure 3.12: The buoy in its four critical positions. Blue arrows indicate the force created by the friction of the current on the buoy, this is the flow force F_{flow}. Red arrows indicate a friction force $F_{friction}$ between the chain and the sea floor. Green arrows indicate an active spring force, created by the chain, denoted by F_{chain}. The two blue arrows in position 2 indicate that during this position the current is changing its direction. Position 2 is the extension related to the the moment of slack tide.

Moment of slack tide (2). This is the most critical extension of the buoy with regard to the moment of slack tide. The chain stops delivering an active counterforce and becomes passive again. Following this reasoning one would expect that this is the moment of slack tide. The extension at this point is equal to the length of the chain plus the draft of the buoy minus the water depth minus the tidal elevation, the later two are both with regard to the chart datum. From here the **flow reverses** and the buoy moves back to position 1. The acceleration is limited by the passive friction force of the chain.

3.5.2 Mathematical model

The extension of the buoy is modelled as a one-dimensional dampened mass-spring system as described in [Meriam & Kraige, 2006]. The mass-spring-damper system is described as a second order differential equation. Furthermore this section is an extension of the work done by [Berghuijs & Osnabrugge, 2011].

The buoy is subject to forces created by the tidal current and is denoted by F_{flow}. The flow and therefore F_{flow} is assumed to be constant along the path of the buoy and does only depend on time. F_{flow} is the driving force of the system.

Next, the buoy is held in its position by a chain, firmly anchored to the sea bottom. The chain more or less counteracts the motion of the buoy. As explained in the previous section the chain delivers two types of forces an active force and a passive force. The active force F_{chain} is modelled as the spring in the dampened mass-spring system. F_{chain} is modelled with a spring constant k, but k is actually a function of x, where x denotes the extension. The passive force created by the friction between the chain and the sea floor is modelled as a damping coefficient c, dependent on the extension's rate of change.

Actually the above forces are just the (local) horizontal component (of the force exerted by the chain). The general equation of a mass-spring system is described :

$$m\ddot{x} + \underbrace{c\dot{x}}_{F_{friction}} + \underbrace{k(x)x}_{F_{chain}} = F_{flow}(t) \tag{3.6}$$

Modelling the driving force

F_{flow} is a function of the effective surface of the buoy A_b, the drag coefficient c_d, the density of the water ρ and the velocity of tidal current v. The following yields:

$$F_{flow}(t) = \frac{1}{2}Ac_d\rho(v(t))^2 \tag{3.7}$$

Where A is the horizontal surface which is dependent on the shape and the draft of the buoy. The draft of the buoy is obtained with a simple displacement calculation. The necessary dimensions and mass m of the buoy are obtained via [Rijkswaterstaat, 2011a]. The drag coefficient c_d for a cylindrical shape in seawater is determined at 1.3 in accordance with [Mott, 2009].

The only remaining term is the velocity of the tidal current. In a first approximation this can be modelled as a harmonic function. With v_{max} the maximum current velocity and T the period of the investigated tidal cycle.

$$v(t) = v_{max}\cos\omega t \tag{3.8}$$

However, the flow velocity is much more complex. Especially in an estuary like the Schelde. Therefore the *observed* flow velocity from field measurements of RWS is used.

The velocity and direction of the tidal current is measured in 'De Pas van Terneuzen' on the 6th of July with an ADCP during a 12 hour measurement campaign of RWS. This results in dataset that completely describes the velocity and direction of the current throughout the entire water column. In the appendix B.1 a map can be found that presents the location of this section relative to buoy 18. These data are then shifted in time using the moment of high and low water, under the assumption that the current velocity of 6 July is equal to that of 1-5 July.

Modelling the chain force

The chain force is difficult to describe. It depends on the weight, length and form of the chain along the depth. As indicated in paragraph 3.5.1 it is expected that the chain behaves as a function of the buoy's position. Therefore, multiple mathematical descriptions are investigated.

Linear behavior. The most simple representation of the chain force is to assume that the spring constant k is constant.

$$k(x) = k \tag{3.9}$$

This results in combination with equation 3.6 in a linear spring force approximation.

Higher order behavior. Succeeding the linear approximation, higher order approximation are more likely to represent the behavior of the chain as is described in paragraph 3.5.1.

$$k(x) = |f(x^p)| \tag{3.10}$$

Where $p + 1$ is the order of the spring force model, a range from the second to the eight order is investigated.

Exponential behavior. In addition the spring constant is modelled as an exponential function:

$$k(x) = |f(a^x)| \tag{3.11}$$

Where a is a calibration constant of this exponential spring model.

The complete implementation of the mathematical mass-spring system is implemented in MATLAB.

3.5.3 Calibration of the model on the observed extension of buoy 18

The mathematical model is calibrated on the observed extension of buoy 18, in order to get reasonable values for the damping coefficient c and spring constant k. Furthermore it is used to determine if the spring force behaves linear.

The average extension as a function of time is taken for the multiple tidal cycles. This is then smoothed using a moving average filter. With a manual iterative process it is attempted to minimize the residuals between the model and the observations. This is done for each mathematical representation of the chain force separately. The results are calibrated mathematical mass-spring models of the buoy and the residuals.

3.6 Estimation of slack tide: hypothesis testing

The estimation of slack tide based on GNSS measurements on a buoy is only possible using the position of the buoy, this followed from the dynamic measurement campaign. The observed velocity of the buoy is extremely low (in the order of 1 or 2 cm/s) and buried under the noise caused by the oscillating movement of the buoy and the measurement noise in case of a medium performance GPS receiver.

Therefore a relationship between the extension of the buoy and the moment of slack tide is necessary. In order to incorporate the stochastic properties of the measurement technique the proposed methodology relies on composite hypothesis testing.

Definition of the hypothesis. The hypothesis is defined to test if the extension of the buoy is significantly larger or smaller than the extension related to the moment of slack tide. Two statistical hypotheses of the moment of slack tide are defined, one for high water slack and one for low water. For high water slack the following holds:

$$H_0 : \underline{E} \sim N(E > E_{st}^{hw}, \sigma^2) \text{ versus } H_a : \underline{E} \sim N(E \leq E_{st}^{hw}, \sigma^2) \qquad (3.12)$$

Thus for high water slack, the null hypothesis H_0 states that the unknown extension E of the buoy is larger than the extension related to the moment of slack tide E_{st}^{hw}. While the alternative hypothesis H_a states that buoy's extension E is smaller than the extension related to the moment of high water slack E_{st}^{hw}. In this case just a *single* observation E has to decide between H_0 and H_a. This is a binary detection problem.

The critical region K will be taken left-sided. k_α is the starting point or boundary of the critical region K. As soon as a sample E is smaller than this critical value k_α, the null hypothesis is rejected: accept H_0 if $E \geq k_\alpha$ and reject H_0 if $E < k_a$.

The similar relation yields for low water slack:

$$H_0 : \underline{E} \sim N(E < E_{st}^{lw}, \sigma^2) \text{ versus } H_a : \underline{E} \sim N(E \geq E_{st}^{lw}, \sigma^2) \qquad (3.13)$$

The null hypothesis H_0 states that the unknown extension E is smaller than the extension related to low water slack E_{st}^{lw}. The alternative hypothesis H_α states that unknown extension E is larger than the extension related to low water slack E_{st}^{lw}. This results in a right-sided critical region K.

Now the concept of the hypothesis testing is defined, values for E_{st}^{hw} and E_{st}^{lw}, σ^2 and the significance level α need to be determined, which is part of the results.

3.7 Determination of phase lag

The main part of this research is the estimation of the moment of slack tide. However it is necessary to relate this to the tidal elevation in order to determine the phase lag. The previous section relates a position to the moment of slack tide. This position is observed

at a certain moment in time, denoted by M_{hws} and M_{lws}. As explained in the background the phase lag for high water is defined as follows:

$$\epsilon_{hw} = M_{hw} - M_{hws} \qquad\qquad (3.14)$$

And for low water:

$$\epsilon_{lw} = M_{lw} - M_{lws} \qquad\qquad (3.15)$$

The tidal elevation data from the measurement station of RWS in Terneuzen is used to determine the moment of high and low water. Under the assumption that the tidal elevation of buoy 18 is equal to that of Terneuzen. With application of equation 3.14 and 3.15 the high and low water phase lags are determined.

3.8   Validation of the estimated phase lag

This section describes the validation of the estimated phase lag against the results of SOBEK, which is an one-dimensional hydraulic modelling system designed for complex estuaries, and the phase lag equation. Furthermore are the estimated phase lags validated against the results of an ADCP measurement campaign performed by RWS.

3.8.1   Modelled phase lag: SOBEK and the phase lag equation

[Nguyen, 2008] applied the SOBEK model and the phase lag equation in the Schelde Estuary on 29 June 1998 (spring tide). These results need to be interpreted carefully, because they are based on many assumptions, simplifications, see [Nguyen, 2008] for more details. The computed phase lags are cross-sectional averages. The estimated phase lags from this research hold only for the location buoy 18 and do not represent a cross-sectional average. However, it useful to determine if the estimated phase lag is in the right order of magnitude. The average estimated phase lag is plotted against the results of the SOBEK model and the phase lag equation.

3.8.2   ADCP observations in "De Pas van Terneuzen"

Ideally, the results are validated against current observation, made in the close vicinity of the investigated buoy. However, there are no current measurement stations in the shipping lane. Due to the high spatial variability of the current are observations along the shore useless.

However, a 12 hour measurement campaign is performed by Rijkswaterstaat on 6 July 2011. During this measurement campaign the magnitude and direction of the current throughout the entire cross section of "De pas van Terneuzen" is measured at a 10 minute interval using a ADCP. From this data the high water phase lag ϵ_{hw} and low water phase ϵ_{lw} is determined by finding the moment in time where the current slacks. The phase lag follows then directly from equation 3.14 or 3.15.

Although, the data is measured on 6 July 2011, which is one day after the dynamic measurement campaign it is assumed that results are valid for 1 till 5 July 2011. This is justified by the fact that tidal amplitude is almost equal for these 6 days. Figure B.1 shows the location of the ADCP measurements in relation to buoy 18. The current velocity that is perpendicular to buoy 18 is used and the depth at the both locations are almost similar, this partly justifies the assumption that this current velocity is equal to the current experienced by buoy 18.

Chapter 4

Results and discussion

This chapter presents the results of this research. Section 4.1 starts with the results of the static measurement campaign, that are the error plots and accuracy descriptions of the tested GPS receivers in combination with different antennas and operating modes.

The next section continues with the results of the dynamic measurement campaign on buoy 18. Furthermore, it presents the position and elevation of the buoy during several tidal cycles. Then in section 4.3 the results from the PCA transformation are presented. These results are used for the calibration of a dampened mass-spring system in section 4.4.

Section 4.4 shows the results of modelling the extension of the buoy as a dampened mass-spring system. Moreover, the quality of the model fit is shown. In section 4.5, a side-step in this research is made. In this section a Kalman filter is developed and some initial filter results are shown. However, these results function as a showcase and are not used in the next section.

The input parameters for the hypothesis testing are defined in 4.6, also the influence of the significance level, the GPS receiver and antenna is shown. Later on is the moment of slack tide related to the moment of high or low water to obtain the phase lag, which is the end result of this research (section 4.7). The latest section validates the results against an analytical phase lag equation, the SOBEK model and current observations.

4.1 Static measurement campaign: performance of different GPS measurement systems and methods

This section presents the results of the 24 hours static measurement campaigns on the NMi platform. The results are divided in two subsections, subsection 4.1.1 shows the position plots of the three receivers, while subsection 4.1.2 deals with the velocity plots.

4.1.1   Accuracy and precision determination of the receivers position estimates

In this subsection, the north, east and up components of the position estimates are plotted against time (UTC). The positions are relative to the accurately determined position coordinates of the marker. Furthermore the bias μ, standard deviation σ and the 95% interval in the north, east and up component are given. Also the three dimensional 95% interval is calculated in order to present a full statistical summary of the receiver performance.

In figure 4.1 the position plot of the Vincotech A1084 with EGNOS corrections is presented. A large bias in the east component is observed. However, this component shows the smallest standard deviation, in comparison with the north and height component. Also, the height component is significantly biased and shows position jumps up to 8 meters. The three dimensional 95% interval is 8.5 meters, which appeared to be the largest in this research.
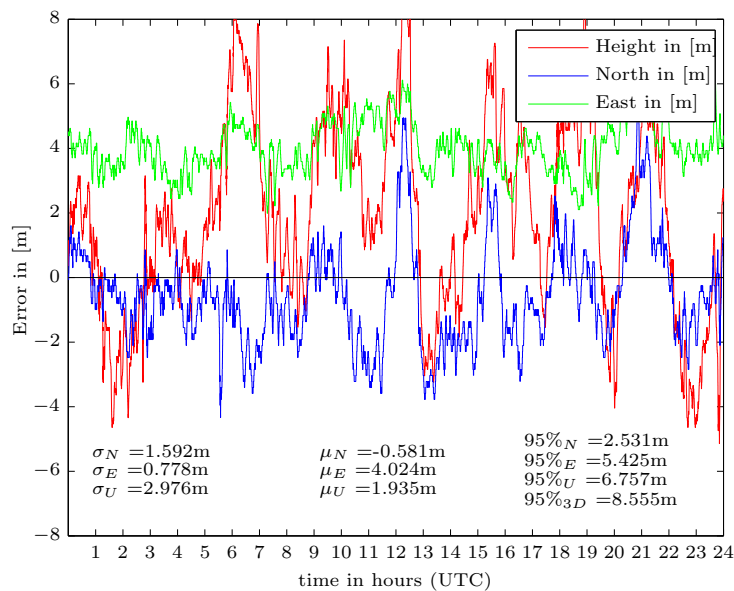
Figure 4.1: Error plot of the position estimates of the Vincotech A1084 with EGNOS corrections. The GPS receiver was installed at marker 14 on 12 June 2011. The figure shows a 24 hours plot of the north, east and up component. Furthermore the 95 % position interval, the standard deviation σ and the bias μ for each component is given.

The Garmin GPS 76 C(S)x without EGNOS corrections (see figure 4.2) shows a similar bias for all components, while the standard deviation for the height is the largest with a value of 2.3 m, this lies within the expectations, considering the weak geometry for this component. Moreover, the 95% interval is around 5.8 meters, which is better than the Vincotech A1084 with EGNOS corrections.

If the Garmin is configured to enable EGNOS corrections, a small improvement in the bias can be observed. For the north, east and up component the bias is respectively 0.7,

Figure 4.2: Error plot of the position estimates of the Garmin GPS 76 C(S)x in standalone mode on 16 May 2011. In this graph the north, east and up components are plotted against time. Also, the figure indicates the statistics.

0.9 and 1.3 meter. While the standard deviation remains almost unchanged. However the 95% interval shows some improvement and decreased till 5.2 meters (see figure 4.3). Unfortunately, position jumps up to 8 meters occured several times, which indicates that the EGNOS position estimates are less stable.
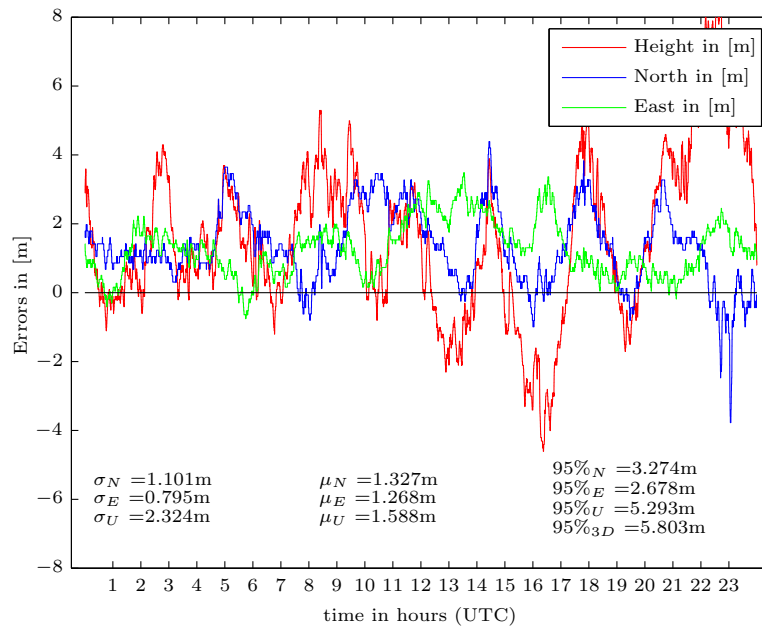
The Septentrio AsteRx1 1.4.0 with the PolaNt antenna in standalone mode shows a better standard deviation (see figure 4.4) then the previous receivers. Also the bias is significantly improved. Furthermore the 95% interval is around 2.7 meters, which is an huge improvement compared to the previous receivers.

The measurement is repeated using the same configuration but now using a patch antenna, the graph is left out in this report for the cause of redundancy. However, the $95\%_{3D}$ interval is almost doubled, and a significant increase in the standard deviation and bias is observed. This indicates influence of the antenna choice on the accuaracy of the position estimates.

In figure 4.5 the EGNOS corrections are enabled for the AsteRx1 with the PolaNt antenna. This results in a significant mitigation of the Signal in Space User Range Error (SIS URE). Now the performance of the AsteRx1 becomes clear, the standard deviation dropped down for the north, east and up component until respectively 0.26, 0.21 and 0.44m. The bias improved to decimeter level. This all resulted in a 95% position interval of 1.19 m. Furthermore, in order to apply EGNOS corrections, the receiver is configured to apply carrier smoothing of the pseudorange code measurements. The noisy code-based measurements are smoothed by the very accurate estimates of the delta pseudoranges. This is not applied in standalone or DGPS mode.
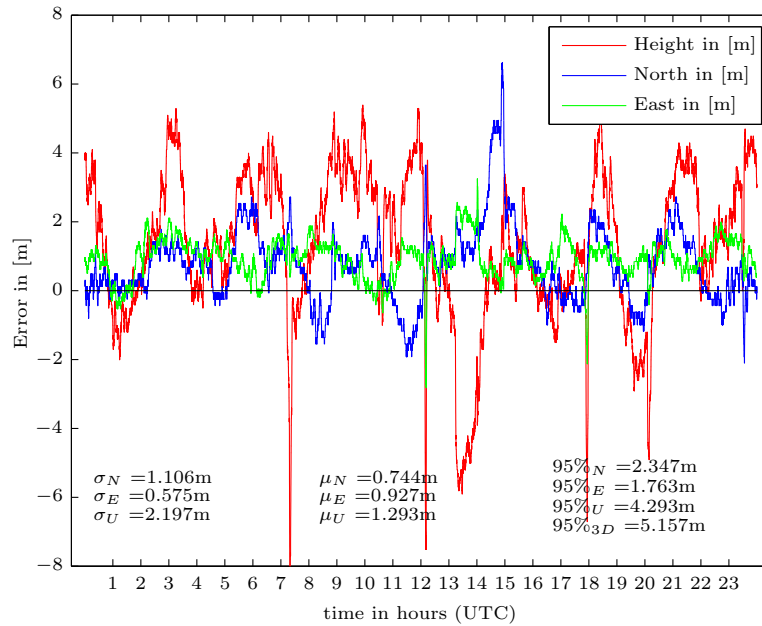
Figure 4.3: Error plot of the position estimates of the Garmin GPS 76 C(S)x with EGNOS corrections on 3 May 2011. In this graph the north, east and up components are plotted against time. Also, the figure indicates the statistics.

The same measurement is repeated with the patch antenna, as opposed to the PolaNt antenna. This results in an increase of the $95\%_{3D}$ of almost 50%. Furthermore the standard deviation and 95% intervals in the north, east and up are significantly larger. However the bias shows only a small increase. Moreover, EGNOS corrections do improve the statistics of the AsteRx1 with a patch antenna, which was not the case with Garmin.

Figure 4.6 shows the results of the AsteRx1 in DGPS configuration. The considered baseline is not longer than 15 meters. What remains is the measurement precision of the code observation. It's important to note that the remaining bias equals practically zero, therefore the complete SIS URE is mitigated. The standard deviation for the north, east and up component is respectively 0.53, 0.36 and 0.82 meters, with a 95% interval of 1.8 meters. It is important to note that no carrier-smoothing of the code measurements is applied, and in addition, the noise in the code pseudoranges is multiplied by a factor $\sqrt{2}$. This is caused by the appliance of *two* receivers that produce independent noisy code measurements that do not cancel out in the single difference solution.

As this set-up completely mitigates the SIS URE, it is used to determine the difference in antenna performance (PolaNt vs the patch antenna). A significant increase in the 95% intervals is observed. For example the $95\%_{3D}$ increased from 1.8 m till 2.7m. Furthermore the AsteRx1 with the PolaNt antenna resulted in an unbiased solution, this is not the case with the patch antenna.

The results of the performances analysis of the receivers in different modes are summarized in table 4.1.

Figure 4.4: Error plot of the position estimates of the Septentrio AsteRx1 in combination
with the PolaNt antenna in standalone mode on 27 April 2011. The north,
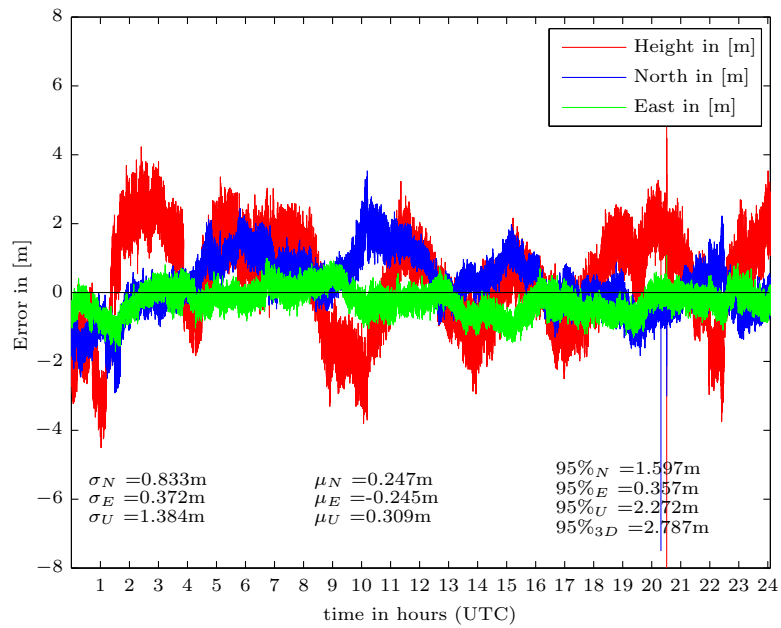east and up components are plotted against time. The figure also indicates the
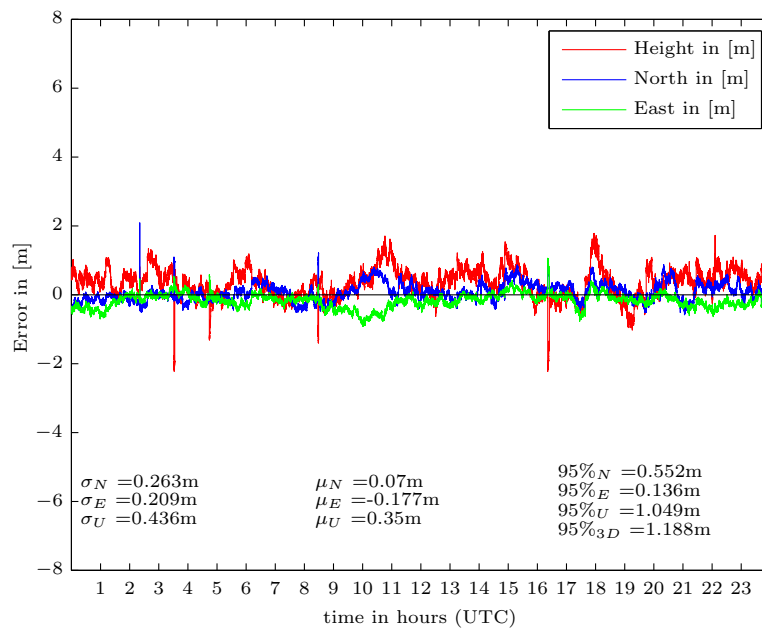statistics.

Figure 4.5: Error plot of the position estimates of the Septentrio AsteRx1 in combination
with the PolaNt antenna and EGNOS corrections on 3 May 2011. The north,
east and up components are plotted against time. The figure also indicates the
statistics.

Figure 4.6: Error plot of the position estimates of the Septentrio AsteRx1 with a single difference code solution. The Septentrio AsteRx1 with the PolaNt antenna is configured as a rover, while the Septentrio PolaRx2 as a base station. This results in a DGPS configuration with an extremely small baseline (15m). This is a single differences code position solution, processed in Trimble Geomatics Office. The observation date is 3 May 2011.

Receiver	Mode	$95\%_N$	$95\%_E$	$95\%_U$	σ_N	σ_E	σ_U	μ_N	μ_E	μ_U	$95\%_{3D}$
Vincotech A1084	SBAS	1.592	0.778	2.976	1.592	0.778	2.976	-0.581	4.02	1.935	8.555
Garmin GPS 76 C(S)x	standalone	3.247	2.678	5.293	1.101	0.795	2.324	1.327	1.268	1.589	5.803
	SBAS	2.347	1.763	4.293	1.106	0.575	2.197	0.744	0.927	1.293	5.157
Septentrio AsteRx1	standalone	1.596	0.357	2.72	0.833	0.372	1.384	0.247	-0.245	0.309	2.787
AT575-275SW	SBAS	0.552	0.136	1.049	0.263	0.209	0.436	0.070	-0.177	0.350	1.188
survey antenna	SD Code	0.819	0.526	1.319	0.533	0.354	0.817	-0.056	-0.050	-0.013	1.823
Septentrio AsteRx1	standalone	2.045	1.417	0.878	0.947	0.799	1.478	0.513	0.068	-1.432	4.429
AT575-70W	SBAS	1.081	0.425	1.697	0.451	0.290	0.705	0.391	-0.084	0.454	1.877
patch antenna	SD Code	1.238	0.746	1.554	0.772	0.491	1.162	-0.003	-0.063	-0.262	2.717

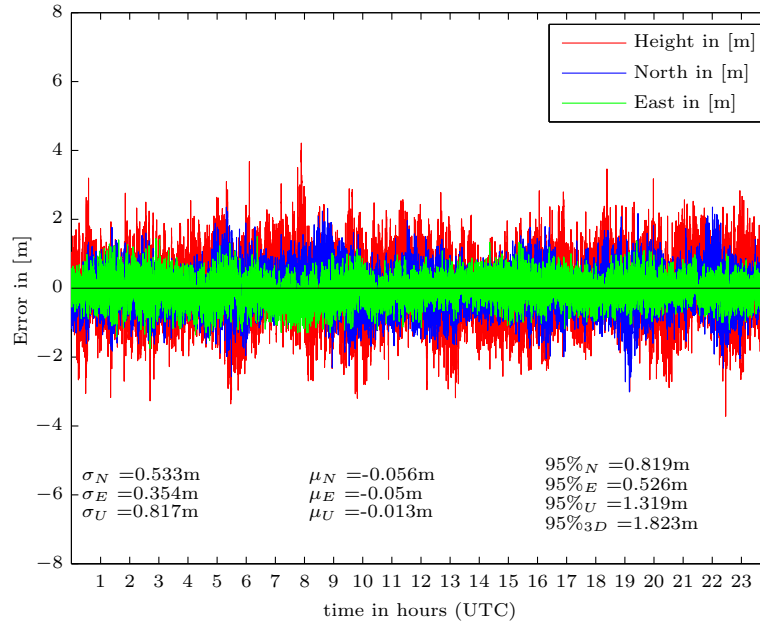**Table 4.1:** Summary statistics of position estimates from the receivers

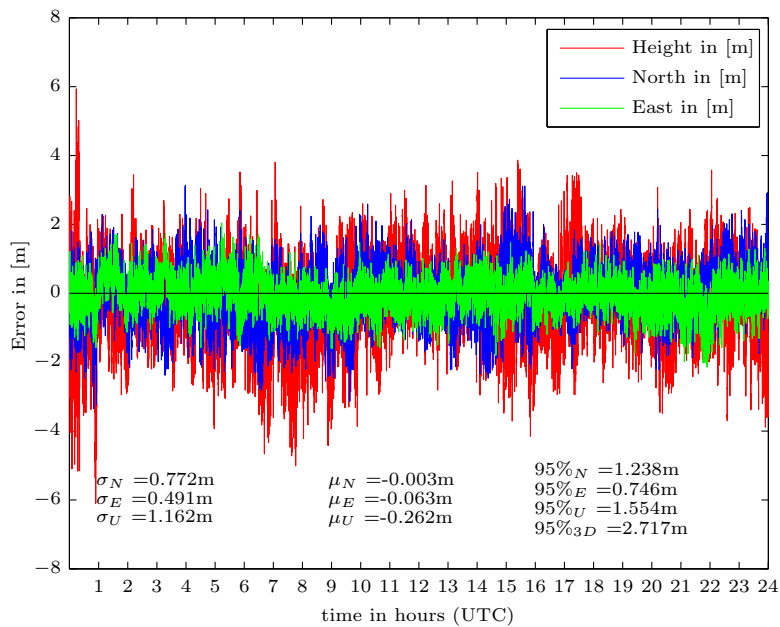**Figure 4.7:** Error plot of the position estimates of the Septentrio AsteRx1 with a single difference code solution. The Septentrio AsteRx1 with the patch antenna is configured as a rover, while the Septentrio PolaRx2 as a base station. This results in a DGPS configuration with an extreme small baseline (15m). This is a single differences code position solution, processed in Trimble Geomatics Office. Observation date is 3 August 2011.

4.1.2 Precision of the receivers velocity estimates

This subsection presents the results of the receivers' velocity estimates. As explained in the introduction, the Vincotech A1084 and the Garmin GPS GS(x) 76 are only capable of delivering the navigation data in a NMEA format. Unfortunately, due to the internal smoothing algorithms and the limited resolution of the NMEA format this resulted in no velocity information. The output during the static measurement campaign is only 0.0 m/s with an occasional jump. Therefore the time derivative of the position estimates is used.

In figure 4.8 the velocity estimates of the Vincotech are presented in a north, east and up system. While the standard deviation appears to be very small, in order of centimeters, the velocity peaks are at decimeter level with a maximum of 0.4 m/s. Furthermore the limited resolution of the NMEA position coordinates string is easily observed in the graph.

Figure 4.8: Error plot of the velocity estimates of the Vincotech A1084 with EGNOS corrections on 12 June 2011. The North component shows the largest standard deviation. Furthermore some outliers up to 0.4 m/s are observed.

The Vincotech shows a similar graph as the Garmin (see figure 4.9), for which the standard deviations are in the same order of magnitude. The same yields for the position jumps, in this case the largest position jump observed is 0.5 m/s.

With regard to the velocity estimates of the AsteRx1, the receiver generated Doppler and the carrier-phase-derived Doppler also known as displacements are investigated.

The receiver generated Doppler velocity plot of the AsteRx1 is presented in figure 4.10. Note that the same scale is used as in figure 4.8 and 4.9. The velocity estimates are in the order of mm/s, which lies within the expectations of the Doppler measurement performance. One large position jump is observed (around 22 hours UTC), at that time
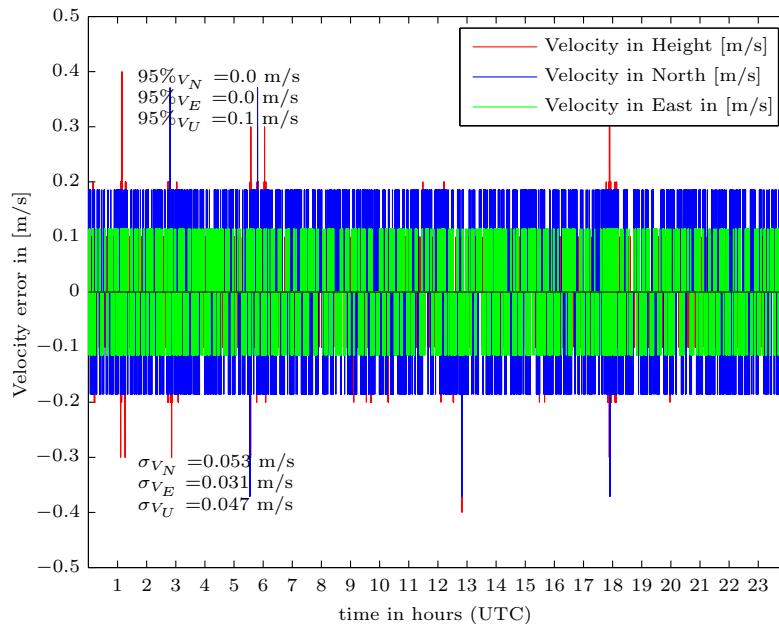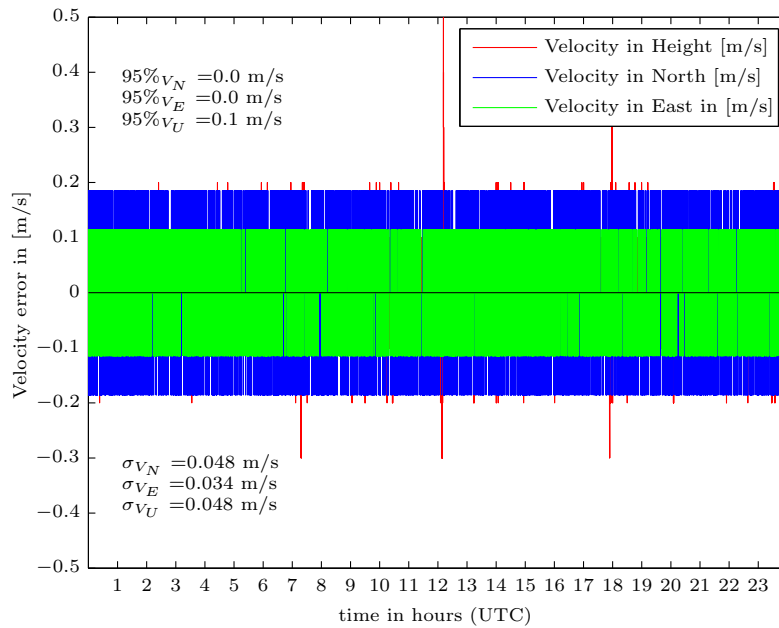
Figure 4.9: Error plot of the velocity estimates of the Garmin GPS 76 CS(X) with EGNOS corrections on 12 June 2011. The North component shows the largest standard deviation. While, the upward component has the largest outliers, up to 0.4 m/s.

the number of satellites in use was only four. Moreover the same jump is observed in figure 4.4. The measurement is repeated using the same set-up, but in this case with the patch antenna, the results are similar and therefore the position plot is left out of this report, the statistics can be found in table 4.2.

The velocity estimates based on the displacements measured with AsteRx1 in combination with the survey antenna are presented in figure 4.11. The measurements are significantly more biased, and less precise than the estimates of the receiver generated Doppler. Again, the same measurement is repeated with the patch antenna, the results can be found in table 4.2.

The results of the performance analysis of the velocity measurements for the three receivers are summarized in table 4.2. The 95% interval and the standard deviation for the north, east and up component are given for each receiver. The 95% interval for the Vincotech and Garmin are left out of this table. The extreme low values are caused by the limited resolution and internal smoothing algorithms. And, do not represent the actual performance of the receivers.
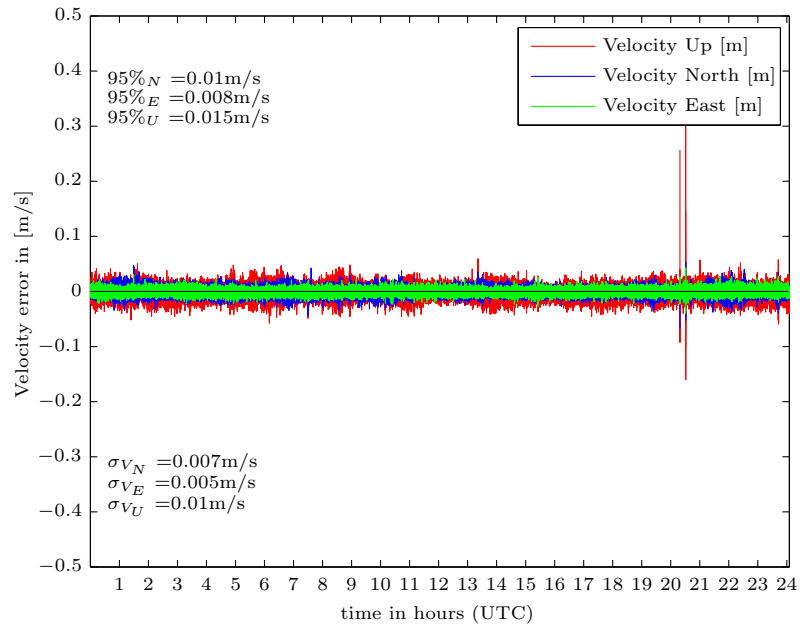
Figure 4.10: Error plot of the Doppler based velocity estimates of the Septentrio AsteRx1 with the PolaNt antenna in standalone mode on 27 April 2011.
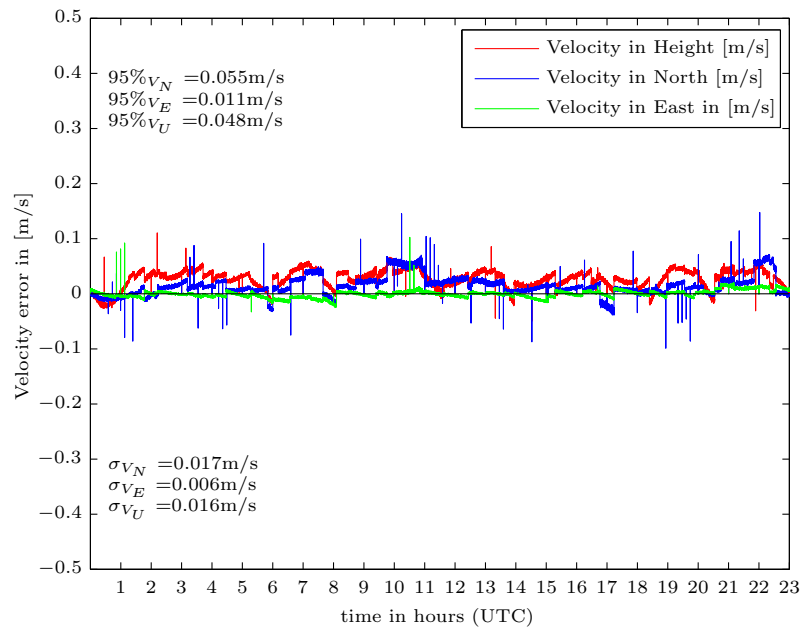
Figure 4.11: Error plot of the carrier-phase-derived Doppler velocity estimates (1 second interval displacements) of the Septentrio AsteRx1 with the PolaNt antenna in standalone mode on 9 May 2011.

Receiver	$95\%_{V_N}$	$95\%_{V_E}$	$95\%_{V_U}$	σ_{V_N}	σ_{V_E}	σ_{V_U}
Vincotech A1084	n/a	n/a	n/a	0.053	0.031	0.047
Garmin GPS 76 C(S)x	n/a	n/a	n/a	0.049	0.034	0.048
Septentrio AsteRx1 with AT575-275SW						
receiver generated Doppler	0.010	0.008	0.015	0.007	0.005	0.010
carrier phase derived Doppler	0.055	0.011	0.048	0.017	0.006	0.015
Septentrio AsteRx1 with AT575-70W						
receiver generated Doppler	0.011	0.008	0.017	0.007	0.005	0.011
carrier phase derived Doppler	0.044	0.006	0.049	0.014	0.005	0.014

Table 4.2: Summary statistics of velocity estimates from the receivers.

4.2 Dynamic measurement campaign: capture the buoy's dynamics

This section presents the results of the dynamic measurement campaign on buoy 18 as performed on 1-5 July 2011. The measurement campaign fulfilled the expectations and is considered to be a success.

After one week of floating on the open sea the measurement box and its equipment survived. The Trimble R7 receiver on the buoy logged for 100 hours before the battery was completely drained, while the base station logged for the complete time interval.

The RINEX files are processed with TGO and experimental MGP software, which show similar results: the accuracies for both solutions are in the order of millimetres (see the appendix D). The kinematic PPP solution of the GPS processing service from the NRC shows a centimetre accuracy [NRC, 2003]).

The position and height of the buoy is plotted in a local north, east and up system in figure 4.12. The path of the buoy is similar for the eight complete tidal cycles and appears to be influenced by one dominant current direction. The graph also indicates the location of the buoy during high and low water, which are obtained by an analysis of the height component. This is done by filtering out the high frequent components, succeeded by numerical algorithm that finds maximum and minimal values using specified thresholds.

4.3 Simplifying the buoy's motion: from a three-dimensional position to a one-dimensional extension

This section presents the results of the dimensional simplification using PCA as is described in the methodology chapter. The input are the local east and north coordinates from the previous section. The height component is neglected, which is justified in section 3.4.

The PCA transformation results in two components, the first (main) and second principle component. The main component contains the extension in the direction of the main principle axis. This axis is assumed to be lined up with the dominant current direction. The second component can be seen as the residual movement of the buoy perpendicular to the dominant current direction.

As explained in section 3.4.2 the extension is now related to the empirical mean. This is incorrect: a shift to the defined centre point is necessary. The correct centre point is determined using equation 3.5. Figure 4.13 shows the centre point with regard to the empirical mean for each tidal cycle. Furthermore the mean centre point $\bar{c}$ is indicated with the black line and the standard deviation (σ_c) based on these 8 observation is indicated with the red lines.

The final results of the simplifications are shown in figure 4.14. The top graph shows the extensions with regard to centre point. It is important to note that the maximum and minimum extension are approximately equal. The residuals are plotted in the bottom graph and are unbiased ($\mu \approx 0.00m$). Moreover, they show a small standard deviation σ of only 2.54 m.
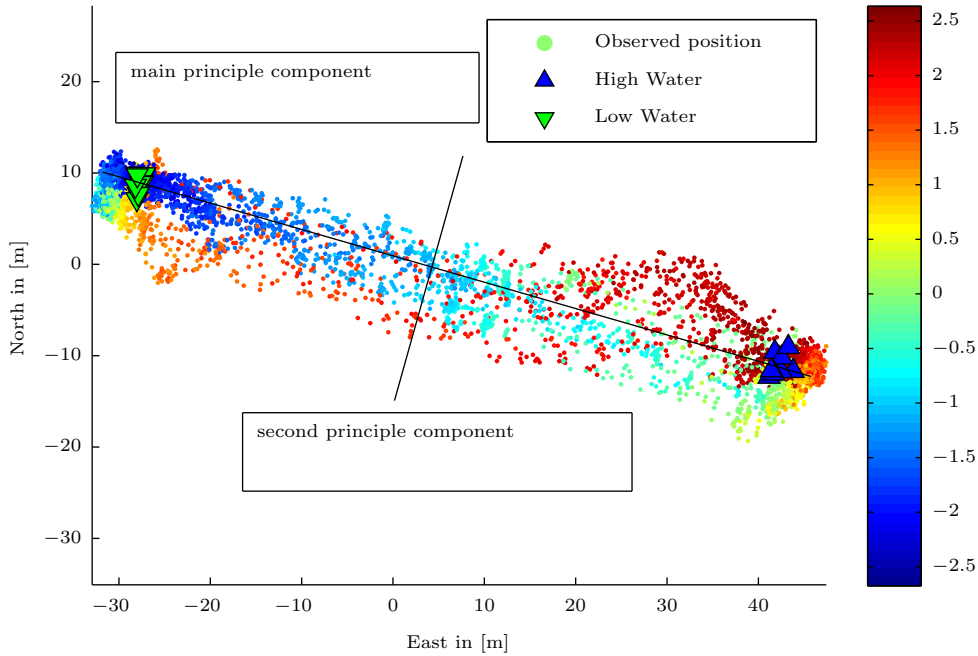
Figure 4.12: Three-dimensional position estimates at 60 seconds interval of the Trimble R7 (logged at 1 Hz) on buoy 18 using a fixed carrier phase baseline solution processed in MGP-software. The north, east and up coordinates are in a local grid relative to the mean position of buoy 18. The relative height is represented in the colour of the markers, the triangles show the position related to high and low water. The axis of the principle components are visualized schematically in this graph. Observation date is 1-5 July 2011.

The maximal observed extension of approximately 40 meters is almost in correspondence with the values provided by RWS with regard to chain length, charted depth and the draft of the buoy, which resulted in a maximum theoretical extension of 37.0 (high water) and 38.5 (low water).

The difference between the theoretical and observed maximal extension can be explained by the momentum created by chain force and the flow force, which results in an attitude inclination of the buoy in the direction of the dominant current, which directly affects the position of the antenna (mounted on the highest point). The antenna was mounted almost 4 meters above the water surface.

In figure 4.15 the extension, smoothed velocity and acceleration of the buoy during the observed tidal cycles are plotted as a function of time. The figure shows also the smoothed mean average for the position, velocity and acceleration (red line). The maximum extension, which is also indicated in the previous figure, is approximately 40 m. For the velocity the individual tracks are smoothed with a moving average filter (blue lines) in order to
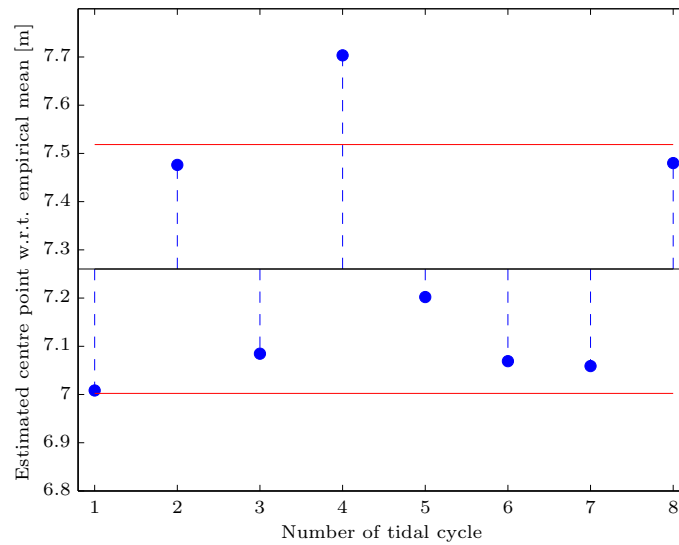
Figure 4.13: This graph shows the estimated centre point for each tidal cycle. The black line indicates the average centre point $\bar{c}$ and the red lines indicate the standard deviation σ_c. Observation date is 1 till 5 July 2011.

reveal a trend in the velocity. The observed velocity is much noisier, and shows velocities up to 3 m/s. This is due to the three-dimensional oscillatory motion of the buoy. The maximum smoothed velocity is in the order of 1-3 cm/s, and is observed during the transition of the buoy. In the acceleration a small trend is observed, the acceleration tends to be slightly larger during transitions.
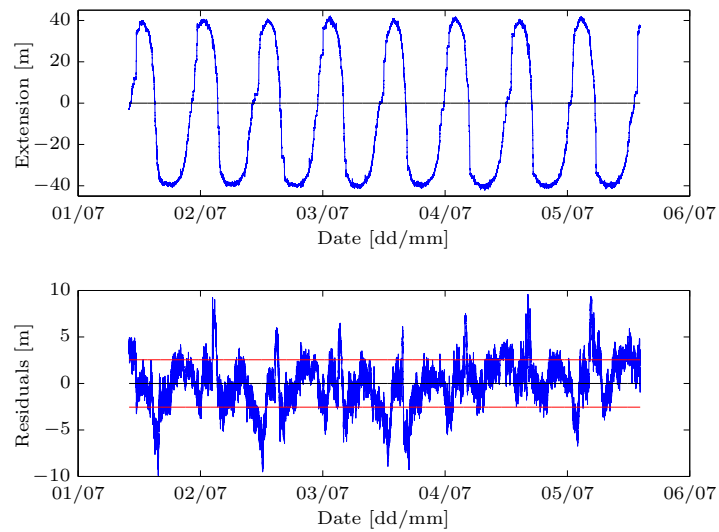
Figure 4.14: Top: this graph shows the extension of buoy 18 in the dominant current direction (main principle component) related to the centre point. The maximal extension during ebb and flood are approximately the same. Bottom: this graph shows the residuals (second principle component). The mean value $\mu \approx 0.00$ m and the standard deviation σ equals 2.54 m (red line). Observation date is 1 till 5 July 2011.
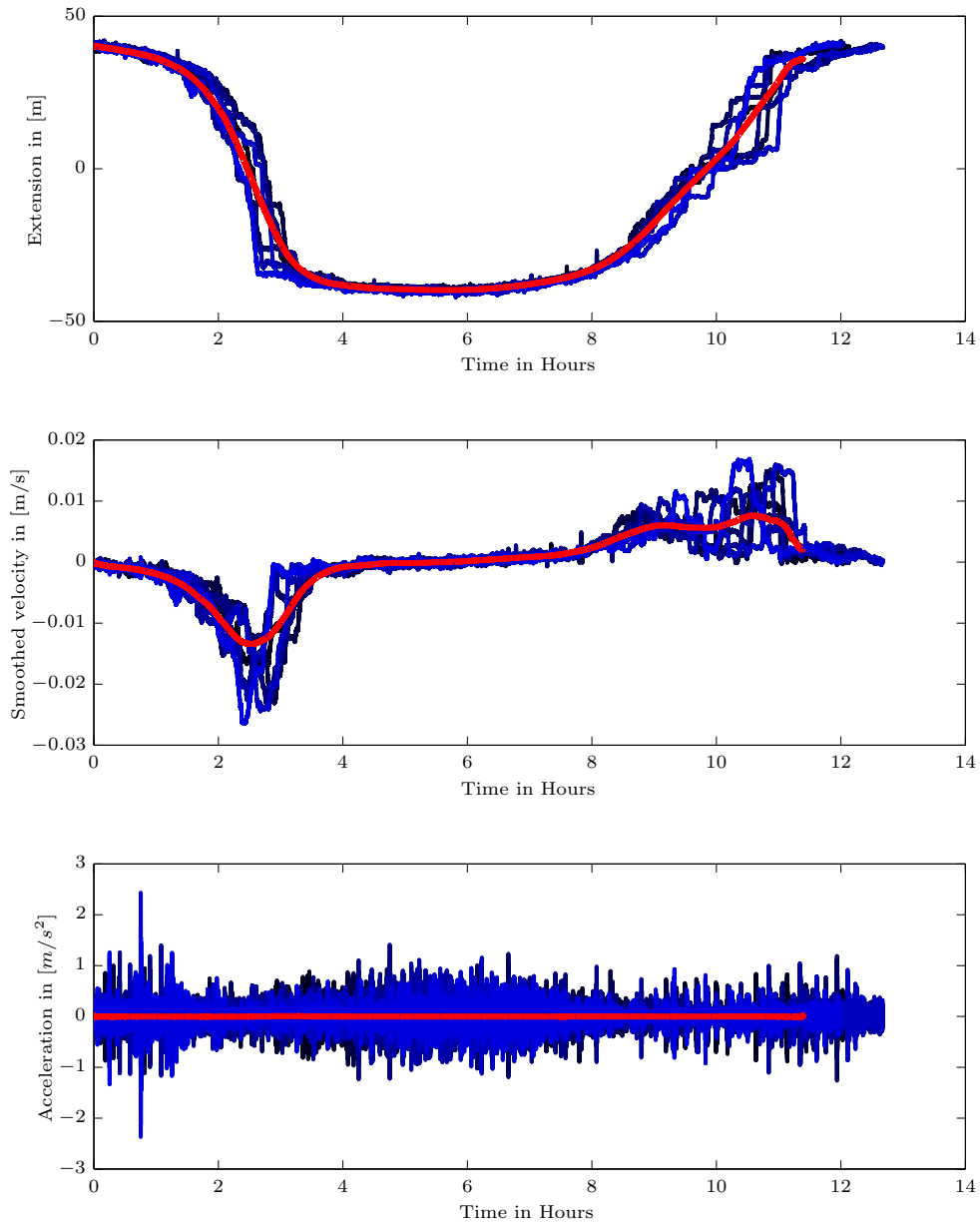
Figure 4.15: The three graphs show the position, smoothed velocity and acceleration of the
buoy during six complete tidal cycles. The blue lines, varying from light to dark
blue, indicate the succeeding tidal cycles. The redline is obtained by taking
the smoothed average of all observed tracks. Position estimates are obtained
with the Trimble R7 using a fixed baseline solution at 1Hz.

4.4 Mathematical description of a buoy's dynamics due to a tidal current

This section presents the results of modelling the buoy's dynamics as a mass-spring system. The model fit is judged in terms of its residuals. The system, the different spring force models and the calibration process are described in section 3.5.

In figure 4.16 the modelled and observed extensions of the buoy are plotted against time. Six different chain force models are used. These models are calibrated on the average observed smoothed extensions during a complete tidal cycle (see section 3.5.3). The graph also shows the *observed* current velocity at buoy 16 on 6 July 2011, which functions as the driving force of this system F_{flow}.

The first order model behaves very well during the maximum and minimal extension. However during the transition the modelled force tends to be stronger than is observed. A small improvement is found using the second order model. The third order model approximates the observed extension even better, a slight overshoot is noted around 20 meters extension during the falling period. However during the rising period the observed and modelled positions are almost equal.

The fourth order model also approximates the observed extension in a good manner and produces similar results as the third order model. The eighth order model is used to show that the solution does not lie with higher order models. The modelled force during minor extensions appears to be too weak and results in a larger extension than is observed. The exponential model is the most extreme, and does not resemble the observed behavior.

The residuals are created by subtracting the modelled extension with the observed averaged and smoothed extension. The results provide a clear result of the performance of the different mass-spring models (see figure 4.17). The previous paragraphs indicate that the third and fourth order model resemble the modelled extension most appropriately, this is confirmed with the low residual values shown in table 4.3.

Moreover the residual values for the first and second order model are also fairly small. Unlike the eighth order and exponential model, which show residuals that are significantly larger, indicating that these spring force models are less suitable.

1th order	2nd order	3rd order	4th order	8th order	exponential
4,07	3,76	2,89	3,82	5,43	5,48

Table 4.3: Residuals in meters of the observed extension vs the extension of the mass-spring model.

In addition to the extension also the velocity of the buoy is modelled, and is plotted in figure 4.18 as function of time. It appears that the speed of the buoy is extremely low during the transition. Maximum observed velocities are in the order of 1 to 2 cm/s. The first, second and third order models show the similar velocity profile as is observed. The fourth, eighth and exponential order models show velocities that are 2 to 3 times larger than is observed.

Moreover it is noticed that the velocity of the buoy is higher during the rising period than the falling period. This is caused by the more rapid changing current velocity during the
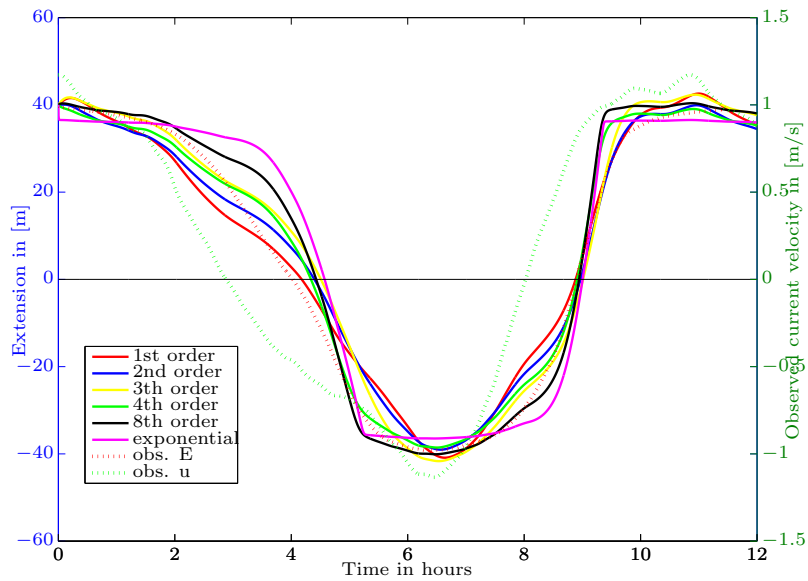
Figure 4.16: The extension E of the buoy is modelled as a dampened mass-spring system with six different spring force models. Each model is calibrated on the smoothed and averaged extension of buoy 18 as observed during the measurement campaign on 1-5 July by adjusting the spring constant k and viscous damping coefficient c. As a driving force of the system the observed current u at buoy 16 on 6-July is used.

falling rising period.

Summarizing, this section showed the results of modelling the dynamics of the buoy with a dampened mass-spring system. Furthermore, the quality of the model fits is shown. The results of this section are used in the development of a state-space model for a Kalman filter in the next section and are used in the development of the method for the estimation of slack tide.
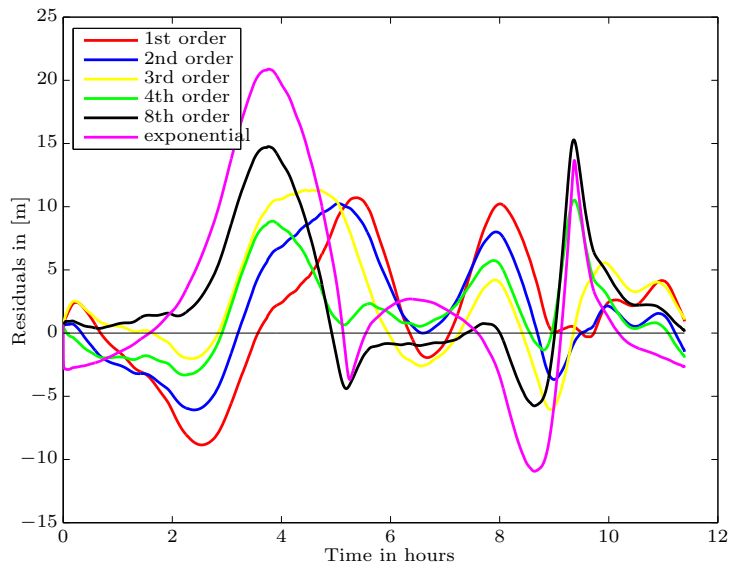
Figure 4.17: This graph shows the residuals between the observed extension and the modelled extension. The residuals of the 3rd order spring force model are the smallest, the largest residuals are found using the exponential spring force model.
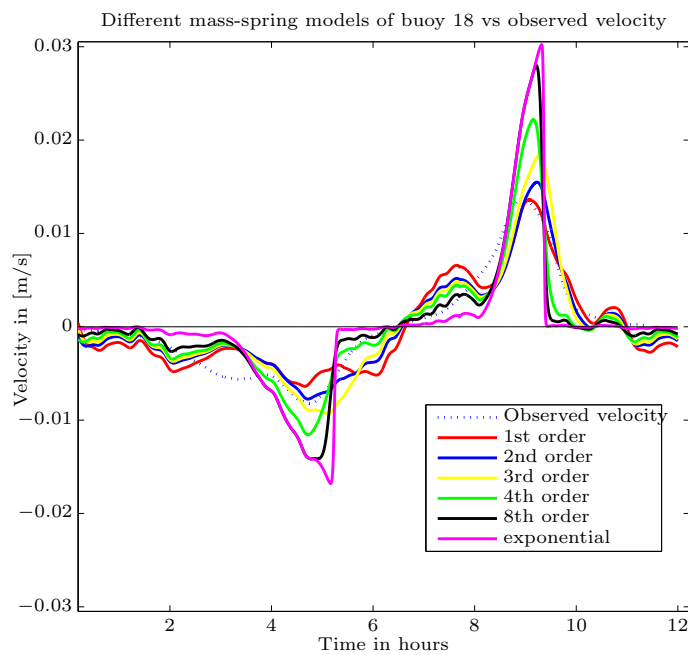
Figure 4.18: Different mass-spring-damper models of buoy 18 vs observed velocity. The dynamics of the buoy are modelled as a dampened mass-spring system. Six different models for the spring force are considered. Each model is calibrated on the smoothed average extension of buoy 18 as observed during the measurement campaign on 1-5 July by adjusting the spring constant k and viscous damping coefficient c. As a driving force of the system the observed current at buoy 16 on 6-July 2011 is used.

4.5   Kalman filter for the extension of a buoy

In section 3.5 the dynamics of the buoy are modelled as a dampened mass-spring system. Based on the residuals between the observed and modelled extensions this model appeared to be a good approximation. The mathematical model is used here, as a side-step of this research, to develop a Kalman filter for the observed extensions. The purpose is to exploit the knowledge about the buoy's dynamics and measurement history in addition to just a current measurement. In subsection 4.5.1 the mathematical model is rewritten in a linear time-invariant state equation, which is applied in a Kalman filtering algorithm in subsection 4.5.2.

4.5.1   Linear time-invariant state equation of an overdamped mass-spring system

To develop a Kalman filter for this system, some simplifications with regard to the mathematical dampened mass-spring model are required. Although a third order chain force model shows the best fit, it is assumed that a linear chain model is an appropriate representation of the unknown chain force. The driving force of the system F_{flow}, is the force induced by the tidal current. It is assumed that this force can be modelled a priori with an average current pattern of the estuary, which is available for most estuaries as described in [Haas, 2007]. This section continues with the derivation of a linear time-invariant state equation for a overdampened mass-spring system, which is described by [Teunissen, 2001].

Rewriting equation 3.6 with a linear chain model:

$$\ddot{x} + \frac{c}{m}\dot{x} + \frac{k}{m}x = F_{flow}(t)/m \tag{4.1}$$

To rewrite this scalar second-order differential equation into a first-order vector form, two variables are defined:

$$\begin{aligned} x_1 &= x \\ x_2 &= \dot{x} \end{aligned} \tag{4.2}$$

Substitution of (4.2) into (4.1) yields:

$$\dot{x}_2 + \frac{c}{m}x_2 + \frac{k}{m}x_1 = F_{flow}(t)/m \tag{4.3}$$

Equation (4.3) can be rearranged to a first-order vector form:

$$\begin{bmatrix} \dot{x}_1 \\ \dot{x}_2 \end{bmatrix} = \begin{bmatrix} 0 & 1 \\ -k/m & -c/m \end{bmatrix} \begin{bmatrix} x_1 \\ x_2 \end{bmatrix} + \begin{bmatrix} 0 \\ F_{flow}(t)/m \end{bmatrix} \tag{4.4}$$

To summarize: with (4.2) the scalar second-order differential equation (4.1) is transformed into a first-order vector form (4.4). The vector $[x_1, x_2]^T$ is the state vector of this system.

From now on F_{flow}/m will be denoted as f the specific force, which is a more common and shorter notation.

Based on the state equation (4.4) the system matrix of a linear mass-spring system equals:

$$F = \begin{bmatrix} 0 & 1 \\ -\omega^2 & -2\gamma \end{bmatrix} \quad \text{with} \quad \omega^2 = \frac{k}{m} \quad , \quad \gamma = \frac{c}{2m} \tag{4.5}$$

The characteristic polynomial of F equals:

$$det(F - \lambda I) = \lambda^2 + 2\gamma\lambda + \omega^2 = 0 \tag{4.6}$$

Which results in two eigenvalues:

$$\lambda_{1,2} = -\gamma \pm \sqrt{\gamma^2 - \omega^2} \tag{4.7}$$

From the calibration of the dampened mass-spring system to resemble the dynamics of the buoy, it followed that $\gamma > \omega^2$. Furthermore, since γ is positive, both eigenvalues are negative. The eigenvectors are obtained by solving for $i = 1, 2$:

$$(F - \lambda_i I_2)t_i = 0 \tag{4.8}$$

The eigenvectors can be ordered in columns, now the matrix T is defined as:

$$T = \begin{bmatrix} 1 & 1 \\ \lambda_1 & \lambda_2 \end{bmatrix} \tag{4.9}$$

The inverse of T equals:

$$T^{-1} = (\lambda_2 - \lambda_1)^{-1} \begin{bmatrix} \lambda_2 & -1 \\ -\lambda_1 & 1 \end{bmatrix} \tag{4.10}$$

When the exponential of a matrix must be found, which is the case for the solution of the linear time-invariant system, a number of numerical calculation methods are available. The Jordan canonical method is used. With (4.9), (4.10) and the application of the Jordan canonical form method the following yields:

$$e^{Ft} = \begin{bmatrix} 1 & 1 \\ \lambda_1 & \lambda_2 \end{bmatrix} \begin{bmatrix} e^{\lambda_1 t} & 0 \\ 0 & e^{\lambda_2 t} \end{bmatrix} \begin{bmatrix} \lambda_2 & -1 \\ -\lambda_1 & 1 \end{bmatrix} (\lambda_2 - \lambda_1)^{-1} \tag{4.11}$$

The solution of the linear, time-invariant state equation (4.4) is given by:

$$\begin{bmatrix} x_1(t) \\ x_2(t) \end{bmatrix} = \begin{bmatrix} a_1 e^{\lambda_1(t-t_0)} + a_2 e^{\lambda_2(t-t_0)} \\ a_1\lambda_1 e^{\lambda_1(t-t_0)} + a_2\lambda_2 e^{\lambda_2(t-t_0)} \end{bmatrix} + \int_{t_0}^t \begin{bmatrix} e^{\lambda_1(t-\tau)} - e^{\lambda_2(t-\tau)} \\ \lambda_1 e^{\lambda_1(t-\tau)} - \lambda_2 e^{\lambda_2(t-\tau)} \end{bmatrix} (\lambda_2 - \lambda_1)^{-1} f(\tau) d\tau \tag{4.12}$$

where

$$\begin{aligned} a_1 &= (\lambda_2 - \lambda_1)^{-1}(\lambda_2 x_1(t_0) - x_2(t_0)) \\ a_2 &= (\lambda_2 - \lambda_1)^{-1}(-\lambda_1 x_1(t_0) - x_2(t_0)) \end{aligned} \tag{4.13}$$

Summarizing, in this subsection the linear time-invariant state equation of an overdamped mass-spring system is developed. In the next section this knowledge about the dynamics of the buoy are used in a Kalman filter.

4.5.2 Kalman filter equations

In the previous section a linear time-invariant state equation is developed for a mass-spring system. Now this equation is used in a Kalman Filter algorithm as described by [Teunissen, 2001]. The Kalman filter is a recursive algorithm and the implementation is represented graphically in 4.19.
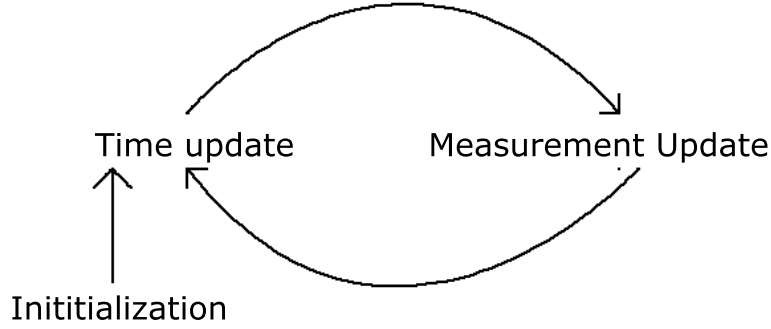
Figure 4.19: Recursive prediction and filtering. The time update predicts the current state ahead. The measurement update corrects the projected estimate by an observation.

Initialization. Initial values for the extension and extension rate of change of the buoy are necessary. These are described in $\hat{\underline{x}}_{0|0}$. If $k = 0$ the buoy has a maximum extension and the extension rate of change equals zero. The correctness of this assumption influences the convergence time. The uncertainty with regard to this initial value $\hat{\underline{x}}_{0|0}$ is described in the error covariance matrix $Q_{\hat{x}_{0|0}}$.

Time Update. With the time update equations the posteriori estimates are used in combination with the dynamical model to predict new a priori estimates of the state vector $\hat{\underline{x}}_{k|k-1}$ (4.14) and the error covariance $Q_{\hat{x}_{k|k-1}}$ (4.15). The continuous time-update equations read therefore [Teunissen, 2001]:

$$\hat{\underline{x}}_{t|k-1} = \Phi_{t,k-1}\hat{\underline{x}}_{k-1|k-1} + \int_{t_{k-1}}^{t} \Phi_{t,\tau}G_\tau \underline{z}_\tau d\tau \tag{4.14}$$

$$Q_{\hat{\underline{x}}_{t|k-1}} = \Phi_{t,k-1}Q_{\hat{\underline{x}}_{k-1|k-1}}\Phi_{t,k-1}^* + \int_{t_{k-1}}^{t} \Phi_{t,\tau}G_\tau Q_{zz}G_\tau^*\Phi_{t,\tau}^* d\tau \text{ for } t \in (t_{k-1}, t_k) \tag{4.15}$$

For this particular dynamic system $\Phi(t, t_0)$ follows directly from (4.12) and equals:

$$\Phi(t, t_0) = (\lambda_2 - \lambda_1)^{-1} \begin{bmatrix} \lambda_2 e^{\lambda_1(t-t_0)} - \lambda_1 e^{\lambda_2(t-t_0)} & -e^{\lambda_1(t-t_0)} - e^{\lambda_2(t-t_0)} \\ \lambda_1\lambda_2(e^{\lambda_1(t-t_0)} - e^{\lambda_2(t-t_0)}) & -\lambda_1 e^{\lambda_1(t-t_0)} - \lambda_2 e^{\lambda_2(t-t_0)} \end{bmatrix} \tag{4.16}$$

$\Phi(t, \tau)$ is obtained by replacing t_0 with τ in $\Phi(t, t_0)$. The matrix G is straightforward and equals:

$$G = \begin{bmatrix} 0 \\ 1 \end{bmatrix}, \tag{4.17}$$

$\underline{z}_\tau$ is described by the acceleration induced on the buoy by the the tidal current. Q_{xx} represents the model noise and is described by the following auto-covariance function.

$$Q_{xx}(t_1, t_2) = \Phi(t_1, t_0)Q_{xx}(t_0, t_0)\Phi(t_2, t_0)^* + \int_{t_0}^{t_1} \int_{t_0}^{t_2} \Phi(t_1, \tau_2)G(\tau_1)Q_{zz}(\tau_1, \tau_2)G(\tau_2)^*\Phi(t_2, \tau_2)^* d\tau_1 d\tau_2 \tag{4.18}$$

This function, which is evaluated for the calibrated mass-spring-damper system of buoy 18 for the time notations: $t_0 = 0$ and $t_1 = t_2 = 1$ in the appendix E equals:

$$Q_{xx}(t_1, t_2) = \begin{bmatrix} -20.0116 & -1.0006 \\ -0.0110 & -0.0006 \end{bmatrix} Q_{xx}(t_0, t_0) \begin{bmatrix} -20.0116 & -0.0110 \\ -1.000550 & -0.000550 \end{bmatrix} \\ + Q_{zz} \begin{bmatrix} 0.9040 & 0.9508 \\ 0.9508 & 1.0011 \end{bmatrix} \tag{4.19}$$

Measurement Update. In the measurement update phase, the current a priori prediction is combined with the current measurement to refine the state estimate. The measurement update equations read therefore:

$$\hat{\underline{x}}_{k|k} = \hat{\underline{x}}_{k|k-1} + Q_{\hat{x}_{k|k-1}} A_k^* Q_{y_k}^{-1}(\underline{y} - A_k\hat{\underline{x}}_{k|k-1}) \tag{4.20}$$

$$Q_{\hat{x}_{k|k}} = (Q_{\hat{x}_{k|k-1}}^{-1} + A_k^* Q_{y_k}^{-1} A_k)^{-1} \tag{4.21}$$

Where the A-matrix equals:

$$A = \begin{bmatrix} 1 & 0 \end{bmatrix}. \tag{4.22}$$

The measurement noise Q_{y_k} depends on the measurement accuracy.

4.5.3   Kalman filtering of the observed extension

In the previous sections the Kalman filter for the extension of a buoy due to a a priori defined tidal current force is described. To show the improvement in terms of accuracy, a small selection of the observed extensions is filtered. However, the results are considered as an optional improvement and part of the recommendations.

Gaussian noise with a zero mean and a standard deviation of 1 meter is added to the extensions. This is done to resemble the situation of a medium cost GPS receiver in SBAS mode, for example the Septentrio AsteRx1 with the patch antenna. The measurement noise Q_{y_k} is set to $(1m)^2$. The model noise Q_{zz} is based on an analysis of the observed acceleration of the buoy and is set to $(0.3m/s^2)^2$ which is equal to the variance of the observed acceleration.

The results are presented in figure 4.20, a clear improvement of the filtered extensions is observed. The standard deviation σ of the filtered solutions is 0.3 m a clear improvement in comparison with standard deviation of the input which is 0.9 m. The standard deviations are related to the empirical mean, after the trend of the data is removed with a first order polyline.

Summarizing, this subsection showed the performance of filtering the extensions with a Kalman filter using a state-space representation of a dampened mass-spring system with a linear spring force model.
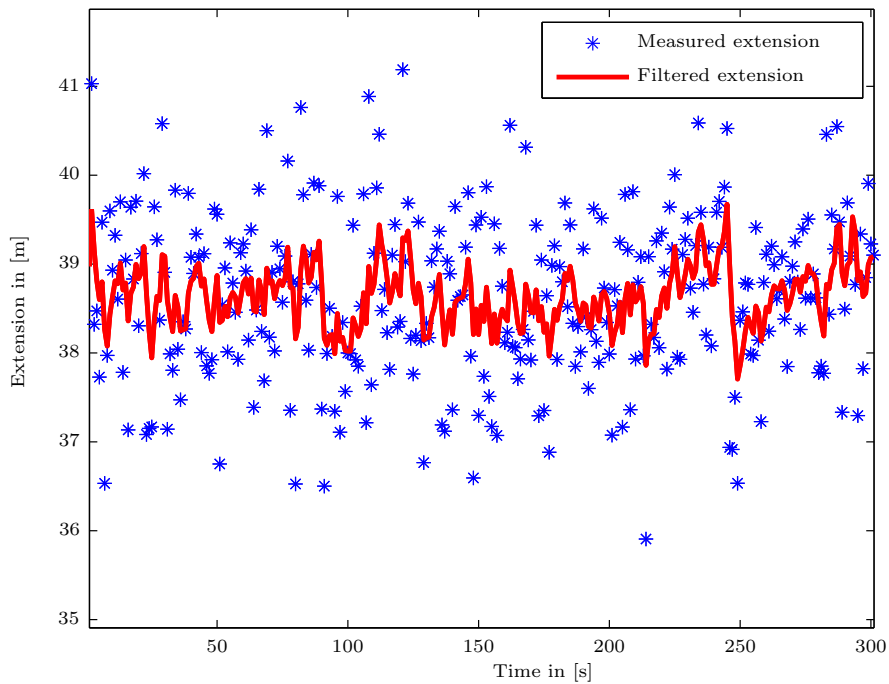
Figure 4.20: This graph shows the results of the Kalman filter algorithm applied to the observed extensions of buoy 18 around 11 hours UTC on 1-July 2011. Normal distributed noise is added to the extensions to resemble the measurement precision of the Septentrio AsteRx1 with the patch antenna in SBAS mode.

4.6 Estimation of slack tide: composite hypothesis testing

The concept of hypothesis testing is discussed in section 3.6. In this section the variables for the hypothesis testing are defined. First the extension related to the moment of slack

tide E_{st} is determined. The next subsection is devoted to determine the variance σ^2 that defines partly the hypothesis. The variance σ^2 consists of three stochastic variables, each is discussed separately. In the last part, the influence of the significance level α and measurement precision is analyzed.

4.6.1 Determination of moment of slack tide

Section 4.4 is devoted to find a relationship between the extension of the buoy and the tidal current. The extension of the buoy during the moment of slack tide is represented schematically in figure 4.21. Now the following holds:

$$E_{st}^{hw/lw} = L_{chain} + Dr_{buoy} - Z - T \tag{4.23}$$

With:

- $E_{st}^{hw/lw}$ is the extension at the moment of slack tide related to high or low water slack;

- L_{chain} is the length of the chain;

- Dr_{buoy} is the draft of the buoy;

- Z is the depth with respect to MSL and;

- T is the elevation during HWS or LWS.

This implies that for every buoy the extension that is related to the moment of slack tide is different. Furthermore results equation (4.23) in two different values of E_{st}, one for the extension at the moment of slack tide for high water and one for low water.

For buoy 18 the length of the chain L_{chain} is set to 40m according to [Rijkswaterstaat, 2011a]. The water depth related to NAP Z is found in an internal hydrographic chart of RWS and is 16m. The draft of the buoy Dr_{buoy} is derived by a simple displacement calculation and is set to 1m. The tidal elevation at the expected moment of slack tide, which is approximately 60 minutes after high or low water, is +2.3m and -1.8m. Now the extension for the moment of high water slack is:

$$E_{st}^{hw} = L_{chain} + Dr_{buoy} - Z - T = 40 + 1 - 16 - 2.3 = 22.7 \tag{4.24}$$

And for low water slack this is equal to:

$$E_{st}^{lw} = L_{chain} + Dr_{buoy} - Z - T = 40 + 1 - 16 + 1.8 = 26.8 \tag{4.25}$$
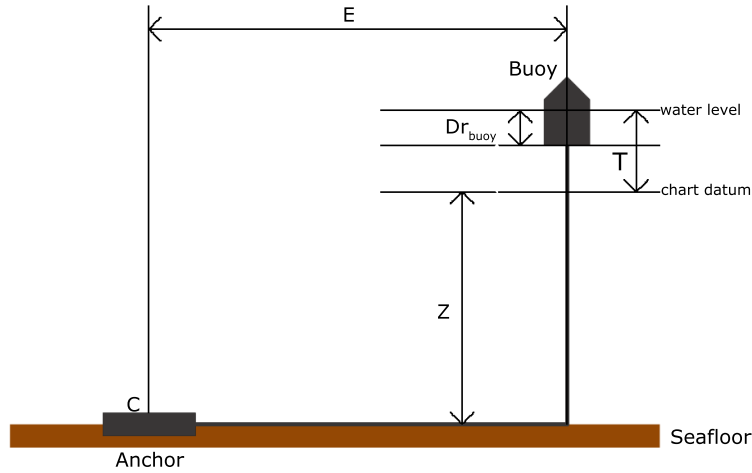
Figure 4.21: Schematic representation of the geometry during the moment of slack tide. Where E denotes the extension, Z is depth with regard to the chart datum, T is the tidal elevation and Dr_{buoy} is the draft of the buoy. The chain is on the floor, right up to underneath the buoy.

4.6.2 Determination of the variance for the hypothesis

The variance σ^2 that partly describes the hypothesis consists of three components: the variance of the GPS position estimates σ_{gps}^2, the noise in the buoy movement that is not related to the current σ_{bd}^2 and the uncertainty of the extension that is related to the moment of slack tide $\sigma_{E_{st}}^2$. Under the assumption that these are uncorrelated the following holds:

$$\sigma^2 = \sigma_{gps}^2 + \sigma_{bd}^2 + \sigma_{E_{st}}^2 \tag{4.26}$$

The determination of σ_{gps}^2 is straightforward and is based on the results of the static measurement campaign. Recall table 4.1 which provides an overview of the standard deviation of the analyzed receivers in combination with different antennas and operating modes.

However, σ_{bd}^2 is more difficult to determine. The dynamic measurement campaign on buoy 18 is performed with the Trimble R7 in relative positioning mode, yielding mm position accuracy. In this manner it is possible to determine σ_{bd}^2, while neglecting σ_{gps}. For any other GPS measurement system, σ_{gps}^2 will be significantly larger and cannot be neglected.

Figure 4.22 shows the extension of the buoy during a period of zero nett movement. This implies that F_{flow}, during this interval is (almost) constant and counteracted by F_{chain} The observed motion results from forces that are acting on the buoy due to wind and wind induced waves. This 'noise' is modelled with a standard normal distribution, which can be seen in the bottom graph of figure 4.22. This results in an empirical variance for the buoy dynamics σ_{bd}^2 of 0.123 m^2. Moreover, σ_{bd}^2 is much smaller than the variance in the residuals (see figure 4.14), since we are now considering the situation of dampened random motion in the direction of the dominant current direction and assuming that the residuals contain no information with regard to the moment of slack tide.
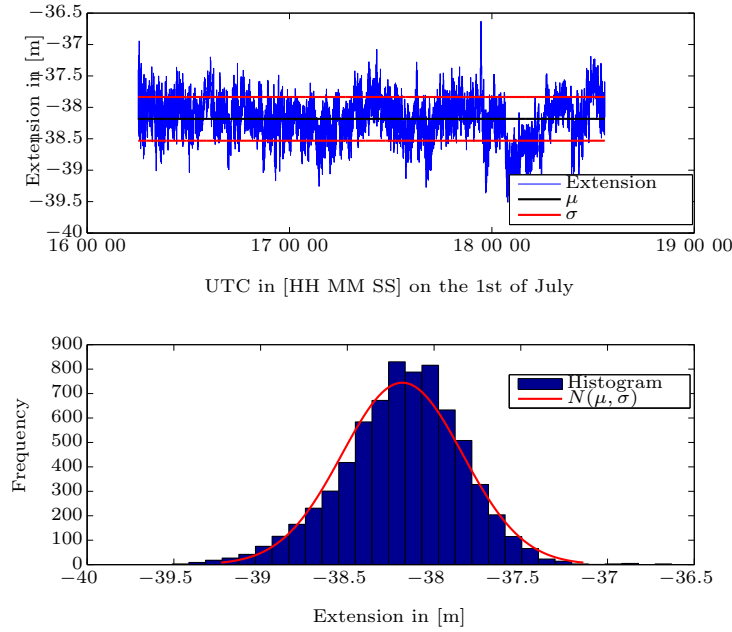
Figure 4.22: Top: This graph shows the dynamics of buoy 18 on the 1st of July 2011 during a period of zero nett movement. The position estimates are projected on the dominant current direction and plotted against time. Furthermore it indicates the standard deviation σ and the mean μ. Bottom: This graph shows the histogram and the least squares best fit of the normal distribution (with: $\mu = -38.2$ m and $\sigma = 0.35$ m) from the dataset presented in the top graph.

The variance with regard to the extension that is related to the moment of slack tide E_{st} is difficult to determine. It relies on the variance of the the chain length, the draft of the buoy, the charted depth and the tidal elevation.

Unfortunately there is no information with regard to the precision of the length of the chain. Therefore it is assumed to be 0.2 m, which is approximately the length of one shackle. The draft of the buoy is calculated using the shape and weight of the buoy, both are precisely known resulting in $\sigma^2_{Dr_{buoy}} = 0.1$ m.

The tidal elevation however is determined by field measurements during the dynamic measurement campaign. The average tidal elevation for a prior defined moment of slack tide is known with centimeter precision, resulting in $\sigma^2_T = 0.1m$.

The precision of the charted water depth at the location of the buoy is influenced by many parameters. The most important are the accuracy of the anchor position in combination with the morphology, the dynamics of the morphology in combination with the acquisition time and the measurement technique. Therefore, the variance of the of the charted depth σ^2_Z is assumed at 0.3 m.

Assuming uncorrelated variables and the application of the propagation of variance the

following holds:

$$\sigma^2_{E_{st}} = \sigma^2_{L_{chain}} + \sigma^2_{Dr_{buoy}} + \sigma^2_Z + \sigma^2_T \tag{4.27}$$

Substituting in the terms in equation 4.27 results in $\sigma^2_{E_{st}} \approx 0.7 \ m^2$.

Now the values for $\sigma^2_{E_{st}}$, σ^2_{bd} and σ^2_{gps} are defined, they are combined in a total variance σ^2 necessary for the hypothesis testing with equation 4.26. Resulting in $\sigma^2 = \sigma^2_{E_{st}} + \sigma^2_{bd} + \sigma^2_{gps} = 0.83 \ m^2$. Note that in this initial case, using the high precise position solution σ^2_{gps} is neglected and set to zero.

4.6.3 Choice of the significance level α, GPS receiver, antenna and operating mode

The choice of significance level α and the GPS receiver in combination with a particular GPS antenna and operating mode - which determines σ^2_{gps} - influences the detection delay.

The significance level directly influences the moment of slack tide detection and the chance on a false early detection. If α is set too small, the detection delay increases. If we set α to high, the chance on a false detection increases.

In figure 4.23 the detection delay is plotted as function of α for all GPS receivers in combination with their antennas and operating modes that are evaluated during the static measurement campaign. This is done by hypothesis testing on the dataset with different critical values k_α, which is a function of α and σ^2. The zero detection delay, to which this graph is related, is obtained with the Trimble R7 $\sigma_{gps} \approx 0$ and a significance level of $\alpha = 0.05$.

The graph clearly shows the relation between the significance level and the detection delay. Furthermore, measurement set-ups with a larger variance are more sensitive to the choice of the significance level. The results of the Vincotech shows this in the most extreme form that is observed, with a maximum additional detection delay of 7 minutes with a significance level α of 0.01. Similar but less extreme results are seen for all the configurations of the Garmin GPS 76 C(S)x.

The best result is obtained using the Septentrio AsteRx1 with a survey antenna in SBAS mode, this is however somewhat surprising if we consider the results of the similar equipment in a SD solution, yielding a very small bias. This can be explained by the fact that for this application only the variance of the horizontal position estimate with regard to the empirical mean is important, which is described by variance of the north and east component $\sigma^2_{NE} = \sigma^2_N + \sigma^2_E$.

Around a significance level α of 0.05 the detection delay increases almost exponentially (due to exponential nature of a normal distribution), this point can therefore be seen as an optimum significance level minimizing the detection delay and the chance on a false alarm.

Figure 4.24 shows the probability of detection γ as a function of the buoy dynamics in time. This graph is based on a significance level of $\alpha = 0.05$ and the smoothed average buoy extension is used as input. The moment $T = 0$ is the very moment that the extension E is equal to the extension related to the moment of slack tide E_{st}. The probability of detection γ increases from approximately zero to one in approximately 400 seconds.
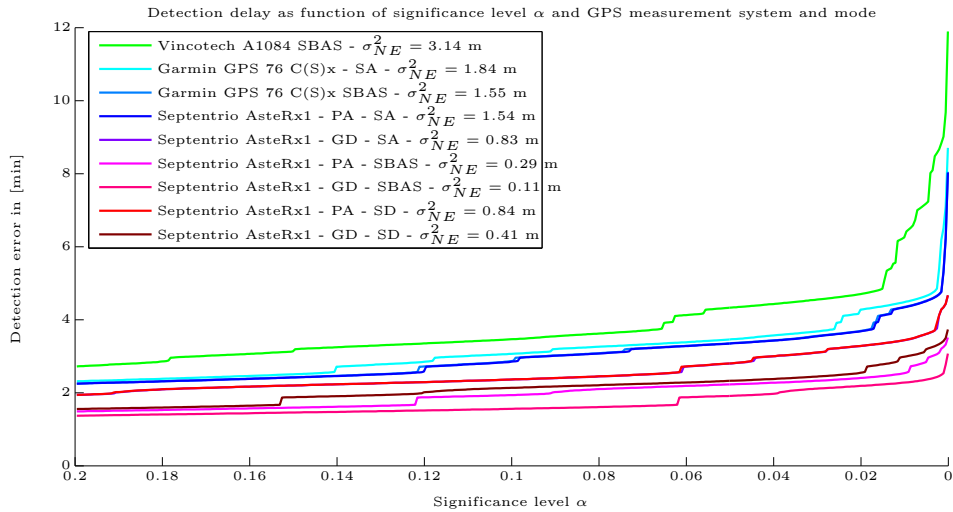
Figure 4.23: This graph shows the detection delay for different significance levels, GPS modes, GPS receivers and GPS antennas based on single epoch extensions. The results of the static measurement campaign, where an analysis is made on the performance of different GPS receivers, antennas and operating modes, is used to calculate the detection delay. The zero delay is set equal to estimated mean high water phase lag using the Trimble R7 (yielding millimetre accuracy). Where PA stands for patch antenna, SU for survey antenna, SA for stand alone and SD for single difference (a relative positioning technique). A low value for α indicates an higher significance and a smaller chance on a false alarm. However, a smaller value for α results in a larger phase lag.

4.7   The estimated phase lag at buoy 18

This section present the results of the estimated phase lag. The previous section is devoted to detect the moment of slack tide. Once the moment of slack tide is known, the determination of the phase lag is straight forward and is described in section 3.7.

Figure 4.25 shows the estimated phase lags for high and low water at water surface at the location of buoy 18 on 1-5 July 2011. These results are based on GPS measurements with the Trimble R7 and a significance level α of 0.05.

The average of the 8 observed high water phase lag ϵ_{hw} is 71 minutes. This is slightly longer than the average low water phase lag ϵ_{LW} of 68 minutes. A slight difference is expected, which is caused by the complex tidal propagation in estuaries. This effect is also described by [Haas, 2007], [Horrevoets, 2002] and [Lievens, 2010].

The observed phase lags at 1-5 July show a standard deviation σ about the mean of 4.7 minutes for the high water phase lag based and 7.5 minutes for the low water phase lag both are based on 8 observations. This holds under the assumption that: the phase lag includes, for the five measurement days, exactly the same time span.

The precision of the standard deviation σ_σ is in this case significant due to limited number of the phase lag estimates. It is shown in [Amiri-Simkooei, 2007] that the precision of the
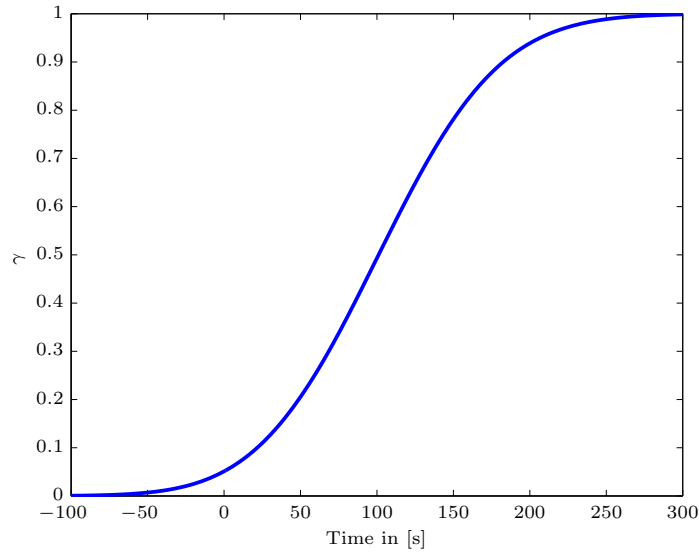
Figure 4.24: This graph shows the probability of detection γ as a function of the buoy dynamics in time. The level of significance is chosen at $\alpha = 0.05$. $T = 0s$ is the very moment the observed extension E is equal to the extension related to slack tide E_{st}. At this particular moment $\alpha = \gamma$. As time progresses the probability of detection γ increases until $\gamma = 1$. The input data is the smoothed average extension observed with the Trimble R7 receiver and is used in this analysis as a ground-truth of for the extension.

standard deviation estimate can be approximated using the following equations:

$$\sigma_{\hat{\sigma}} \approx \frac{\sigma_{\hat{\sigma}^2}}{2\hat{\sigma}} \tag{4.28}$$

Where

$$\sigma_{\hat{\sigma}^2} = \sqrt{\frac{2\sigma^4}{m - n}} \tag{4.29}$$

Where n stands for the number of unknowns, which in this case is 1 (the phase lag) and m for the number of estimated phase lags which equals 8. This results in $\sigma_{\hat{\sigma}^2} = 1.25$ minutes for the high water phase lag and $\sigma_{\hat{\sigma}^2} = 2.01$ minutes for the low water phase lag.
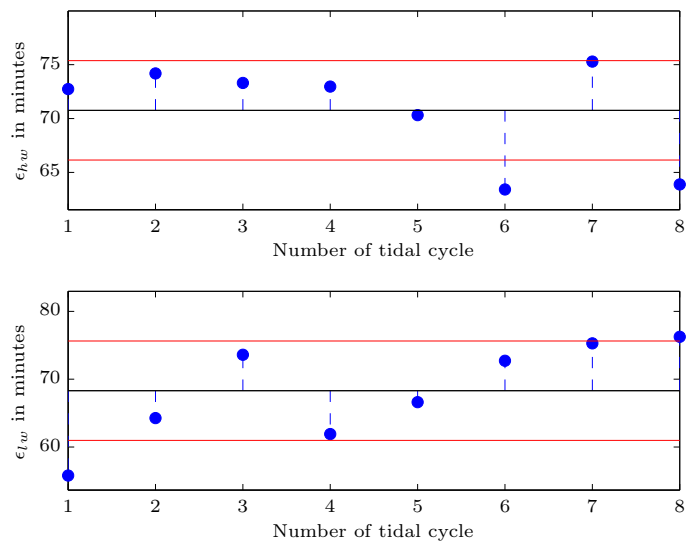
Figure 4.25: These graphs show the high water phase lag ϵ_{hw} and low water phase lag ϵ_{lw} at the location of buoy 18 in the Schelde Estuary (in the vicinity of Terneuzen). The moment of slack tide is found with hypothesis testing using a significance level α of 0.05. The moment of high water is derived from a tidal observation station in Terneuzen (RWS). The black line represents the mean phase lag based on 8 observation. The results of the estimated high water phase lag have a standard deviation of 4.7 minutes. For the estimates of the low water phase lag this is slightly larger: σ equals 7.5 minutes. This is shown in the graph with the red line. Observation date is 1 till 5 July 2011.

4.8 Validation of the estimated phase lag

This section describes the results of the validation of the average estimated phase lag against: the SOBEK model, the phase lag equation and the current observations.

4.8.1 Modelled phase lag: SOBEK and the phase lag equation

Figure 4.26 shows the phase lag obtained with: the SOBEK model (29 June 1998 - spring tide) [Nguyen, 2008], the phase lag equation (29 June 1998) [Savenije, 2005] and the average estimated phase lag at buoy 18 (1-5 July 2011 - 3 July 2011 is spring tide). The average phase lag at buoy 18 is in the same order of magnitude as the computed phase lags.

The difference between the results of the phase lag equation and the average phase lag of buoy 18 is fairly large. The phase lag equation, well appreciated for its simplicity, does not differentiate between a high water and low water phase lag. Which results in a difference of approximately 23 and 26 minutes.

The results of the SOBEK model and the average phase lag of buoy 18 are in close agreement for the high water phase lag, but show a a large difference for the low water phase lag. The difference for the high water phase lag is around 10 minutes, while for the low water phase lag this is approximately 30 minutes.

The next subsection validates the phase lag at buoy 18 against ADCP current observations.
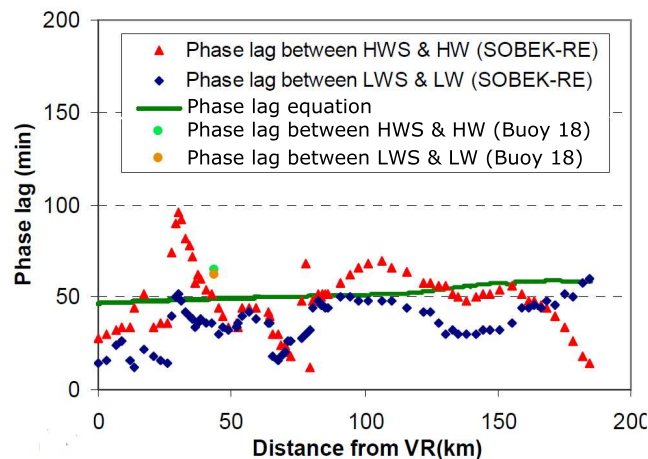

Figure 4.26: This graph shows the phase lags obtained with: the phase lag equation (29 June 1998 - spring tide), the SOBEK model (29 June 1998 - spring tide) and the average estimated phase lag at buoy 18 (1-5 July 2011 - 3 July 2011 is spring tide). Buoy 18 is approximately 42 km from "de Vlakte van de Raan" (VR). Image is adapted and taken from [Nguyen, 2008].

4.8.2   ADCP observations in "De Pas van Terneuzen"

Figure 4.27 shows the phase lag for high water ϵ_{hw} and low water ϵ_{lw} based on the interpretation of the ADCP measurements. The interpretation of the ADCP measurements to find the moment of slack tide is represented graphically in the appendix B.2. Based on this interpretation ϵ_{lw} is equal to 65 minutes and ϵ_{hw} equals 68 minutes.

The average estimated phase lags from buoy 18 are in close agreement with the results from the ADCP measurements. The difference is 3 minutes for ϵ_{hw}, and 3 minutes for ϵ_{lw}. However, due to the measurement interval of the water level and water current there is room for an interpretation error, which is in the worst case 2 times 10 minutes. Therefore, should the results be interpreted carefully.
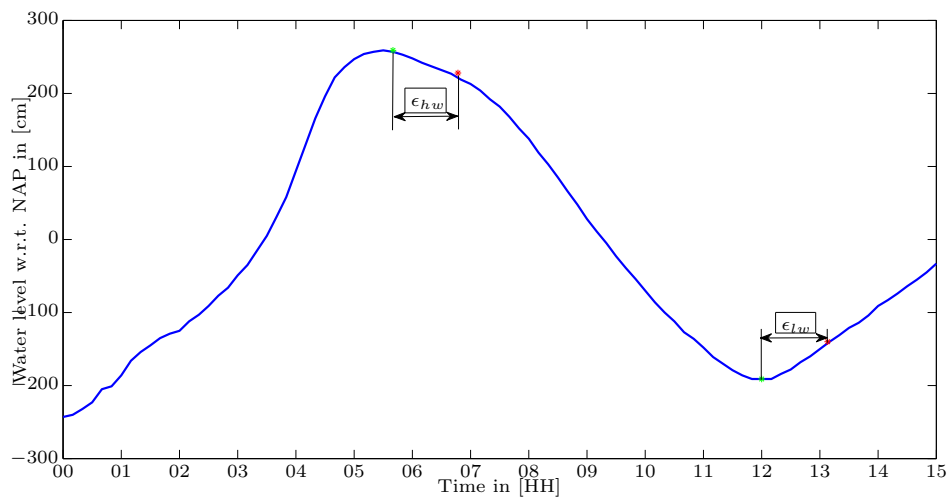
Figure 4.27: This figure shows the low water phase lag $\epsilon_l w$ and high water phase lag ϵ_{hw} based on the ADCP measurement and the observed tidal elevation at Terneuzen of RWS. The moment of slack tide is found by interpreting the ADCP plots which can be found in the appendix B.2. High and low water are found using a simple numerical minimum and maximum algorithm. This results in $\epsilon_{hw} = 68$ min and $\epsilon_{lw} = 65$ min.

Chapter 5

Conclusions and Recommendations

This chapter contains the conclusions and recommendations of this thesis. The main conclusion is drawn in section 5.1. Furthermore are the subquestions answered based on the results of this research. In section 5.2 the recommendations with regard to the design of an operational system are given.

5.1   Conclusions

The main conclusion: the estimation of slack tide based on GPS measurements on a buoy can be accomplished with an accuracy better than 10 minutes.

Which GPS receiver, antenna and operating method is most suited for this specific goal? Based on the results, which demonstrate the performance of different GPS receivers and antennas in different operating modes in terms of accuracy and precision and the influence of this precision on the slack tide detection method it can be concluded that: a single frequency mid-range receiver with a survey antenna in SBAS mode offers an optimum between the complexity of the equipment and the detection delay. This implies a GPS-receiver with a wide front-end bandwidth (e.g. 10 MHz or more) and a pseudorange precision of several decimeters. For example: the Septentrio AsteRx1 1.4.0 in combination with the PolaNt antenna.

What is the actual motion of the buoy during a tidal cycle? The three-dimensional motion of the buoy can be described by: a local vertical motion caused by the vertical tidal wave; a horizontal movement described by a main component caused by the tidal current and perpendicular to this component a fairly small residual movement. Furthermore a high-frequent oscillatory movement is observed in all three directions due to the wind-induced waves.

What is the most suitable navigation data from the GPS measurements? The most suitable navigation data, which is the navigation data that contains the most information with regard to the moment of slack tide, is the relative local two-dimensional

(horizontal) position. Absolute position brings no additional benefits, since the position of the anchor is based on the observed positions of the buoy. Velocity estimates and displacements contain no useful information for the following reasons: the time-averaged velocity of the buoy never exceeds more than 1 cm/s; and in addition to this, the observed instantaneous velocity is in the order of meters per second, which is caused by the three-dimensional high frequency oscillatory motion due to the wind-induced waves.

What is a suitable method to estimate the moment of slack tide based on GPS measurements on the buoy? Composite hypothesis testing is found to be a suitable method to detect the moment of slack tide based on GPS measurement on buoys. The test is designed to determine whether the extension of the buoy is either larger or smaller than the extension related to the moment of slack tide. First, a relation between the moment of slack tide and the position of the buoy is developed. This relation depends on the charted depth and water level, the buoy's draft, the tidal elevation and the length anchor chain; which are provided by the Department of Waterways and Public Works. This implies that the moment of slack tide is directly dependent on the accuracy of these provided values. However, the maximum extension of the buoy appeared to be in reasonable agreement with these provided values. Second, a stochastic model was developed for: the buoy dynamics that are not related to the tidal current; the moment of slack tide and the GPS position estimates. The results of composite hypothesis testing showed a precision about the mean of around 5 minutes for high water slack, and 7 minutes for low water slack.

How do the results compare against nearby measurements of the water current and estuary tidal propagation models? The estimated phase lags at buoy 18 obtained with the proposed method showed a fairly large bias with respect to the analytical phase lag equation. A small improvement is noticed by a comparison of the estimated phase lag against a one-dimensional hydraulic modelling system (SOBEK). The differences can be explained by the fact that: the (analytical) tidal propagation models provide a cross-sectional average phase lag, while the estimated phase lag only holds for the very location of the buoy. However the results are in good agreement with the detailed current measurements. Based on this validation the initial requirement, which is the detection of slack tide with an accuracy less then 10 minutes, is fulfilled.

Can the method be further improved by including the knowledge about the dynamics of the buoys and series of measurement as opposed to a single epoch slack tide estimation? A significant improvement in the precision, of about 60-70%, of the estimated one-dimensional extension is obtained by the application of a Kalman filter algorithm. For the Kalman filter the dynamics of the buoy are modelled as a dampened mass-spring system, which appears to be a valid approximation. An increase of the precision of the extension results in a decrease of the detection delay. The detection delay decreases approximately with 1.5 minutes. Therefore it is concluded that a Kalman filter algorithm improves the estimation of slack tide.

5.2   Recommendations

In this section the recommendations are presented. Furthermore, it describes the procedures of a recommended operational system to monitor and observe the moment of slack tide in estuaries based on GPS measurements on a buoy.

- A mid-range receiver is recommended, this implies a receiver with a psuedorange accuracy of a decimeter. This receiver should be used with a survey antenna and operated in SBAS mode.This recommended equipment offers an optimum between cost and the detection delay of the moment of slack tide. For example the Septentrio AsteRx1 with the PolaNt antenna in SBAS mode. It is important to remind that for the SBAS corrections no additional local infrastructure is necessary.

- For real-time implementation it is suggested to combine this GPS receiver with a wireless data link and power supply, which is described by [Berghuijs & Osnabrugge, 2011].

- It is recommended to choose an ATON buoy that is located in an ebb or flood channel and therefore subject to one dominant current direction.

- For further improvement of the precision of the estimated slack tide, it is recommended to apply Kalman filtering to the observed extensions.

- The following procedures with regard to an operational system to monitor and observe the moment of slack tide in estuaries based on GPS measurements on a buoy are recommended:

  - **Initial Phase** In the initial phase, the most important variables are determined by an analysis of the buoy's motion. Furthermore some parameters that describe the moment of slack tide need to be acquired.

    * Determine or acquire the following information: the length of the anchor chain, the draft of the buoy, the horizontal tidal amplitude during the measurements at the location of the buoy, and the water depth at the approximate location of the anchor with a manual sounding or with hydrographic map.
    * Find the dominant current direction using principle component analysis based on observations of the buoy's position during several tidal cycles.
    * Determine the centre point, with equation 3.5 based on the observed extensions of the buoy during several tidal cycles.
    * Validate the information about the chain length, water depth, water level and buoy draft, which results in a theoretical maximal extension, against the observed maximal extension. The extension of the moment of slack tide is now a function (see eq:4.23) of these validated variables.
    * Combine the stochastic properties of: the buoy's motion that is not related to the tidal current; the GPS measurement set-up and the definition the moment of slack tide using equation 4.26.

  - **Operational Phase** In the operational phase, the moment of slack tide is found by an analysis of the measurements of the position the buoy.

    * Project the observed horizontal buoy positions on to the dominant current direction and relate these to the defined centre point. This yields the observed extension.
    * Use composite hypothesis testing to test wheter the extension of the buoy is either larger or smaller than the extension related to moment of slack

tide by equation (3.12), the first positive test in a time series of tests defines the moment of slack tide.

* The phase lag is obtained by computing the time difference between the moment of slack tide and the moment of high/low water. Therefore the observed water levels from a nearby tidal measurement station are necessary.

References

Amiri-Simkooei, A. (2007). *Least-Squares Variance Component Estimation: Theory and GPS Application.* Unpublished doctoral dissertation, TU Delft.

Anonymous. (2008). *Global Positioning System Standard Positioning Service Performance Standard* (Tech. Rep.). United States Department of Defense for Command, Control, Communications, and Intelligence.

Berghuijs, W., & Osnabrugge, B. (2011). *The development of an autonomous GPS system to monitor tidal slack in estuaries: A survey of hardware and algorithm options.*

Boon, P. (2011). *Westerschelde Vak 18: dieptelijnen en dieptecijfers.* (Tech. Rep.). Department of Waterways and Public Works.

Braasch, M., & Dierendonck van, A. (1999). GPS receiver architectures and measurements. *Proceedings of the IEEE*, *87*(1), 48–64.

DeLoach, S. (1995). *GPS Tides: a project to determine tidal datums with the Global Positioning System.* Army Topograhic Engineering Center Alexendria VA.

Eck, B. (1999). De schelde-atlas, een beeld van een estuarium. *Schelde Informatie Centrum, Middelburg.*

Garmin. (2011, April). *Garmin owner manual for the GPSMAP 76Cx and 76CSx* (Tech. Rep.). Garmin International, Inc. http://www8.garmin.com/manuals/GPSMAP76csx_OwnersManual.pdf.

Gauthier, L., Michel, P., Ventura-Traveset, J., & Benedicto, J. (2001). EGNOS: The First Step in Europe's Contribution to the Global Navigation Satellite System. *ESA bulletin*, *105*, 35–42.

Haas, J. (2007). *Phase lags in alluvial estuaries.* Unpublished master's thesis, TU Delft.

Hamilton, R., & Wright, D. (2009). Physical Oceanographic Real-time System. *Hydro International*, *13*, 16-19.

Horrevoets, A. (2002). *1d-modelleren van het schelde-estuarium.* Unpublished master's thesis, TU Delft.

Hughes, W. J. (2001). *Global Positioning System (GPS) Standard Positioning Service (SPS) Performance Analysis Report.* Technical Center NSTB/WAAS TE Team Atlantic City International Airport, NJ 08405.

Jolliffe, I. (2002). *Principal component analysis* (Vol. 2). Wiley Online Library.

Joosten, P., & Tiberius, C. (2002). LAMBDA: FAQs. *GPS Solutions*, *6*(1), 109–114.

Kato, T., Terada, Y., Kinoshita, M., & Kakimoto. (2000). Real-time observation of tsunami by RTK-GPS. *Earth Planets and Space*, *52*(10), 841–846.

Kato, T., Terada, Y., Kinoshita, M., Kakimoto, H., Isshiki, H., Moriguchi, T., et al. (2001). A new tsunami monitoring system using RTK-GPS. In *US National Tsunami Hazard Mitigation Program Review and International Tsunami Symposium* (pp. 7–10).

Leeuwen, S. Storm van, Marel, H. v. d., Toissant, M., & Martelucci, A. (2004). *Validation of SBAS MOPS Troposphere Model over the EGNOS Service Area* (Tech. Rep.). Nationaal Lucht- en Ruimtevaartlaboratorium.

Lievens, M. (2010). *Observing tidal slack in the Scheldt estuary.* Unpublished master's thesis, TU Delft.

Meriam, J., & Kraige, L. (2006). *Engineering mechanic (vol. 2) dynamics 5th ed.* Wiley-India.

Misra, P., & Enge, P. (2006). *Global Positioning System: Signals, Measurements and Performance Second Edition.* Lincoln, MA: Ganga-Jamuna Press.

Mott, R. (2009). *Toegepaste stromingsleer.* Pearson Education.

Nagai, T., Kato, T., Moritani, N., Izumi, H., Terada, Y., & Mitsui, M. (2006). Offshore Tsunami Monitoring Network Design Using GPS Buoys and Coastal On-Site Sensors. In *Coastal Engineering Conference* (Vol. 30, p. 1529).

Nagai, T., Ogawa, H., Terada, Y., Kato, T., & Kudaka, M. (2004). GPS buoy application to offshore wave, tsunami and tide observation. In *Coastal Engineering Conference* (Vol. 29, p. 1093).

Nguyen, A. (2008). *Salt intrusion, tides and mixing in multi-channel estuaries.* Taylor & Francis.

NOAA. (2011, April). *The challenge of measuring water currents.* http://co-ops.nos.noaa.gov/meascurr.htm.

NRC. (2003). *The Accuracy of Precise Point Positioning from the Canadian Geodetic Service of Natural Resources Canada.* http://www.geod.nrcan.gc.ca/products-produits/ppp_acc_e.php.

Pearson, K. (1901). LIII. On lines and planes of closest fit to systems of points in space. *Philosophical Magazine Series 6*, *2*(11), 559–572.

Rijkswaterstaat. (2011a, June). *Personal communication with J. van Espen with regard to physical dimensions of Buoy 18.*

Rijkswaterstaat. (2011b). *Presentatie meetresultaten: Debiet - sediment - osm meting* (Tech. Rep.).

Savenije, H. (1992). *Rapid assessment technique for salt intrusion in alluvial estuaries.* Unpublished doctoral dissertation, TU Delft.

Savenije, H. (2001). A simple analytical expression to describe tidal damping or amplification. *Journal of Hydrology*, *243*(3-4), 205–215.

Savenije, H. (2005). *Salinity and tides in alluvial estuaries.* Elsevier LTD.

Schmidt, W., Woodward, B., Millikan, K., Guza, R., Raubenheimer, B., & Elgar, S. (2003). A GPS-Tracked Surf Zone Drifter. *Journal of Atmospheric and Oceanic Technology*, *20*(7), 1069–1075.

Septentrio. (2006). *AsteRx1: GPS/Galileo Single-frequency OEM Receiver* (Tech. Rep.). Septentrio Satellite Navigation. http://www.navtechgps.com/Downloads/AsteRx1.pdf.

Septentrio. (2011, September). *Septentrio PolaNt SF high precision geodetic antenna.* (Tech. Rep.). Septentrio Satellite Navigation. http://www.septentrio.com/products/antennas/polant-sf.

Serrano, L., Kim, D., Langley, R., Itani, K., & Ueno, M. (2004). A GPS velocity sensor: how accurate can it be? In *ION NTM* (pp. 875–885).

Stive, M., & Bosboom, J. (2011). *Coastal Dynamics.* VSSD.

Talke, S., & Swart, H. de. (2006). Hydrodynamics and Morphology in the Ems/Dollard Estuary: Review of Models, Measurements, Scientific Literature, and the Effects of Changing Conditions. *Institute for Marine and Atmospheric Research Utrecht (IMAU).*

Teunissen, P. (2001). *Dynamic data processing: Recursive least squares.* Delft University.

Teunissen, P., Simons, D., & Tiberius, C. (2005). *Probability and observation theory.* Department of Earth Observation and Space systems, Faculty of Aerospace Engineering, Delft University of Technology.

Trimble, U. (2001). Trimble Geomatics Office, User Guide. *Trimble Navigation Limited, USA*, *1*, 2.

Van Veen, J. (1950). Eb-en vloedschaar systemen in de nederlandse getijwateren, tijdschr. *Koninkl. Ned. Aardrijkskundig Genootschap*, *67*, 303–325.

Vincotech. (2011, April). *A Description of the Vincotech GPS Receiver Modules A1084-A/-B* (Tech. Rep.). Vincotech GmbH. http://download.vincotech.com//GPS20Receiver20A108420V1.3.pdf.

Yoo, Y., Hou, D., Kouguchi, N., Ishida, H., Shiotani, S., Fujii, H., et al. (2004). Arrayed GPS-buoys wave observation system. In *OCEANS'04. MTTS/IEEE TECHNO-OCEAN'04* (Vol. 3, pp. 1370–1375).

Appendix A

Details of the GPS Receivers

A.1   GPS receivers and firmware

GPS Receiver	Specification 1	Specification 2
Vincotech A1084	Firmware version 3.5.2	
Garmin GPS 76 C(S)x	Software version 4.00	GPSSW version 3.00s
Septentrio AsteRx1 1.4.0	Boot loader version 1.7	GNSSFW version 1.4.0
Trimble R7	Version 2.32	

Table A.1: GPS receiver specification

A.2   Factsheets
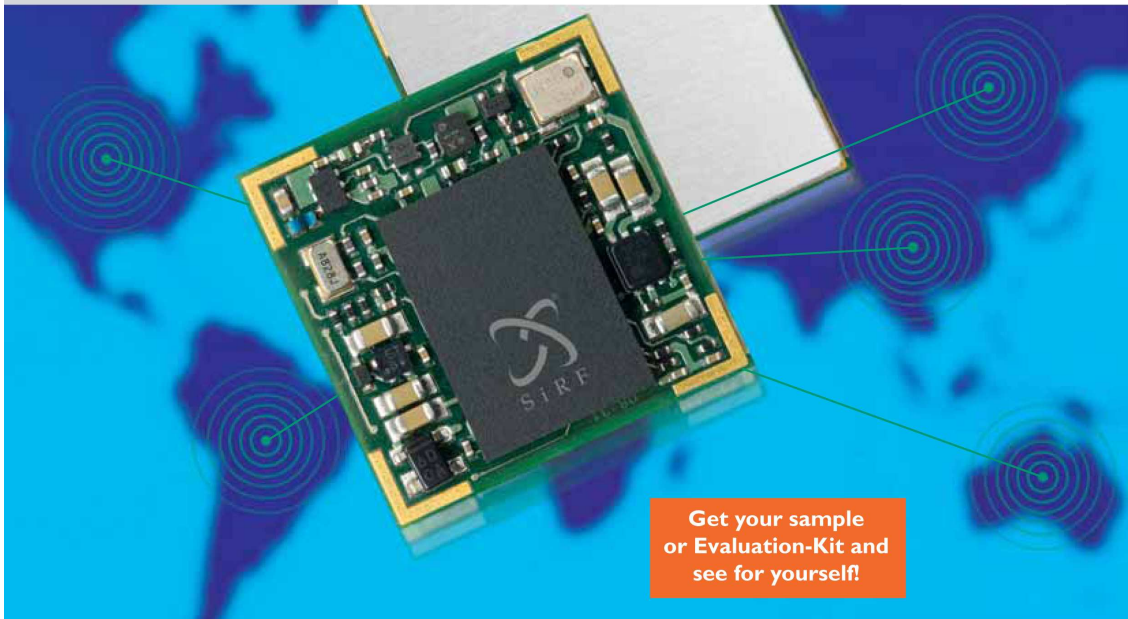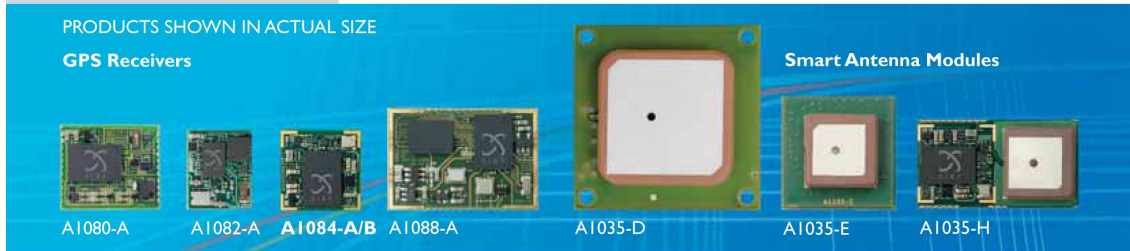
A1084-A/B

Positioning Products

Miniaturized GPS receiver
for passive and active antennas

Many GPS applications, such as portable devices or telematics units, require a built-in antenna. However, an external antenna connector is often desired for GPS performance or reliability reasons. This is what the new A1084-A GPS receiver supports with its second antenna pin and on board antenna switch, whilst the A1084-B supports both passive and active antennas on a single antenna pin. This very compact SiRFStar III based GPS receiver comes completely shielded with a lid and with benchmark-setting GPS performance on a very small footprint.

Bench marking sensitivity	■ -159 dBm tracking
Fastest TTFF (Time To First Fix)	■ < 35 s under cold start conditions (typical)
Ultra-low power consumption	■ 86 mW average in tracking mode
Smallest footprint	■ 15 x 15 mm^2
Antenna	■ Passive and active antenna supported
Dual antenna support	■ RF switch on A1084-A

Positioning Receiver Portfolio

With the mission to support our customers in implementing GPS functionality into their systems, Vincotech is offering a large product portfolio to cover almost all integration possibilities in an easy way. A dedicated R&D team located in the Munich region, Germany, develops sensitive positioning solutions based on state of the art technologies. All GPS products are manufactured in our ISO9001 and TS16949 certified factory in the EU. Our modules comply to the RoHS standard and are 100% electrically and functionally tested prior to packaging. This way we constantly guarantee high quality products.

PRODUCTS SHOWN IN ACTUAL SIZE

GPS Receivers   **Smart Antenna Modules**

A1080-A   A1082-A   **A1084-A/B**   A1088-A   A1035-D   A1035-E   A1035-H

GPS Receivers	Supply voltage / V	Current draw @Ifix per sec. / mA	Operating temperature / °C	Low Power Mode Trickle Power	Low Power Mode Push-To-Fix	Low Power Mode Keep Ephemeris Alive	AGPS Ephemeris Push	Active antenna	Passive antenna	2nd antenna input Antenna switch	Internal antenna supply	Firmware update (Flash)	ROM	SBAS support	Back-up battery option	Shielding lid	AEC-Q compliant components	Size / mm²
A1080-A	3.3	23	-30/85	■	■		■	■			■	■		■	■			19×16
A1080-B	3.3	23	-40/85	■	■		■	■			■	■		■	■			19×16
A1082-A	1.8	35	-30/85			■		■					■		*			14×12
A1084-A	3.3	26	-30/85	■	■		■	■	■	■	■	■		■	■	■	15×15
A1084-B	3.3	26	-30/85	■	■		■	■	■		■	■		■	■	■	15×15
A1088-A	3.3	30	-40/85			■	■				■	■		■	■	■	28×19

*SRAM backup possible with Enable pin

Smart Antenna Modules	Antenna type	Circular polarisation	Linear polarisation	Plug-in module	SMD solderable	External antenna pin	Shielding lid	Size / mm²	Based on GPS receiver
A1035-D	patch	■		■			■	35×35	A1080-A
A1035-E	patch	■		■				21×21	A1082-A
A1035-H	patch	■			■	■	■	30×17	A1084-A
A1085-A**	chip		■		■		■	31×17	A1080-A
A1086-A**	meander		■		■	■	t.b.d.	25×15	A1084-A
A1086-B**	meander		■		■		t.b.d.	25×15	A1084-A

**product planned
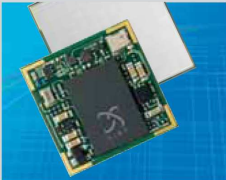
Technical Details A1084-A/B

PERFORMANCE

Channels	20 parallel tracking
Correlators	200,000 plus
Frequency	L1 – 1,575 MHz
Sensitivity	
Tracking	-159 dBm
Acquisition (cold start)	-142 dBm
Position accuracy	< 2.5 m CEP autonomous
(horizontal)	< 2.0 m CEP SBAS
Time To First Fix	
Hot start[1]	< 1 s
Warm start[2]	< 32 s
Cold start[3]	< 35 s

COMMUNICATION

Standard GPS software	
NMEA message switchable	GGA, GSA, GSV, VTG, RMC, GLL
Baud rate	4,800 (default) to 115,200
Serial ports	3.3 V CMOS compatible
Tx0	NMEA output
Rx0	NMEA input

1) The receiver has estimates of time/date/position and valid almanac and ephemeris data.
2) The receiver has estimates of time/date/position and almanac
3) The receiver has no estimate of time/date/position, and no recent almanac
4) An external current limiter is suggested to avoid damage in fault conditions

The information provided herein is believed to be reliable at press time. Vincotech assumes no responsibility for inaccuracies or omission. Vincotech assumes no responsibility for the use of this information, and all such information shall be entirely at the users own risk. Prices and specifications are subject to change without notice. Vincotech does not authorize or warrant any of its products for use in lifesupport devices and/or systems.

ENVIRONMENT

Temperature	
Operating	-30° to +85°C
Storage	-40° to +85°C
Humidity	Non condensing

POWER

Supply voltage	3.0 to 3.6 VDC
Current draw	
Acquisition	31 mA (typical)
Tracking	26 mA (typical)
Standby	20 µA (typical)
Antenna supply via VANT	
Voltage range	up to 5.0 V
Max. allowed current[4]	50 mA

MECHANICAL

Dimensions	15.2 × 15.2 × 2.4 mm³
	0.6" × 0.6" × 0.1"
Weight	1.2 g / 0.042 oz.

YOUR PARTNER

Vincotech GmbH
Biberger Straße 93
82008 Unterhaching/Germany

Phone   +49 (0)89 8780 67-0
Fax   +49 (0)89 8780 67-300

www.vincotech.com/gps

Vincotech
power.position.service

GARMIN   GPSMAP® 76Cx and 76CSx

Amazing detail and color meet

high-sensitivity GPS performance in

Waterproof navigation with a splash of color

the GPSMAP 76Cx and 76CSx.

These mariner-friendly handhelds are

WAAS-enabled, waterproof, and they'll

even float if dropped overboard.

They're set to go the distance on land

or sea thanks to a long battery life

and 128 megabytes of microSD

card memory for loading optional

MapSource® detail: BlueChart®,

City Navigator™, TOPO, and more.

The 76CSx adds electronic compass and

barometric altimeter for extremely

accurate heading and elevation readings.

Automatic pressure trend recording even

lets you can keep an eye on the weather.

GARMIN

GPSMAP® 76Cx and 76CSx

Navigation features

Waypoints/icons:	1000 with name and graphic symbol, 10 proximity
Routes:	50 reversible routes with up to 250 points each, plus MOB and TracBack® modes
Tracks:	Automatic track log; 20 saved tracks let you retrace your path in both directions
Trip computer:	Current speed, average speed, resettable max. speed, trip timer and trip distance
Alarms:	Anchor drag, approach and arrival, off-course, proximity waypoint, shallow water and deep water
Tables:	Built-in celestial tables for best times to fish and hunt, sun and moon rise/set based on date and location
Map datums:	More than 100 plus user datum
Position format:	Lat/Lon, UTM/UPS, Maidenhead, MGRS, Loran TDs and other grids, including user grid

GPS performance

Receiver:	High sensitivity SiRFstarIII™ GPS receiver; WAAS-enabled; continuously tracks and updates your position
Acquisition times*:	
Warm:	<1 sec
Cold:	<38 sec
Factory reset:	<45 sec
Update rate:	1/second, continuous
GPS accuracy:	
Position:	<10 meters, typical
Velocity:	.05 meter/sec steady state
DGPS (WAAS) accuracy:	
Position:	<5 meters, typical
Velocity:	.05 meter/sec steady state
Dynamics:	4 g's
Protocol messages:	NMEA 0183 output protocol
Antenna:	Built-in quad helix receiving antenna, with external antenna connection (MCX)

Moving map features

Basemap:
(GPSMAP 76Cx & 76CSx) Built-in routable basemap (North and South America) with cities, highways, interstates, local thoroughfares and secondary roads within metro areas, interstate exit services, airports, rivers, lakes, coastlines and tide stations

GPSMAP 76Cx   GPS 76CSx

Uploadable maps:
(GPSMAP 76Cx & 76CSx)

Accepts up to 1 GB (gigabyte) microSD™ data card for downloaded map detail from a variety of optional MapSource® media (extra microSD data cards optional)

Electronic compass feature
(GPSMAP 76CSx only)

Accuracy:	±2 degrees with proper calibration (typical); ±5 degrees extreme northern and southern latitudes
Resolution:	1 degree

Barometric altimeter feature
(GPSMAP 76CSx only)

Accuracy:	10 feet with proper calibration (user and/or automatic calibration)
Resolution:	1 foot
Range:	–2,000 to 30,000 feet
Elevation computer:	Current elevation, resettable minimum and maximum elevation, ascent/descent rate, total ascent/descent, average and maximum ascent/descent rate
Pressure:	Local pressure (mbar/inches HG), 48-hour automatic pressure trend recording

Power

Source:	Up to 30 hours (76Cx) Up to 20 hours (76CSx)
Battery life:	Up to 16 hours; 10 hours typical on GPSMAP 76CSx

Physical

Size:	2.7"W x 6.2"H x 1.2"D (6.9 x 15.7 x 3.1 cm)
Weight:	7.7 ounces with batteries (not included)
Display:	1.6"W x 2.2"H (4.1 x 5.6 cm) 256-color transflective TFT display (160 x 240 pixels)
Case:	Fully gasketed, high impact plastic alloy, waterproof to IEC 60529 IPX7 standards
Temp. range:	5ºF to 158ºF (-15ºC to 70ºC)
User data storage:	Indefinite, no memory battery required

Accessories

Standard:	128 MB microSD card PC/USB interface cable MapSource Trip & Waypoint Manager CD Owner's manual Quick reference guide Wrist strap
Optional:	Marine mount Carrying case 12-volt adapter cable Power/data cable Remote GPS antenna

Accepts MapSource® BlueChart® data for detailed offshore cartography

Get detailed street maps plus the location of services with MapSource® City Navigator™.

MapSource TOPO data is ideal for outdoor sports such as hiking or geocaching.

The barometric altimeter feature on the GPSMAP 76CSx provides elevation profiles.

©2006 Garmin Ltd. or its subsidiaries

GARMIN

Specifications are preliminary and subject to change without notice.

*On average for a stationary receiver with an open sky view.

AsteRx1: GPS/Galileo Single-frequency OEM Receiver

The AsteRx1 receiver is the first product in a new family of GNSS receiver boards for demanding industrial applications. AsteRx1 is a creditcard-sized OEM board with low power consumption and high update rates, featuring proven high-quality all-in-view GPS and Galileo tracking and offering excellent measurement quality for high precision positioning, even in challenging environments.

First Industrial Galileo-ready Receiver

The AsteRx1 OEM board is a next generation L1 GPS/Galileo/SBAS OEM receiver platform. It is designed for high-performance single-frequency applications. AsteRx1 features 24 single-frequency channels for all-in-view mixed GPS/Galileo and SBAS tracking. Optionally, all 24 channels can be used for a single satellite constellation. Both GIOVE and Galileo modulations are supported ensuring Galileo support from today on. While AsteRx1 offers access to the signals from tomorrow, it offers an exquisite GNSS module for demanding GPS applications today.

Innovative Technology for Exceptional Performance

Innovative new technology is introduced to maximally benefit from the performance improvement possibilities inherent in the new signals. Longer code lengths and advanced modulation techniques of the Galileo BOC(1,1) signal promise lower noise tracking and lower sensitivity for multipath signals. Septentrio's A Posteriori Multipath Estimator (APME), unique in its ability to tackle short-delay multipath, maximally exploits these benefits. A dedicated acquisition unit avoids long acquisition times inherent to longer code lengths, offering faster acquisition for Galileo signals than was even available for GPS before using traditional techniques.

This results in very robust acquisition and tracking, maintaining excellent low-noise measurement quality for both code and carrier phase, the basis for precise position information and detailed signal and signal quality information. Moreover, high update rates (up to 50 Hz) and low latency (below 10ms, independent of update rate) guarantee flexible deployment even in high-dynamic environments.

Easy to integrate

AsteRx1 features low power consumption (<1W) and is available in a compact OEM board version, making it suitable for on-board as well as portable battery operated applications. For ready-to-use solutions, the AsteRx1 can be delivered in a waterproof IP65 rugged enclosure with sturdy connectors, allowing usage in tough conditions.

Flexible configuration, a powerful command language, a variety of detailed output messages and formats suited for automation, serial and USB2.0 interfaces, all facilitate the work of the system integrator.

Last but not least, as with all Septentrio GNSS receivers, an intuitive, Qt-based GUI – RxControl – can be used with the AsteRx1 for its configuration, for logging and remote control. Moreover, RxControl includes a host of enhanced visualization features. RxControl is available both on Windows and Linux platforms, as well as on WindowsMobile for PDA platforms (as RxMobile).

Future proof

A competitive GPS engine today, with seamless evolution to the new environment with Galileo tomorrow, AsteRx1 offers the ideal future-proof platform for system integrators, planning for maximal performance without the need for hardware upgrades. To this end, the AsteRx1 platform also conforms to the latest legislation, including the European Union's RoHS (Restriction of Hazardous Substances) directive.

AsteRx1 Technical Specifications

FEATURES

- Single-frequency L1 code/carrier tracking of Galileo and GPS signals
- 24 hardware channels for simultaneous tracking of all visible satellites in Galileo + GPS constellations
- Includes up to 3 SBAS channels (EGNOS, WAAS, other)
- Raw data output (code, carrier, SBAS navigation data)
- Up to 50 Hz raw measurement and 20 Hz PVT output rate (user selectable)
- A Posteriori Multipath Estimator technique (APME)
- Differential GPS (rover)
- x PPS output (x = 0.1, 0.5, 1, 2, 5, 10)
- EGNOS and WAAS compatible
- Provision of protection levels in SBAS positioning mode (HPL/VPL)
- RAIM included
- Three serial ports (RS232/LVTTL) and 1 full speed USB port
- Highly compact and detailed Septentrio Binary Format (SBF) output, up to 50 Hz
- NMEA v2.30 output format, up to 5 Hz
- Compact creditcard-size OEM board solution
- OEM board or mounted in IP65 waterproof enclosure
- Includes intuitive GUI (RxControl) and detailed operating and installation manual

OPTIONS

- Differential GPS base station
- RTK (single-frequency)
  RTCM v2.3 or 3.0 input/output
  Reference Station Network compatible (FKP)
  CMR 2.0
- 2 Event markers

FEATURES

Position accuracy[1,2,3]

	Horizontal	Vertical
Standalone	1.7 m	3 m
SBAS	0.7 m	1.2 m
DGPS	0.35 m	0.65 m
RTK[4]	0.2 m	0.35 m

Velocity Accuracy[1,2,3]

	Horizontal	Vertical
Standalone	5.0 mm/sec	8.0 mm/sec

Maximum Output rate 50 Hz
Latency < 10 msec

Time accuracy[3]
1PPS 20 nsec

Measurement precision[1,3,5]
C/A pseudoranges
5 cm (GPS)[6]
15 cm (GPS)[7,8]
30 cm (GPS)[7,9]
8 cm (Galileo L1 BOC)[7,8]
35 cm (SBAS)[7,8]

L1 carrier phase <1 mm

L1 doppler 20 mHz

Time to first fix
Cold start[10] 50 sec
Warm start[11] 40 sec
Hot start[12] 15 sec
Re-acquisition 0.5 sec

Tracking performance (C/N$_0$ threshold)[13,14]
Code phase tracking 19 dB-Hz
Carrier phase tracking 26 dB-Hz
Acquisition 33 dB-Hz
Acceleration 20 g
Jerk 3 g/sec

1 1 Hz measurement rate
2 Performance depends on environmental conditions
3 1σ level
4 Float solution, after convergence
5 C/N0 ≈ 45 dB-Hz
6 Smoothed
7 Non-smoothed
8 Multipath mitigation disabled
9 Multipath mitigation enabled
10 No information available (no almanacs, no approximate position)
11 Almanacs and approximate position known, no ephemeris known
12 Almanacs, ephemeris and approximate position known
13 95%
14 Max speed 515 m/sec, max altitude 18 000 m

PHYSICAL AND ENVIRONMENTAL

Size	56 x 76 x 9 mm
Weight	25g
Input voltage	5 VDC ± 5%
Antenna LNA Power Output	
Output voltage	+ 5VDC
Maximum current	200 mA
Power consumption	< 1 W
Operating temperature	-45 to +85°C
Storage temperature	-55 to +85°C
Humidity	5% to 95% (non condensing)
Input/Output Connectors	
I/O connector	2x40 pins
	(SAMTEC SFM)
Antenna	MMCX
Communications	

3 serial ports (S232/LVL-TTL) up to 115 kbps (user configurable)

1 full speed USB 2.0

OTHER SEPENTRIO PRODUCTS

PolaRx2e and PolaRx2e_OEM – Dual-frequency GNSS receiver platform for high-end applications. Based on code and carrier tracking of the L1 and L2 signals, it provides the user with satellite range measurements and position, velocity and time.

PolaRx2eH - A unique single-board dual-frequency dual-antenna receiver – suitable to being connected to 2 dual-frequency antennas, brings heading and machine control applications within economic and practical reach.

PolaRx2e@ - A unique single-board dual-frequency receiver that can be connected to up to 3 antennas, for various heading/attitude and other multi-antenna applications.

PolaRx2C – The PolaRx2C can track up to 4 satellites in L2C mode. For these satellites, the CA, P1, P2 and L2C measurements are available simultaneously.

GeNeRx1 – A combined GPS/Galileo receiver, which can be flexibly configured to simultaneously track Galileo as well as GPS satellites in multi-frequency mode. All Galileo frequencies and modulations are supported.

PolaNt – A lightweight precise positioning and survey single or dual-frequency antenna for use with PolaRx family.

RxControl - RxControl is an intuitive user interface to configure and control all types of PolaRx receivers and monitor, log and post data remotely.

RxMobile - A unique intuitive, portable GUI field controller for the PolaRx receivers. RxMobile allows controlling the receiver, monitoring the navigation solution and accessing its functions in the field in the same intuitive way as with RxControl.

Although believed to be accurate and reliable, Septentrio reserves the right to alter the above specifications without prior notice. However, no responsibility is assumed by Septentrio for its use, nor for any infringements of patents or other rights of third parties resulting from its use.

Trimble R7 GPS Receiver

*Advanced Dual Frequency GPS and WAAS/EGNOS receiver system
with L2C capability and integrated UHF radio modem*

GENERAL

- Tough, lightweight magnesium alloy casing
- Fully integrated internal radio modem fully sealed
- Incorporates the Trimble R-track technology, which allows tracking of the L2 Civil Signal (L2C)
- CompactFlash data storage expandable up to 128 MB
- Integral USB (Universal Serial Bus) for ultra fast download
- Greater than 10 hours data logging or 7 hours of RTK operation on 2 internal 1.8 ampere-hour lithium-ion batteries
- Tripod clip or integrated base case
- Mount rover on-the-pole, in a belt pouch or in a backpack
- Front panel for control of power, data logging, formatting of CompactFlash cards, ephemeris and application file deletion and restoring default controls. LED indicators for satellite tracking, radio link operation data logging and power monitoring
- Low power consumption

PERFORMANCE SPECIFICATIONS

Measurements

- Advanced Maxwell™[5] Custom Survey GPS Chip
- High precision multiple correlator L1 and L2 pseudorange measurements
- Unfiltered, unsmoothed pseudorange measurements data for low noise, low multipath error, low time domain correlation and high dynamic response
- Very low noise L1 and L2 carrier phase measurements with <1 mm precision in a 1Hz bandwidth
- L1 and L2 Signal-to-Noise ratios reported in dB-Hz
- Proven Trimble low elevation tracking technology
- 24 Channels L1 C/A Code, L2C[8], L1/L2 Full Cycle Carrier, WAAS/EGNOS Support

Code Differential GPS Positioning[7]

Horizontal	0.25 m + 1 ppm RMS
Vertical	0.50 m + 1 ppm RMS

WAAS differential positioning accuracy typically <5 m 3DRMS[1]

Static and Fast Static GPS Surveying[7]

Horizontal	±5 mm + 0.5 ppm RMS
Vertical	±5 mm + 1 ppm RMS

Kinematic Surveying[7]

Real-time and Postprocessed Kinematic Surveys

Horizontal	10 mm + 1 ppm RMS
Vertical	20 mm + 1 ppm RMS
	0.02 seconds (20 millisecond) latency
Initialization time	Single/Multi-Base eRTK min 10 secs +0.5 times baseline length in km, up to 30 km VRS™ (Virtual Reference Stations) initialization time <30 seconds typical anywhere within coverage area
Initialization reliability	Typically >99.9%[2]

eRTK Wide Area Coverage

- Conventional RTK typical coverage 300 sq km (115 sq mi) per base
- Single Base eRTK up to 1,250 sq km (500 sq mi)[3]
- Multiple Base eRTK up to 3,750 sq km (1,500 sq mi)[3,4]
- VRS eRTK 8,500+ sq km (3,300 sq mi)[3,5]

HARDWARE

Physical

Casing	Tough, lightweight fully sealed magnesium alloy
Water/dustproof	IP67 Dustproof, protected from temporary immersion to depth of 1 m (3.28 ft)
Shock and Vibration	Tested and meets the following environmental Standards: Shock MIL-STD-810-F to survive a 1m (3.28ft) drop onto concrete. Vibration MIL-STD-810-F on each axis
Weight	With internal batteries, internal radio, internal battery charger, standard UHF antenna: 1.4 kg (3 lb) As entire RTK Rover with batteries for 7 hours, less than 4 kg (8.8 lb)
Dimensions	13.5 cm W x 8.5 cm H x 24 cm L (5.3 in. W x 3.4 in. H x 9.5 in. L)

Electrical

Power	DC input 10.5 V to 28 V with over voltage protection
Power consumption	2.5 W receiver only, 3.75 W including internal radio
Battery	>10 hours postprocessed, 7 hours RTK (with two 1.8 ah batteries)
Battery weight	0.1 kg (1.6 oz)
Battery charger	Internal with external AC power adapter; no requirement for external charger
Power output	10.5 V to 20 V (Port 1), 10.5 V to 7.5 V (Port 3)
Certification	Class B Part 15 FCC certification and CE Mark approved Environmental
Operating temperature	–40 °C to +65 °C (–40 °F to +149 °F) C-Tick approved
Storage temperature	–40 °C to +80 °C (–40 °F to +176 °F)
Humidity	100%, condensing

COMMUNICATIONS AND DATA STORAGE

- 2 external power ports, 2 internal battery ports, 3 serial ports
- Integrated USB for data download speeds in excess of 1 megabit per second (10 times faster than even the fastest serial port)
- CompactFlash—advanced lightweight and compact removable data storage. Options of 64 MB or 128 MB from Trimble
- More than 3,400 hours continuous L1+L2 logging at 15 seconds with 6 satellites typical (128 MB)
- Fully integrated, fully sealed internal UHF radio modem option
- GSM, Cell Phone and CDPD modem support for eRTK and VRS operation
- Range pole antenna for eRTK Wide Area Real Time Kinematic. For long range UHF communications without interference to GPS antenna phase center
- Dual event marker inputs
- 1 Hz, 2 Hz, 5 Hz and 10 Hz Positioning and Data Logging
- 1 Pulse Per Second Output
- CMRII, CMR+, RTCM 2.1 Input and Output Standard
- 14 NMEA outputs
- Supports BINEX and smoothed carrier

®Trimble.

Trimble R7 GPS Receiver

Advanced Dual Frequency GPS and WAAS/EGNOS receiver system
with L2C capability and integrated UHF radio modem

ZEPHYR™ ANTENNA

- Dimensions: 16.2 cm diameter × 5.7 cm (6.4 in × 2.25 in) maximum depth
- Weight: 0.45 kg (1 lb)
- Operating temperature range: −40 °C to +70 °C (−40 °F to 158 °F)
- 100% humidity proof, fully sealed
- The GPS antenna meets the following environmental standards:
    - MIL-810-F Figure 514 5c-17 vibration levels on each axis
    - Shock tested to MIL-810-F Table 516.5-I to survive a 2 m (6.56 ft) drop
- 4-point antenna feed for sub-mm phase center repeatability.
- Integral Low Noise Amplifier
- 50 dB antenna gain
- Phase Center Repeatability <1 mm horizontal

ZEPHYR GEODETIC™ ANTENNA

- Dimensions: 34.3 cm diameter × 7.6 cm (13.5 in × 3 in) maximum depth
- Weight: 1.0 kg (2.2 lb)
- Operating temperature range: −40 °C to +70 °C(−40 °F to 158 °F)
- 100% humidity proof, fully sealed
- The GPS antenna meets the following environmental standards:
    - MIL-810-F Figure 514 5c-17 vibration levels on each axis
    - Shock tested to MIL-810-F Table 516.5-I to survive a 2 m (6.56 ft) drop
- Shock tested for a drop of 2 m (6.56 ft) onto concrete
- 4-point antenna feed for sub-mm phase center repeatability
- Integral Low Noise Amplifier
- 50 dB antenna gain
- Trimble Stealth™ Ground Plane for reduced multipath
- Phase Center Repeatability <1 mm horizontal

1 *Depends on WAAS system performance.*
2 *May be affected by atmospheric conditions, signal multipath and satellite geometry.*
3 *May require cellular telephone coverage.*
4 *Based on configuration of 3 stations at 40 km spacing.*
5 *Based on configuraiton of 6 stations at 70 km spacing.*
6 *Receiver operates normally to −40 °C but some office based functions such as USB download or internal battery charging are not recommended at temperatures below freezing.*

7 *Accuracy may be subject to conditions such as multipath, obstructions, satellite geometry, atmospheric parameters. Always follow recommended survey practices.*
8 *The availability of L2C signal is dependent on the US Government.*

Specifications subject to change without notice.

Trimble

NORTH AMERICA
Trimble Engineering
& Construction Group
5475 Kellenburger Road
Dayton, Ohio 45424-1099 • USA
800-538-7800 (Toll Free)
+1-937-245-5154 Phone
+1-937-233-9441 Fax
www.trimble.com

EUROPE
Trimble GmbH
Am Prime Parc 11
65479 Raunheim • GERMANY
+49-6142-2100-0 Phone
+49-6142-2100-550 Fax

ASIA-PACIFIC
Trimble Navigation
Singapore Pty Limited
80 Marine Parade Road
#22-06, Parkway Parade
Singapore 449269 • SINGAPORE
+65-6348-2212 Phone
+65-6348-2232 Fax

TRIMBLE AUTHORIZED DISTRIBUTION PARTNER

Appendix B

RWS Measurement campaign

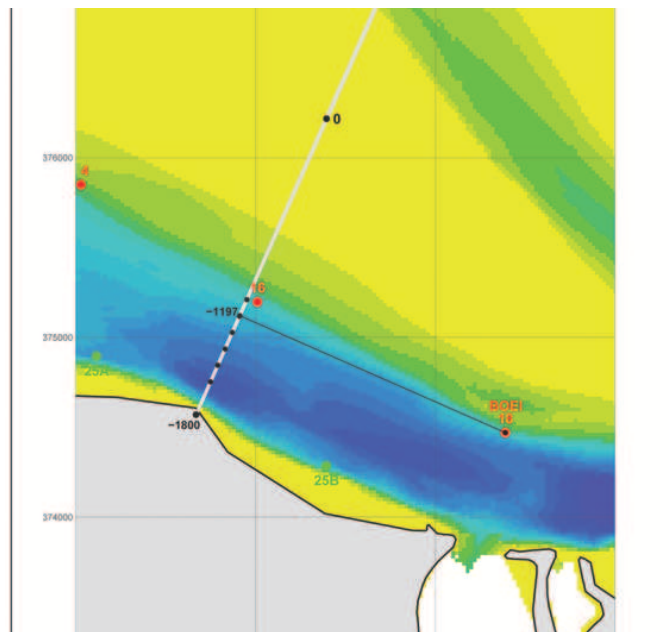## B.1 Overview measurement location

Figure B.1: Overview map of the ADCP measurements from RWS.

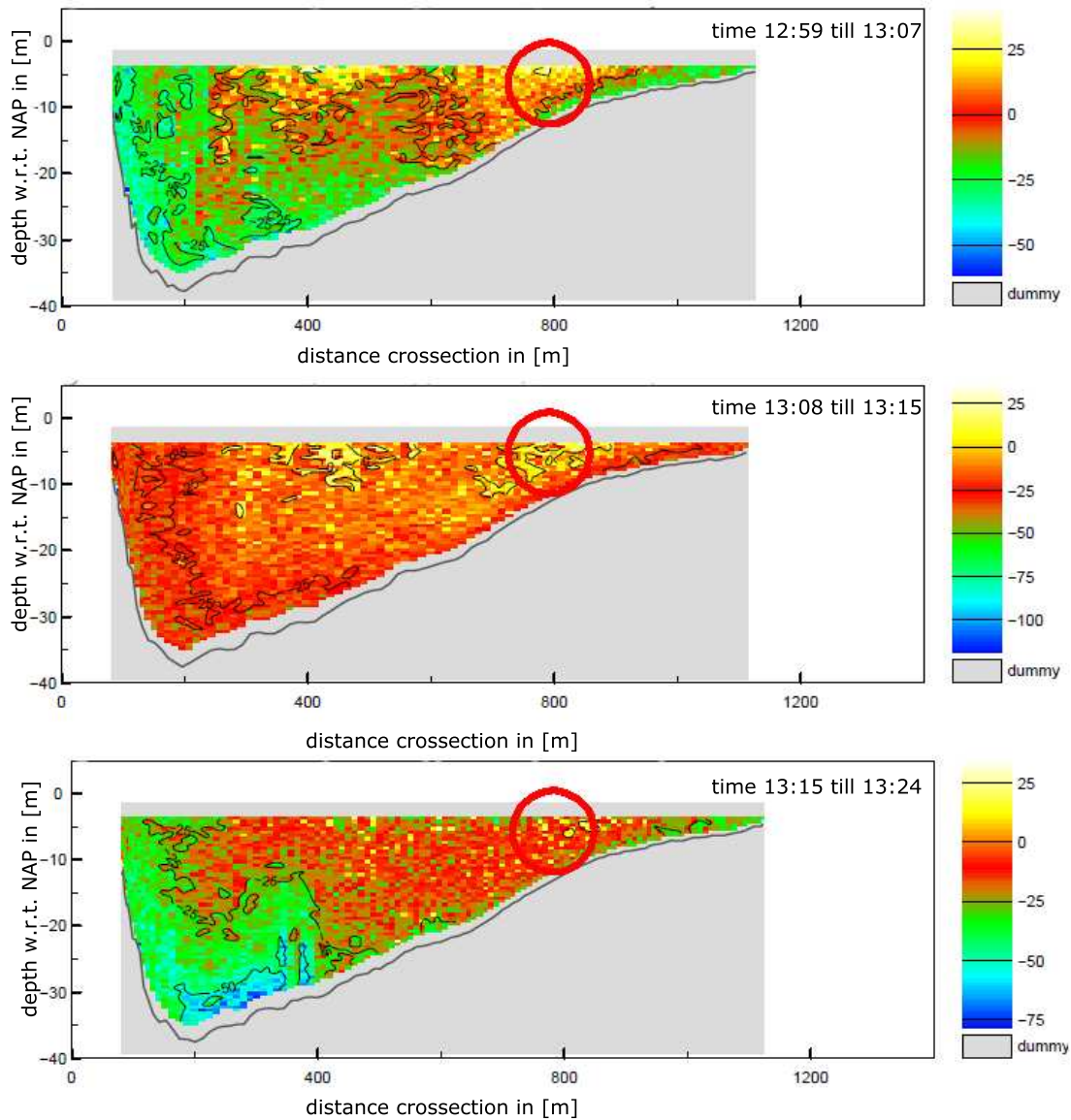## B.2 ADCP current observation around the moment of slack tide

Figure B.2: This figure shows the velocity of the current in the cross-section of 'De Pas van Terneuzen' on 6 July 2011 on three measurement intervals. The time of the measurement interval is denoted in left-top of each graph. Positive values indicate an ebb current, while negative values indicate a flood current. The color bar is inconsistent. The red circle indicates roughly the location of the buoy within the cross section. From top to bottom the graphs show the situation just before, during and after the moment of low water slack.
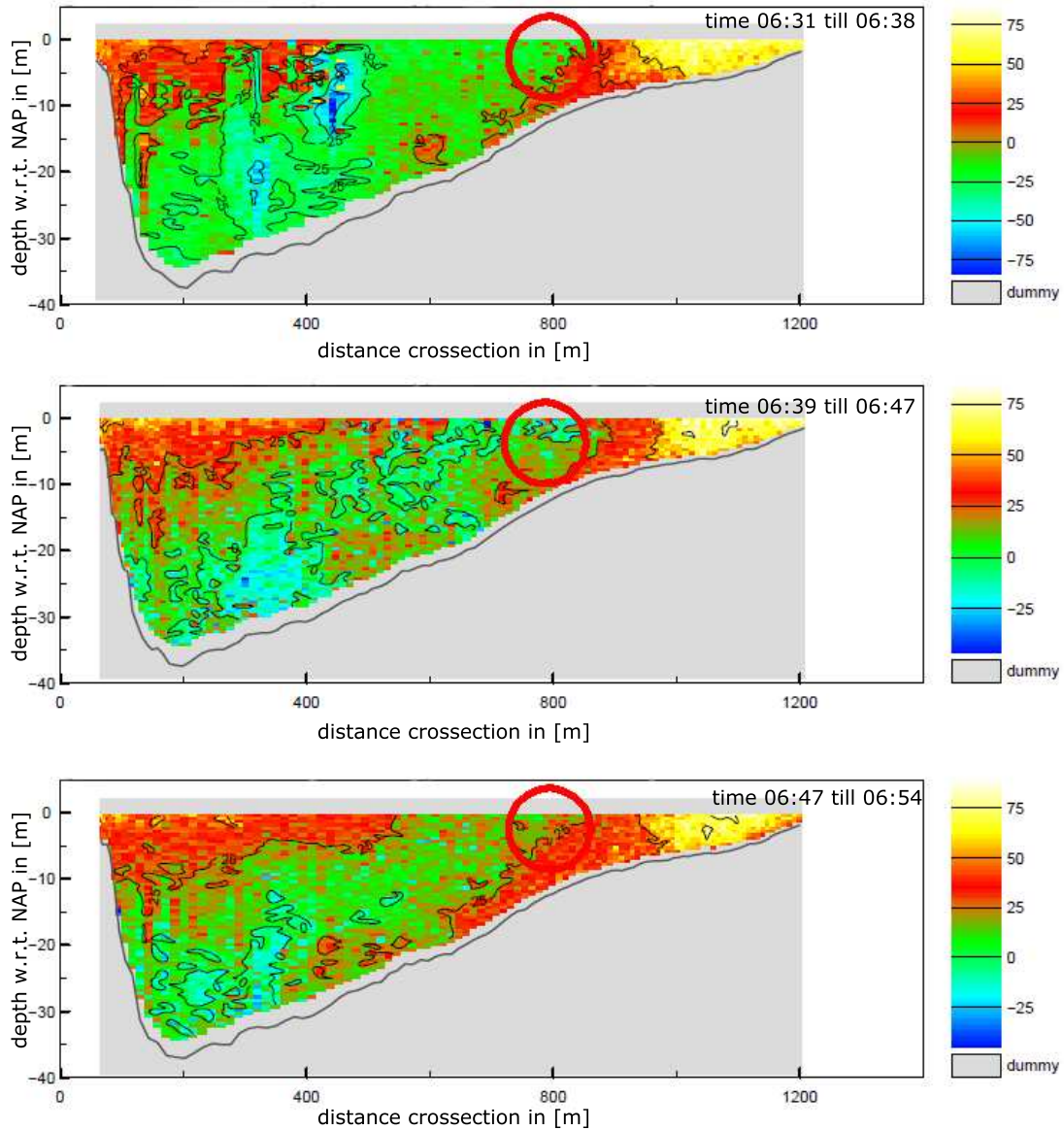
Figure B.3: This figure shows the velocity of the current in the cross-section of 'De Pas van Terneuzen' on 6 July 2011 on three measurement intervals. The time of the measurement interval is denoted in left-top of each graph. Positive values indicate an ebb current, while negative values indicate a flood current. The color bar is inconsistent. The red circle indicates roughly the location of the buoy within the cross section. From top to bottom the graphs show the situation just before, during and after the moment of high water slack.

Appendix C

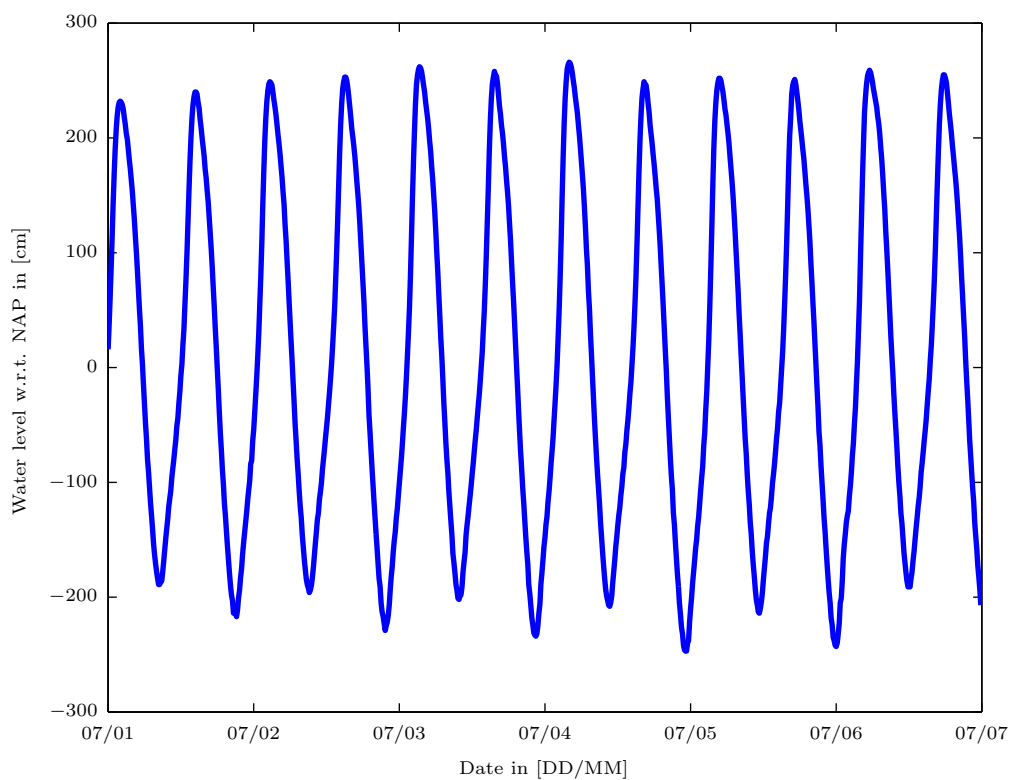# Tidal and meteo information

C.1 Tidal Information

Figure C.1: Observed water level at the RWS measurement station Terneuzen from 1-6 July 2011. Courtesy: RWS
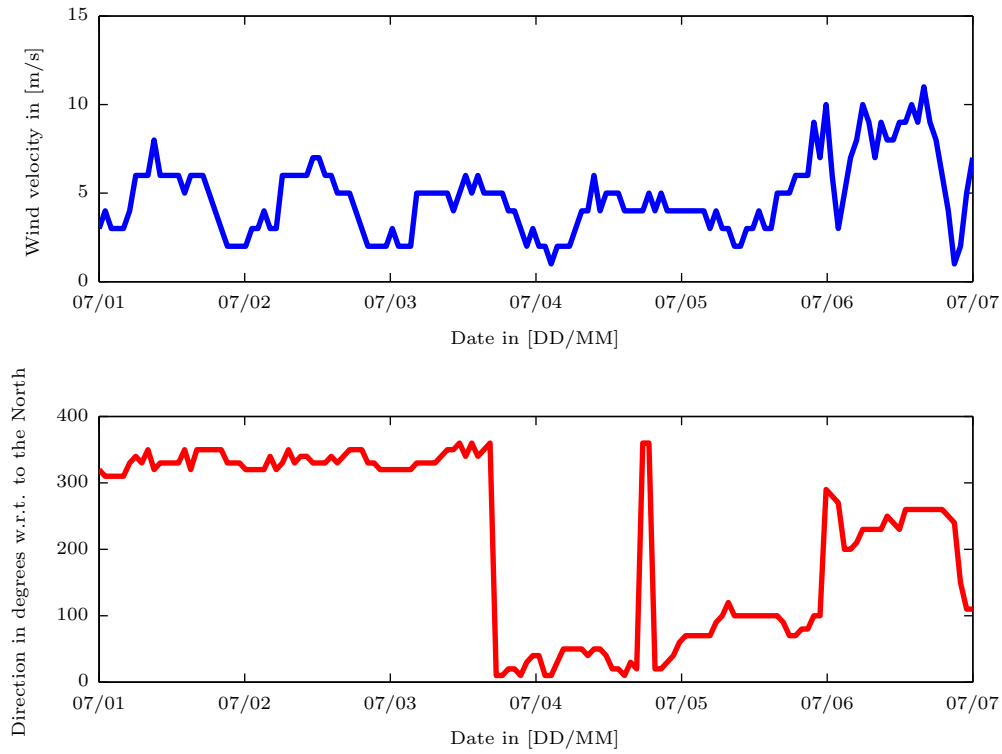
C.2   Meteo Information

Figure C.2: Observed wind velocity and direction in Vlissingen at 1 till 7 July 2011. Vlissingen is approximately 20 km separated from buoy 18. Courtesy: Royal Netherlands Meteorological Institute.

Appendix D

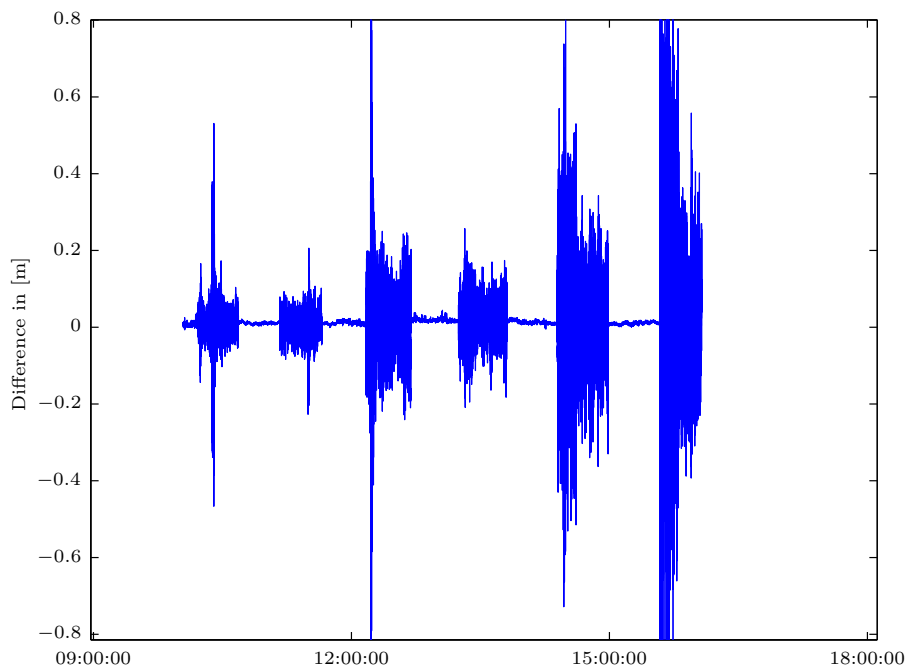# Processing kinematic baseline

Figure D.1: This graph shows the difference in baseline length (Multraship office in the City of Terneuzen - Buoy 18) derived with two different GPS data processing packages: Trimble Geomatics Office and MGP-software developed by Ir. P.J. Buist). The larger difference ($\geq 0.1m$) occur at the moment that TGO reports difficulties in the ambiguity determination, which results in a float solution. The mean difference in baseline length between the two packages is smaller than 1 cm. Observation date is 4 July 2011.
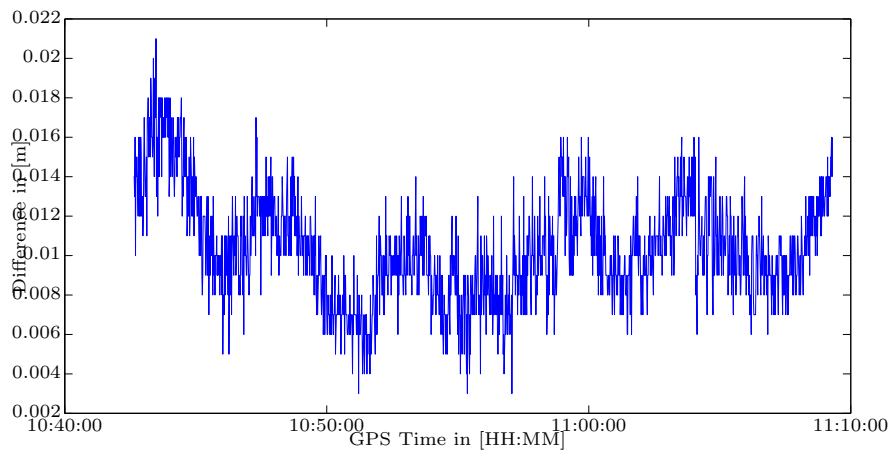
Figure D.2: This graph shows the difference in baseline length between two GPS data processing packages: Trimble Geomatics Office and MGP-software developed by Ir. P.J. Buist. The graph is a selection of figure D.1 during a period in time where the position estimates are based on a fixed phase solution for both software packages. The mean difference $\mu = 0.01$ m and the standard deviation $\sigma = 0.0027$ m. Observation date is 4 July 2011.

Auto-covariance of the output

The propagation law for the auto-covariance of the output $\underline{x}(t)$, assuming that $\underline{x}(t_0)$ is uncorrelated with $\underline{z}(t)$, is defined as [Teunissen, 2001]:

$$Q_{xx}(t_1, t_2) = \Phi(t_1, t_0)Q_{xx}(t_0, t_0)\Phi(t_2, t_0)^* + \int_{t_0}^{t_1}\int_{t_0}^{t_2}\Phi(t_1, \tau_1)G(\tau_1)Q_{zz}(\tau_1, \tau_2)G(\tau_2)^*\Phi(t_2, \tau_2)^* d\tau_1 d\tau_2$$

(E.1)

Inhere equals:

$$\Phi(t_1, t_0) = (\lambda_2 - \lambda_1)^{-1}\begin{bmatrix} \lambda_2 e^{\lambda_1(t_1-t_0)} - \lambda_1 e^{\lambda_2(t_1-t_0)} & -e^{\lambda_1(t_1-t_0)} + e^{\lambda_2(t_1-t_0)} \\ \lambda_1\lambda_2 e^{\lambda_1(t_1-t_0)} - \lambda_1\lambda_2 e^{\lambda_2(t_1-t_0)} & -\lambda_1 e^{\lambda_1(t_1-t_0)} + \lambda_2 e^{\lambda_2(t_1-t_0)} \end{bmatrix}$$

(E.2)

and

$$G = \begin{bmatrix} 0 \\ 1 \end{bmatrix}$$

(E.3)

In (E.2) the transition matrix for t_0 to t_1 is defined. The other transition matrices ($\Phi(t_1, t_0)$, $\Phi(t_2, t_0)$, $\Phi(t_1, \tau_2)$ and $\Phi(t_2, \tau_2)$) are obtained by a substitution of the time-notations on the left- and right hand side of the equation. $Q_{xx}(t_0, t_0)$ is described by the variance matrix of the initial state vector $\underline{x}(t_0)$. Q_{zz} is the auto-covariance matrix of the input vector $\underline{z}(t)$, which is in this case a scalar.

Filling in the terms in (E.1), the following yields:

$$Q_{xx}(t_1, t_2) = \Phi(t_1, t_0)Q_{xx}(t_0, t_0)\Phi(t_0, t_0)^* + \dots$$
$$(\lambda_2 - \lambda_1)^{-2}Q_{zz}\int_{t_0}^{t_1}\int_{t_0}^{t_2}\begin{bmatrix} \Phi_{12}(t_1, \tau_1)\Phi_{12}(t_2, \tau_2) & \Phi_{12}(t_1, \tau_1)\Phi_{22}(t_1, \tau_1) \\ \Phi_{22}(t_1, \tau_1)\Phi_{12}(t_2, \tau_2) & \Phi_{22}(t_1, \tau_1)\Phi_{22}(t_2, \tau_2) \end{bmatrix}d\tau_1 d\tau_2$$

(E.4)

In this equation implies ... that the function continues on the next line. The subscripts indicate the elements of the transition matrix E.2 and where:

$$\Phi_{12}(t_1, \tau_1)\Phi_{12}(t_2, \tau_2) = \frac{e^{\lambda_1 t_1}e^{\lambda_1 t_2}}{e^{\lambda_1 \tau_1}e^{\lambda_1 \tau_2}} - \frac{e^{\lambda_2 t_2}e^{\lambda_1 t_1}}{e^{\lambda_1 \tau_1}e^{\lambda_2 \tau_2}} - \frac{e^{\lambda_1 t_2}e^{\lambda_2 t_1}}{e^{\lambda_2 \tau_1}e^{\lambda_1 \tau_2}} + \frac{e^{\lambda_2 t_1}e^{\lambda_2 t_2}}{e^{\lambda_2 \tau_1}e^{\lambda_2 \tau_2}} \qquad (E.5)$$

$$\Phi_{12}(t_1, \tau_1)\Phi_{22}(t_2, \tau_2) = \frac{e^{\lambda_1 t_1}\lambda_1 e^{\lambda_1 t_2}}{e^{\lambda_1 \tau_1}e^{\lambda_1 \tau_2}} - \frac{e^{\lambda_1 t_1}\lambda_2 e^{\lambda_2 t_2}}{e^{\lambda_1 \tau_1}e^{\lambda_2 \tau_2}} - \frac{e^{\lambda_2 t_1}\lambda_1 e^{\lambda_1 t_2}}{e^{\lambda_2 \tau_1}e^{\lambda_1 \tau_2}} + \frac{e^{\lambda_2 t_1}\lambda_2 e^{\lambda_2 t_2}}{e^{\lambda_2 \tau_1}e^{\lambda_2 \tau_2}} \quad (E.6)$$

$$\Phi_{12}(t_2, \tau_2)\Phi_{22}(t_1, \tau_1) = \frac{e^{\lambda_1 t_1}\lambda_1 e^{\lambda_1 t_2}}{e^{\lambda_1 \tau_1}e^{\lambda_1 \tau_2}} - \frac{e^{\lambda_1 t_2}\lambda_2 e^{\lambda_2 t_1}}{e^{\lambda_2 \tau_1}e^{\lambda_1 \tau_2}} - \frac{e^{\lambda_2 t_2}\lambda_1 e^{\lambda_1 t_1}}{e^{\lambda_1 \tau_1}e^{\lambda_2 \tau_2}} + \frac{e^{\lambda_2 t_1}\lambda_2 e^{\lambda_2 t_2}}{e^{\lambda_2 \tau_1}e^{\lambda_2 \tau_2}}(E.7)$$

$$\Phi_{22}(t_1, \tau_1)\Phi_{22}(t_2, \tau_2) = \frac{\lambda_1{}^2 e^{\lambda_1 t_1}e^{\lambda_1 t_2}}{e^{\lambda_1 \tau_1}e^{\lambda_1 \tau_2}} - \frac{\lambda_1 e^{\lambda_1 t_1}\lambda_2 e^{\lambda_2 t_2}}{e^{\lambda_1 \tau_1}e^{\lambda_2 \tau_2}} - \frac{\lambda_2 e^{\lambda_2 t_1}\lambda_1 e^{\lambda_1 t_2}}{e^{\lambda_2 \tau_1}e^{\lambda_1 \tau_2}} + \frac{\lambda_2{}^2 e^{\lambda_2 t_1}e^{\lambda_2 t_2}}{e^{\lambda_2 \tau_1}e^{\lambda_2 \tau_2}}$$
$$(E.8)$$

Taking the double integral over the second matrix in (E.4), is done by taking the double integral over the individual elements of this matrix described by (E.5) till (E.8).

$$\int_{t_0}^{t_1} \int_{t_0}^{t_2} \Phi_{12}(t_1, \tau_1)\Phi_{12}(t_2, \tau_2)d\tau_1 d\tau_2 = \begin{array}{l} \frac{e^{\lambda_1 t_2}e^{\lambda_1 t_1}}{(e^{\lambda_1 t_0})^2 \lambda_1{}^2} - \frac{e^{\lambda_2 t_1}}{e^{\lambda_2 t_0}\lambda_2{}^2} - \frac{e^{\lambda_2 t_2}e^{\lambda_1 t_1}}{e^{\lambda_1 t_0}e^{\lambda_2 t_0}\lambda_1 \lambda_2} - \frac{e^{\lambda_1 t_2}e^{\lambda_2 t_1}}{e^{\lambda_1 t_0}e^{\lambda_2 t_0}\lambda_1 \lambda_2} + \cdots \\[4pt] \frac{e^{\lambda_2 t_2}e^{\lambda_2 t_1}}{(e^{\lambda_2 t_0})^2 \lambda_2{}^2} - \frac{e^{\lambda_1 t_1}}{e^{\lambda_1 t_0}\lambda_1{}^2} + \frac{e^{\lambda_2 t_2}e^{\lambda_1 t_1}}{e^{\lambda_2 t_0}e^{\lambda_1 t_2}\lambda_1 \lambda_2} + \frac{e^{\lambda_1 t_2}e^{\lambda_2 t_1}}{e^{\lambda_1 t_0}e^{\lambda_2 t_2}\lambda_1 \lambda_2} - \cdots \\[4pt] \frac{e^{\lambda_1 t_2}}{e^{\lambda_1 t_0}\lambda_1{}^2} + \lambda_2{}^{-2} + \frac{e^{\lambda_2 t_2}e^{\lambda_1 t_1}}{e^{\lambda_1 t_0}e^{\lambda_2 t_1}\lambda_1 \lambda_2} + \frac{e^{\lambda_1 t_2}e^{\lambda_2 t_1}}{e^{\lambda_2 t_0}e^{\lambda_1 t_1}\lambda_1 \lambda_2} - \cdots \\[4pt] \frac{e^{\lambda_2 t_2}}{e^{\lambda_2 t_0}\lambda_2{}^2} + \lambda_1{}^{-2} - \frac{e^{\lambda_2 t_2}e^{\lambda_1 t_1}}{e^{\lambda_1 t_2}e^{\lambda_2 t_1}\lambda_1 \lambda_2} - \frac{e^{\lambda_1 t_2}e^{\lambda_2 t_1}}{e^{\lambda_2 t_2}e^{\lambda_1 t_1}\lambda_1 \lambda_2} \end{array}$$
$$(E.9)$$

$$\int_{t_0}^{t_1} \int_{t_0}^{t_2} \Phi_{12}(t_1, \tau_1)\Phi_{22}(t_2, \tau_2)d\tau_1 d\tau_2 = \begin{array}{l} \frac{e^{\lambda_1 t_2}e^{\lambda_1 t_1}}{\lambda_1 (e^{\lambda_1 t_0})^2} - \frac{e^{\lambda_2 t_1}}{\lambda_2 e^{\lambda_2 t_0}} - \frac{e^{\lambda_2 t_2}e^{\lambda_1 t_1}}{\lambda_1 e^{\lambda_1 t_0}e^{\lambda_2 t_0}} - \frac{e^{\lambda_1 t_2}e^{\lambda_2 t_1}}{\lambda_2 e^{\lambda_2 t_0}e^{\lambda_1 t_0}} + \cdots \\[4pt] \frac{e^{\lambda_2 t_2}e^{\lambda_2 t_1}}{\lambda_2 (e^{\lambda_2 t_0})^2} - \frac{e^{\lambda_1 t_1}}{\lambda_1 e^{\lambda_1 t_0}} + \frac{e^{\lambda_2 t_2}e^{\lambda_1 t_1}}{\lambda_1 e^{\lambda_1 t_2}e^{\lambda_2 t_0}} + \frac{e^{\lambda_1 t_2}e^{\lambda_2 t_1}}{\lambda_2 e^{\lambda_2 t_2}e^{\lambda_1 t_0}} - \frac{e^{\lambda_1 t_2}}{\lambda_1 e^{\lambda_1 t_0}} + \cdots \\[4pt] \lambda_2{}^{-1} + \frac{e^{\lambda_2 t_2}e^{\lambda_1 t_1}}{\lambda_1 e^{\lambda_1 t_0}e^{\lambda_2 t_1}} + \frac{e^{\lambda_1 t_2}e^{\lambda_2 t_1}}{\lambda_2 e^{\lambda_2 t_0}e^{\lambda_1 t_1}} - \frac{e^{\lambda_2 t_2}}{\lambda_2 e^{\lambda_2 t_0}} + \lambda_1{}^{-1} - \cdots \\[4pt] \frac{e^{\lambda_2 t_2}e^{\lambda_1 t_1}}{\lambda_1 e^{\lambda_1 t_2}e^{\lambda_2 t_1}} - \frac{e^{\lambda_1 t_2}e^{\lambda_2 t_1}}{\lambda_2 e^{\lambda_2 t_2}e^{\lambda_1 t_1}} \end{array}$$
$$(E.10)$$

$$\int_{t_0}^{t_1} \int_{t_0}^{t_2} \Phi_{12}(t_2, \tau_2)\Phi_{22}(t_1, \tau_1)d\tau_1 d\tau_2 = \begin{array}{l} \frac{e^{\lambda_1 t_2}e^{\lambda_1 t_1}}{\lambda_1 (e^{\lambda_1 t_0})^2} - \frac{e^{\lambda_1 t_2}e^{\lambda_2 t_1}}{\lambda_1 e^{\lambda_1 t_0}e^{\lambda_2 t_0}} - \frac{e^{\lambda_2 t_2}e^{\lambda_1 t_1}}{\lambda_2 e^{\lambda_2 t_0}e^{\lambda_1 t_0}} + \frac{e^{\lambda_2 t_2}e^{\lambda_2 t_1}}{\lambda_2 (e^{\lambda_2 t_0})^2} - \cdots \\[4pt] \frac{e^{\lambda_1 t_1}}{\lambda_1 e^{\lambda_1 t_0}} + \frac{e^{\lambda_1 t_2}e^{\lambda_2 t_1}}{\lambda_1 e^{\lambda_2 t_2}e^{\lambda_1 t_0}} + \frac{e^{\lambda_2 t_2}e^{\lambda_1 t_1}}{\lambda_2 e^{\lambda_1 t_2}e^{\lambda_2 t_0}} - \frac{e^{\lambda_2 t_1}}{\lambda_2 e^{\lambda_2 t_0}} - \frac{e^{\lambda_1 t_2}}{\lambda_1 e^{\lambda_1 t_0}} + \cdots \\[4pt] \frac{e^{\lambda_1 t_2}e^{\lambda_2 t_1}}{\lambda_1 e^{\lambda_2 t_0}e^{\lambda_1 t_1}} + \frac{e^{\lambda_2 t_2}e^{\lambda_1 t_1}}{\lambda_2 e^{\lambda_1 t_0}e^{\lambda_2 t_1}} - \frac{e^{\lambda_2 t_2}}{\lambda_2 e^{\lambda_2 t_0}} + \lambda_1{}^{-1}\cdots \\[4pt] - \frac{e^{\lambda_1 t_2}e^{\lambda_2 t_1}}{\lambda_1 e^{\lambda_2 t_2}e^{\lambda_1 t_1}} - \frac{e^{\lambda_2 t_2}e^{\lambda_1 t_1}}{\lambda_2 e^{\lambda_1 t_2}e^{\lambda_2 t_1}} + \lambda_2{}^{-1} \end{array}$$
$$(E.11)$$

$$\int_{t_0}^{t_1} \int_{t_0}^{t_2} \Phi_{22}(t_1, \tau_1)\Phi_{22}(t_2, \tau_2)d\tau_1 d\tau_2 = \begin{array}{l} \frac{e^{\lambda_1 t_2}e^{\lambda_1 t_1}}{\left(e^{\lambda_1 t_0}\right)^2} - \frac{e^{\lambda_1 t_2}e^{\lambda_2 t_1}}{e^{\lambda_1 t_0}e^{\lambda_2 t_0}} - \frac{e^{\lambda_2 t_2}e^{\lambda_1 t_1}}{e^{\lambda_1 t_0}e^{\lambda_2 t_0}} + \frac{e^{\lambda_2 t_2}e^{\lambda_2 t_1}}{\left(e^{\lambda_2 t_0}\right)^2} - \dots \\[8pt] \frac{e^{\lambda_1 t_1}}{e^{\lambda_1 t_0}} + \frac{e^{\lambda_1 t_2}e^{\lambda_2 t_1}}{e^{\lambda_1 t_0}e^{\lambda_2 t_2}} + \frac{e^{\lambda_2 t_2}e^{\lambda_1 t_1}}{e^{\lambda_2 t_0}e^{\lambda_1 t_2}} - \frac{e^{\lambda_2 t_1}}{e^{\lambda_2 t_0}} - \dots \\[8pt] \frac{e^{\lambda_1 t_2}}{e^{\lambda_1 t_0}} + \frac{e^{\lambda_1 t_2}e^{\lambda_2 t_1}}{e^{\lambda_2 t_0}e^{\lambda_1 t_1}} + \frac{e^{\lambda_2 t_2}e^{\lambda_1 t_1}}{e^{\lambda_1 t_0}e^{\lambda_2 t_1}} - \frac{e^{\lambda_2 t_2}}{e^{\lambda_2 t_0}} + 2 - \dots \\[8pt] \frac{e^{\lambda_1 t_2}e^{\lambda_2 t_1}}{e^{\lambda_2 t_2}e^{\lambda_1 t_1}} - \frac{e^{\lambda_2 t_2}e^{\lambda_1 t_1}}{e^{\lambda_1 t_2}e^{\lambda_2 t_1}} \end{array}$$

(E.12)

Now the auto-covariance of the output is completely evaluated, the values for mass-spring model of buoy 18 are substituted in (E.4). That is $\gamma = 10\ s^{-1}$, $\omega^2 = \frac{1}{90}\ s^{-2}$, which results in the following two eigenvalues $\lambda_1 = 0.00055\ s^{-1}$ and $\lambda_2 = -20.00055\ s^{-1}$. Furthermore, we substitute the time notations: $t_0 = 0$ and $t_1 = t_2 = 1$. Now the following yields:

$$Q_{xx}(t_1, t_2) = \begin{bmatrix} -20.0116 & -1.0006 \\ -0.0110 & -0.0006 \end{bmatrix} Q_{xx}(t_0, t_0) \begin{bmatrix} -20.0116 & -0.0110 \\ -1.000550 & -0.000550 \end{bmatrix}$$
$$+ Q_{zz} \begin{bmatrix} 0.9040 & 0.9508 \\ 0.9508 & 1.0011 \end{bmatrix}$$

(E.13)